DETAILED MODELING AND OPTIMIZATION OF A MEMBRANE SYSTEM FOR ANESTHETIC GAS SEPARATION

by

Megan McNeil

Submitted in partial fulfilment of the requirements
for the degree of Master of Applied Science

at

Dalhousie University
Halifax, Nova Scotia
July 2017

Table of Contents

List of Tables

List of Figures

x

Abstract

Inhalation anesthesia is delivered using partial rebreathing circuits. The anesthetic compounds are not metabolized, so they can be re-administered to the patient if excess carbon dioxide is removed. There are multiple drawbacks associated with the current carbon dioxide removal technology, including the production of toxic by-products, which may harm the patient. As a result, a membrane separation system has been to replace the current technology. The objective of this thesis project was to develop and experimentally validate a modeling approach to predict and optimize the membrane system performance with sufficient accuracy in a timely manner. To meet these objectives, a segmental model was developed, experimentally validated, and used to study the performance for different patient scenarios. The model is a useful tool for designing and optimizing the performance of a membrane system for a novel application and fulfills the criteria of predicting the dynamic membrane system with acceptable accuracy.

List of Abbreviations and Symbols Used

Abbreviations

f	respiration frequency (min^{-1})
$etCO_2$	end tidal CO_2 concentration, equivalent to $expCO_2$
$expCO_2$	expired CO_2 concentration, equivalent to etCO2
$inspCO_2$	inspired CO_2 concentration
MV	minute volume ($mL\ min^{-1}$)
RMSE	root-mean-square error
RTD	residence time distribution
TV	tidal volume (mL)

Symbols

a	membrane surface area per unit of volume in the membrane module (m^{-1})
A_m	membrane area (m^2)
c	concentration ($mol\ m^{-3}$)
d	diameter (m)
D	diffusion coefficient ($m^2\ s^{-1}$)
E(t)	residence time distribution (s^{-1})
F	molar flow rate ($mol\ s^{-1}$), or volume force ($N\ m^{-3}$)
j	mass averaged flux ($kg\ m^{-2}\ s^{-1}$)
J	flux across the membrane ($mol\ m^{-2}\ s^{-1}$)
K	membrane permeance ($mol\ m^{-2}\ s^{-1}\ bar^{-1}$)
$1/K_{total}$	total resistance to transport in the system ($m^2\ s\ bar\ mol^{-1}$)
$1/k_F$	feed-side mass transfer resistance ($m^2\ s\ bar\ mol^{-1}$)
$1/k_P$	mass transfer resistance on the permeate side ($m^2\ s\ bar\ mol^{-1}$)
l	membrane thickness (m)
l/Q	mass transfer resistance in the membrane ($m^2\ s\ bar\ mol^{-1}$)
n	number of moles
N	molar flow rate across the membrane ($mol\ s^{-1}$) or tanks-in-series model parameter
P	pressure (bar)
Q	membrane permeability ($mol\ m\ m^{-2}\ h^{-1}\ bar^{-1}$)

r	radius (m)
R	universal gas constant (m^3 bar K^{-1} mol^{-1})
Re	Reynolds number
S	solubility coefficient in the membrane (mol m^{-3} bar^{-2}) or mass source term (kg m^{-2} s^{-1})
t	time (s)
T	temperature (K)
t_m	mean residence time (s)
V	total volume (m^3)
$\dot{V}$	volumetric flow rate (m^3 s^{-1})
w	mass fraction
y	molar fraction
y_{Exp}	experimental molar fraction
y_{sim}	simulated molar fraction

Greek letters

ε	porosity
θ	dimensionless time
κ	permeability of the porous medium (m^2)
μ	viscosity (kg m^{-1} s^{-1})
ρ	density (kg m^{-3})
σ^2	variance (s^2)
τ	space-time (s)

Subscripts

0	feed-membrane interface
A	discrete sub-section property
i	species *i*
k	shell or tube side of the membrane
L	permeate-membrane interface
F	feed
P	permeate
R	retentate
S	sweep

Acknowledgements

Chapter 1:   Introduction

1.1 Introduction to Anesthesia

General anesthetics are used in medicine to induce a state of unconsciousness in patients so they may endure invasive surgical procedures. One method of administering anesthesia is via inhalation of gaseous anesthetic agents. During inhalation anesthesia, a breathing gas mixture is delivered to the patient via mechanical ventilation. The gas mixture consists of a carrier gas and an anesthetic agent. The carrier gas mixture typically contains oxygen and varying amounts of nitrogen and/or nitrous oxide [1]. The most common anesthetic agents used in contemporary anesthesia are isoflurane, sevoflurane, and desflurane. These volatile halogenated ethers are readily vaporized into the carrier gas and delivered to the patient [1]. The chemical structure of these three compounds is shown in Table 1.1, along with some relevant physical properties.

Table 1.1. Physical properties of common anesthetic compounds [2]

Property	Isoflurane	Desflurane	Sevoflurane
Molecular formula	$C_3H_2ClF_5O$	$C_3H_2F_6O$	$C_4H_3F_7O$
Molar weight (g mol^{-1})	184.5	168.04	200.05
Boiling point at 760 mm Hg (°C)	48.5	22.8	58.5
Vapor pressure at 20°C (mm Hg)	238	669	157
Structure			

The respiration of an anesthetized patient is controlled by mechanical ventilation, which is also a convenient way to deliver the anesthetic agents. The expired gas mixture contains CO_2 from the patient's metabolic needs, as well as excess anesthetic compounds which are available to be reused. Most anesthesia systems today are configured as a circuit, where the expired gas mixture is returned to the anesthesia apparatus to minimize the loss of anesthetic compounds. Before recirculating the gas mixture to the patient, excess CO_2 must

be removed. A fresh gas flow must also be integrated into the breathing circuit to compensate for the removed gases and to maintain the metabolic O_2 requirement of the patient. A partial rebreathing circuit schematic is shown in Figure 1.1.
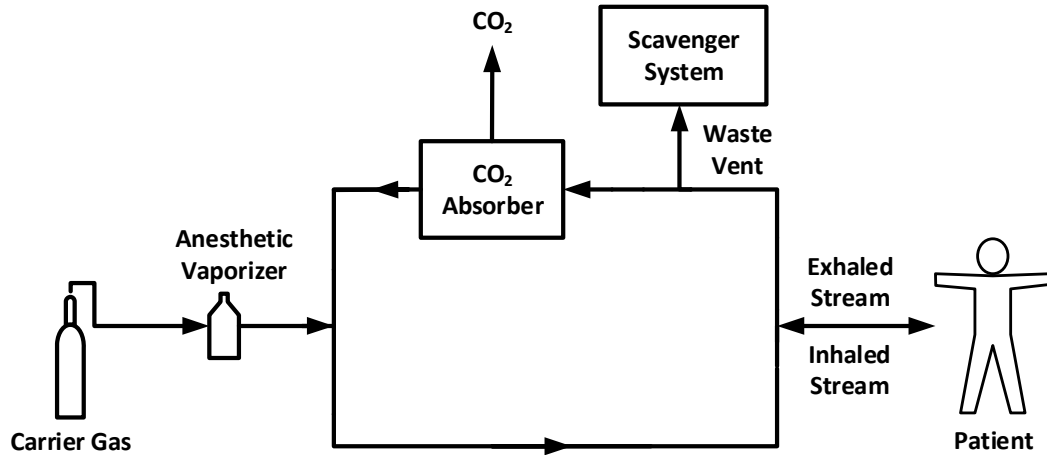
Figure 1.1. Flowchart of an anesthesia rebreathing circuit.

The current CO_2 removal method in anesthesia rebreathing circuits is by soda lime adsorption. Exhaled gas passes through a canister containing solid soda lime granules which remove most of the CO_2 before the remaining gas mixture is recycled in the rebreathing circuit. The circuit is also periodically vented to prevent build-up of inert compounds and waste gases.

1.2 Overview of Rebreathing

Anesthetic gases are expensive and contribute to ozone layer depletion and climate change [3]. Therefore, maximizing the re-use of these compounds provides both economic and environmental benefits. Rebreathing refers to the method used in modern anesthesia machines to conserve anesthetic compounds. Since the compounds are not metabolized, they may be recirculated to the patient if excess CO_2 is removed. Removal of CO_2 in anesthesia machines is currently achieved using canisters of adsorbent granules. The adsorbents typically consist of sodium hydroxide, potassium hydroxide, calcium hydroxide, and water [4]. However, there are drawbacks associated with the current CO_2 removal system. The adsorbents in commercially available units have been shown to react with the anesthetic vapors to create dangerous by-products, such as compound A and

carbon monoxide, which may pose a health risk to the patient [5]–[8]. To be specific, compound A (fluoromethyl-2,2-difluoro-1-[trifluoromethyl] vinyl ether) is a degradation product of sevoflurane and has been shown to contribute to a condition known as Post-Operative Cognitive Decline (POCD) and also contributes to kidney damage [9], [10]. Another drawback is the explosion and fire hazard that arises if the canister dries up. In addition, spent canisters must be replaced frequently and require specific and costly disposal treatments [11].

1.3 Alternative CO_2 Removal Technologies used in Anesthesia Partial Rebreathing Circuits

Alternative separation technologies have been explored to minimize the production of toxic by-products while permitting the rebreathing of anesthetic vapours. Adsorption technologies accomplish the separation of CO_2 from anesthetic gases efficiently but the production of toxic by-products presents a disadvantage to this technique. The degradation mechanism resulting from vapour interaction with adsorption units has been studied in an effort to eliminate this problem [5]. Several alternative adsorbents have been proposed that have been found to have minimal compound A and carbon monoxide production [5], [7]. Molecular sieves perform separations based on molecular size discrimination. Zeolite sieves have also been studied and successfully performed the required separation without the production of harmful by-products [12], [13]. An activated carbon filter is used in the anesthetic conserving device (AnaConDa®) to retain the volatile anaesthetics in the circuit without producing toxic by-products. While this technology omits the need for CO_2 removal, exhaled O_2 cannot be reused in this approach. Several membrane separation techniques have also been proposed but are still in early development stages [14], [15]. In particular, preliminary studies of immobilized liquid membranes for this application have been conducted and appear to demonstrate efficient separations [16]. In gas-liquid membrane contactors, the target component in the gas phase is absorbed into the liquid phase. Portugal *et al.* [17] proposed a membrane contactor which absorbs CO_2 from anesthesia breathing circuits using amino acid salt solutions. However, the regeneration process required to recycle the absorbent solution is a practical barrier for implementation in anesthesia apparatuses.

Despite research devoted to improving anesthesia delivery, absorption by soda lime remains the standard CO_2 removal technology in rebreathing circuits. However, a novel membrane-based system has recently been proposed and studied as a solution for CO_2 removal from anesthesia rebreathing circuits [18].

1.4 Alternative CO_2 Recovery Methods

The role of CO_2 as a greenhouse gas has prompted significant research focus on CO_2 capture and CO_2 separation technologies. There are several different approaches that could be considered to separate CO_2 from anaesthetic vapors in anesthesia rebreathing circuits.

Absorption processes are well established for CO_2 capture. In these processes, CO_2-rich gas mixtures are contacted with liquid absorbent solutions to selectively remove CO_2 from the gas phase. Absorption may be driven exclusively by vapor-liquid equilibrium between the gas and the liquid (physical absorption) or it may be assisted by chemical reaction in the liquid phase (chemical absorption). The selectivity of the process is determined by the absorbing solutions. After separation, the liquid solvent must be regenerated through a process of stripping, heating, and depressurization. The energy requirements for solvent regeneration is one of the main disadvantages of absorption processes.

Absorption operations may be implemented using membrane contactors to facilitate the contact between the gas and liquid phases [19]. A membrane contactor entails two phases separated by a semi-permeable membrane. The separation is governed by the absorption of a target component into a stream on the other side of the membrane. Gas-liquid contactors are commonly used for CO_2 capture. Typically, a gas mixture containing CO_2 is on one side of the membrane while a liquid solvent is on the other side. Carbon dioxide penetrates the membrane and is absorbed into the solvent. The membrane can be either porous or non-porous. Mass transfer across a non-porous membrane is governed by component solubility in the membrane and offers further selectivity beyond the liquid absorption. Porous membranes are non-selective and rely on the absorption into the solvent to drive the separation [20].

A final common CO_2 separation technology used for post-combustion carbon capture is adsorption. Adsorption is the reversible binding of a gaseous or liquid species (adsorbate) to the solid surface of an adsorbent [21]. The adsorbent is subsequently regenerated by desorbing the adsorbate. The adsorption mechanism is due to intermolecular forces between the target component and the solid adsorbent. The adsorption media typically has a high porosity to provide increased surface areas for sorption of the adsorbate.

1.5 Novel Membrane System for CO_2 Removal from Anesthesia Circuits

A new membrane-based system for CO_2 removal from anesthesia circuits was recently proposed by Wilfart *et al.* [18]. In this system, the anesthesia gas is passed through the shell side of a hollow fiber membrane contactor, while a sweep gas (O_2) is passed through the tube-side. The selected membrane is selective for CO_2 and only permits minimal transport of the anesthetic vapours. The primary advantages of this system are that only gases already present in the anesthesia circuit are used, no extreme conditions are required, no other mechanical systems are necessary, the system can be directly integrated into existing anesthesia machines, and, unlike some adsorbents, the membrane is completely inert.

1.6 Thesis Objectives

The purpose of this dissertation is to develop and validate a detailed modeling approach to predict the behaviour of a new membrane-based system [18] for CO_2 removal in anesthesia circuits, and then to use this model to optimize the performance of the system. It is proposed that a transient pseudo-one-dimensional model will be sufficiently accurate to predict *in situ* performance of the system and provide convenient coupling with ventilator models; however, multi-dimensional models will be necessary for optimizing the geometry of the system. The remaining chapters of this dissertation test this general hypothesis through a variety of modeling studies and experimentation. The following section provides an overview of the organization of this dissertation.

1.7 Thesis Structure

Several studies were performed to investigate and optimize the anesthesia gas membrane separation system. To organize these studies, this dissertation has been divided into seven chapters. Chapter 2 provides relevant background information related to membrane separation processes and modeling approaches. Chapter 7 presents a summary of major conclusions and contributions resulting from the presented studies. Chapters 3, 4, 5 and 6 are written in journal article format, and represent the major contributions stemming from this work. The intention is to submit these chapters for publication in journals focusing on membrane separation processes, separation process modeling, and anesthesia.

Chapter 3 summarizes the development of a pseudo-one-dimensional design model for the hollow fiber membrane system. The model is then calibrated using steady-state experimental data. Additionally, the model and steady-state experimental data are used to explore the impact of operating flow rates and membrane module configurations on separation performance.

In Chapter 4, a computational fluid dynamics (CFD) model is developed for the membrane system using a porous media approach and implemented using COMSOL Multiphysics. The CFD model and steady-state experimental data are then used to tune the membrane permeance. Further simulations are used to perform several numerical tracer studies to explore the impact of operating conditions on mixing behaviour in the module. The impacts of using chemical species with a finite permeability are also explored numerically.

In Chapter 5, a series of tracer experiments are used to validate the transient predictions of the design and CFD models. The focus is on mixing behaviour and on validating dynamic model predictions. It also demonstrated that it is not possible to completely decouple such predictions from membrane permeation.

In Chapter 6, the design model is coupled with an existing ventilator model and used to perform dynamic simulations for realistic patient scenarios. The simulation results are compared to experimental data obtained using an anesthesia circuit and a lung simulator.

Chapter 2:   Background Information

A membrane system has been proposed as an alternative separation technology for CO_2 removal from anesthesia rebreathing circuits. This chapter provides relevant background information about membrane systems and how these systems are analyzed.

2.1 Membrane Technology Introduction

Membrane technology has recently emerged as a promising alternative to conventional gas separation processes for a wide range of applications including applications as diverse as wastewater treatment, pharmaceutical production, and post-combustion carbon capture [19], [22]. Hollow fiber membrane contactors, in particular, offer several benefits including a high surface area to volume ratio, operational flexibility, and ease of modular scale-up [19]. In addition to developing novel membrane technologies, considerable effort has also been dedicated to creating mathematical models to describe the behavior of the membrane systems. Membrane system performance depends on several factors, so often a mathematical model is employed to gain insight into the influence of different operating parameters on performance.

2.2 Modeling Overview

Numerous modeling methodologies have been developed for membrane systems, with varying degrees of complexity. Balancing the trade-off between model accuracy and computational burden is a key challenge in any mathematical model. Computational fluid dynamics (CFD) usually refers to methods that permit the prediction of multi-dimensional, transient flow (*i.e.* velocity) fields. Usually, but not always, the velocity and pressure fields are determined by solving the Navier-Stokes and continuity equations. Since CFD provides local velocity estimates, other conservation equations (*e.g.*, species and energy) can then be solved to estimate other fields (*e.g.*, concentration and temperature) in a system. While CFD analysis provides important insight into the heat, mass and momentum transfer processes in a system, these simulations take a long time to solve, which limits their capacity to be used for parametric sensitivity studies and system optimization. Different simplifying assumptions may be used to reduce computation time; however, they also reduce the amount of information available from the predictions and model fidelity. In this

chapter, several modeling approaches will be explored with varying simplifications and levels of detail.

Hollow fiber membrane system models may be considered in terms of three sub-models: shell-side flow, membrane transport, and the tube-side flow. The total and component material balances on the retentate and permeate side are coupled by transport across the membrane. Different fluid properties and module geometries influence the physical behavior and transport in the membrane system. Therefore, the choice of flow model will differ depending on the system characteristics.

Membranes used in hollow fiber configuration may either be porous, or nonporous. The choice of transport model is determined based on the membrane type. Many hollow fiber membrane systems employ a porous membrane with an absorbent liquid on the permeate side of the membrane. In these cases, it may be reasonable to assume that the separation is controlled by liquid side mass transport. However, for the system considered in this thesis, a dense membrane is used to separate two gas streams, so the transport model discussion will focus on applying the widely-accepted solution-diffusion model to the membrane.

A visual representation of the transport of CO_2 in the membrane system is shown in Figure 2.1. The CO_2-rich feed enters the shell side of the membrane, and pure O_2 enters the tube side. Due to the concentration driving force, CO_2 diffuses through the boundary layer on the outside of the membrane fibers to the membrane surface. The CO_2 then dissolves in and diffuses through the membrane. The CO_2 then desorbs into the gas phase and diffuses across the concentration boundary layer on the tube side. The dissolution in the membrane, diffusion through the membrane, and desorption from the membrane are processes considered in the solution-diffusion model, whereas the other two processes constitute external mass transfer resistances.
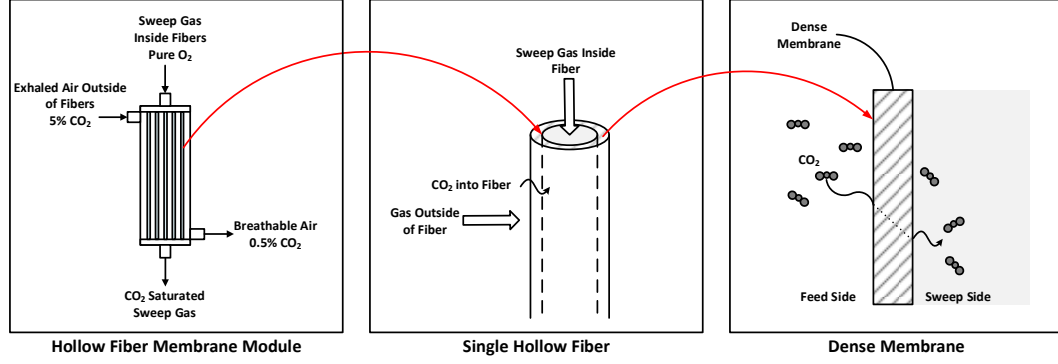
Figure 2.1. Schematic representation of a gas-gas hollow fiber membrane contactor system.

2.3 Dense Membrane Transport

Gas permeation through dense membranes is often described using the solution-diffusion model [23]. In the solution-diffusion model, gaseous components in the feed gas first dissolve into the membrane material and then diffuse down their concentration gradient through the membrane material to the permeate side of the membrane. If the diffusion through the membrane is assumed to follow Fick's law, the steady-state membrane flux can be written as:

$$J_i = \frac{D_i}{l}(c_{i0} - c_{il}) \tag{2.1}$$

Where J_i is the flux of component i across the membrane (mol m^{-2} s^{-1}), l is the membrane thickness (m), D_i is the diffusion coefficient of component i in the membrane (m^2 s^{-1}), c_{i0} is the concentration of component i on the feed side of the membrane (mol m^{-3}), and c_{il} is the concentration of component i on the permeate side (mol m^{-3}). If the gas solubility in the membrane is assumed to follow Henry's law, the concentration can be related to the partial pressure, p_i (bar), by the solubility coefficient for component i, S_i (mol m^{-3} bar^{-2}), in the membrane:

$$c_i = S_i p_i \tag{2.2}$$

The membrane permeability of component i, Q_i, (mol m m^{-2} h^{-1} bar^{-1}) is expressed as the product of the solubility and diffusivity in the membrane material:

$$Q_i = D_i S_i \tag{2.3}$$

9

Substituting Equations 2.2 and 2.3 into Equation 2.1 yields the following equation for the steady-state membrane flux:

$$J_i = \frac{Q_i}{l}(p_{i0} - p_{il})$$

(2.4)

Since it is challenging to define the membrane thickness in a consistent manner, the permeability and membrane thickness are often lumped together into a single parameter referred to as the permeance of component i, K_i. Since measuring the component partial pressures at the hollow fiber membrane interfaces is a difficult task, the driving force for mass transfer can be taken as the partial pressure difference between the bulk feed and bulk permeate. In this case, the permeance must be combined with the film mass transfer resistances into an overall mass transfer coefficient, K_{total}. Assuming ideal gas behaviour, Eq. 2.4 can then be expressed with the following equation:

$$J_i = K_i(p_{i0} - p_{il}) = K_{total}(y_{i,F}P_F - y_{i,P}P_P)$$

(2.5)

The permeance and overall mass transfer coefficient both have units of mol m^{-2} s^{-1} bar^{-1}. The overall mass transfer coefficient accounts for the mass transfer resistances on both sides of the membrane, as well as the resistance incurred by the membrane. This may be modeled using a resistors-in-series analogy with the inverse mass transfer coefficients on the feed side, in the membrane, and on the permeating side:

$$\frac{1}{K_{total}} = \frac{1}{k_F} + \frac{1}{K_i} + \frac{1}{k_P}$$

(2.6)

Where $1/K_{total}$ is the total resistance to transport in the system, $1/k_F$ is the feed-side mass transfer resistance, $1/K_i$ is the mass transfer resistance in the membrane, and $1/k_P$ is the mass transfer resistance on the permeate side (all with units of m^2 s bar mol^{-1}). For gas separations with dense membranes, the feed and permeate side mass transfer resistances are usually minor compared to the membrane resistance and the overall mass transfer rate is therefore controlled by the membrane resistance. For modeling this membrane system, the overall mass transfer coefficient was assumed to be the membrane permeance ($1/K_{total}$ $\approx 1/K_i$.

10

2.4 Membrane Configurations

Assuming that mass transfer resistances have already been minimized, mass transfer in membranes can be improved either by increasing the area available for mass transfer or by increasing the component partial pressure difference across the membrane (driving force) [19]. The driving force can be manipulated to optimize separation performance by altering the flow configuration of the feed and permeate streams. Most hollow fiber membrane modules can be categorized as either cross-flow or parallel-flow modules. Parallel-flow modules may be arranged in either a co-current or countercurrent configuration. In a co-current setup, the shell and tube-side fluids enter the module on the same side, while in a counter-current module, the two fluids enter at opposing sides. A simple schematic representation of the flow streams and the resulting concentration profiles along the length of the membrane are shown in Figure 2.2.
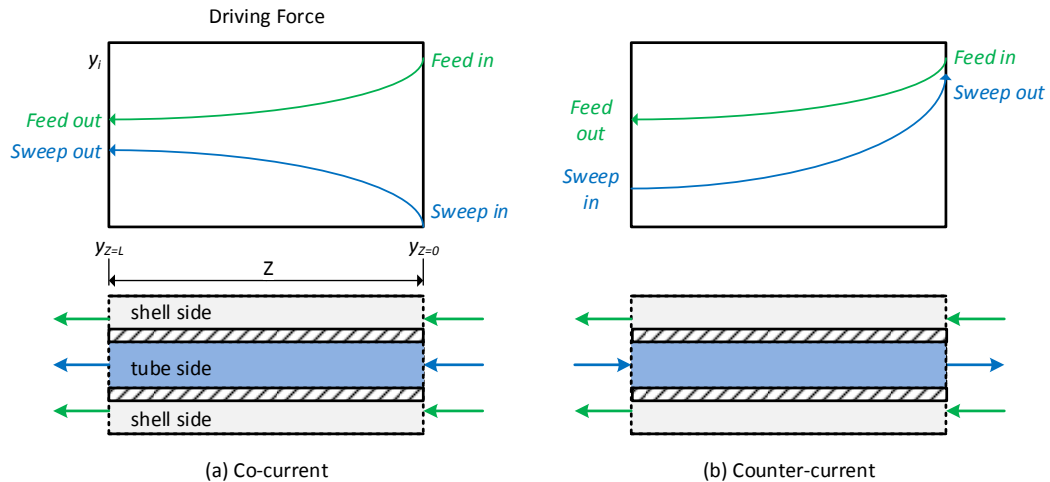
Figure 2.2. Schematic representation of driving force variation with module length for (a) co-current and (b) counter-current flow configurations. Modified from reference [18].

There are advantages and disadvantages associated with both parallel and cross-flow module configurations. Parallel-flow modules, when arranged in counter-current flow have a greater average driving force, and have demonstrated greater mass transfer efficiency compared to the equivalent co-current or cross-flow arrangement [24], [25]. However, parallel-flow modules are often associated with higher pressure drops over the length of the module, so cross-flow modules are often preferred, depending on the application.

2.5 Membrane System Description

The purpose of the model developed in this thesis is to model a specific hollow fiber membrane system that will be used to remove CO_2 from anesthesia circuits. There are several operational details that constrain the range of the different parameters used in the model. For instance, the system must be operated at atmospheric pressure and temperature, and is intended to directly replace the current CO_2 scrubbing device. As well, the resistance to feed flow must be minimized so that it does not interfere with the patient's breathing pattern. A detailed discussion of the constraints and resulting membrane system design is presented in reference [18]. Given the constraints of the system, the selected design consists of a cylindrical module with cross-wound polymethylpentene (PMP) fibers wrapped around a hollow perforated core. The feed gas exhaled by the patient enters the fiber bundle on the shell-side through the core and flows radially outward into the fiber bundle, where it contacts the membrane fibers. The feed gas CO_2 concentration in the anesthesia circuit must be reduced from 5% to 0.5% to be safely recirculated to the patient. To increase the driving force across the membrane and improve the separation, a pure O_2 sweep gas is supplied on the tube-side of the membrane module. A flow diagram of the module is shown in Figure 2.3.
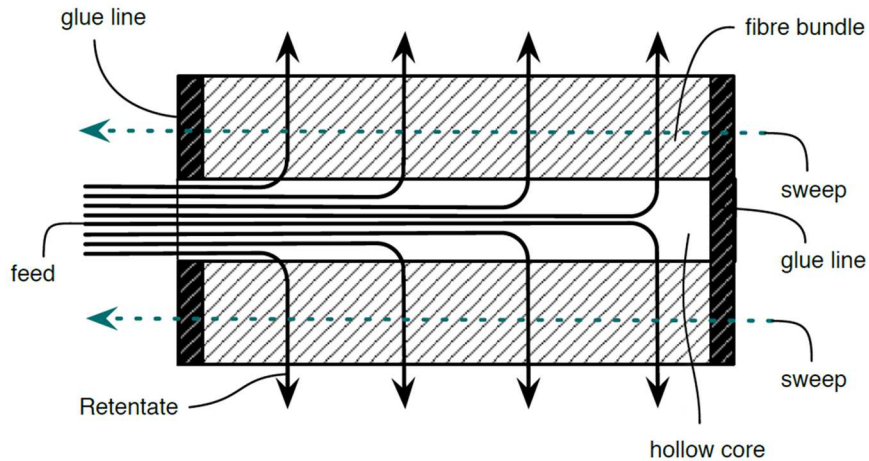
Figure 2.3. Schematic of the cross-flow module design [18].

2.6 Nomenclature

Symbols

c	concentration (mol L^{-1})
D	diffusion coefficient (m^2 s^{-1})
J	flux across the membrane (mol m^{-2} s^{-1})
K	membrane permeance (mol m^{-2} s^{-1} bar^{-1})
$1/K_{total}$	total resistance to transport in the system (m^2 s bar mol^{-1})
$1/k_F$	feed-side mass transfer resistance (m^2 s bar mol^{-1})
$1/k_P$	mass transfer resistance on the permeate side (m^2 s bar mol^{-1})
l	membrane thickness (m)
l/Q	mass transfer resistance in the membrane (m^2 s bar mol^{-1})
Q	membrane permeability (mol m^{-1} s^{-1} bar^{-1})
S	solubility coefficient in the membrane (mol m^3 bar^{-2})

Subscripts

0	feed-membrane interface
i	component i
L	permeate-membrane interface
F	feed
P	permeate

Chapter 3:   Modeling a Membrane System for Anesthetic Gas Separation using a Segmental Model

3.1 Introduction

Modern inhalation anesthesia is delivered using partial rebreathing circuits. Anesthetic compounds are delivered to the patient in a carrier gas mixture containing varying amounts of oxygen (O_2), nitrous oxide (N_2O), nitrogen (N_2), and carbon dioxide (CO_2). Since the anesthetic compounds are not fully metabolized on exhalation, they may be re-administered to the patient if excess CO_2 is removed from the exhaled gas stream. There are drawbacks associated with the current CO_2 removal system, so a membrane system has recently been proposed as an alternative to the current standard method of CO_2 adsorption by soda lime [3], [5]–[8], [11], [18].

Recently, considerable progress has been made in polymeric membrane development for CO_2 separation. A hollow fiber membrane system using a dense, asymmetric polymethylpentene (PMP) membrane has been proposed and shows good potential for anesthetic gas separation [26]. The purpose of this work is to develop and experimentally validate a mathematical model that can be used to predict the membrane system performance and assess the suitability of the proposed technology for anesthetic gas separation. The model will later be used to explore the performance of the membrane system during bench-scale experiments and under simulated patient conditions, and to further optimize the design of the device.

Hollow fiber membrane performance is governed, in part, by flow patterns within the membrane module. While flow inside the fibers has been well described using appropriate models, shell-side flow behaviour is more challenging to model due to the unknown mixing behavior arising from complex geometries [27]. Since performance is influenced by fluid flow behavior, it is important for the model to reflect the hydrodynamics inside the module appropriately.

Ideal flow patterns are often assumed because they are easy to describe mathematically and analyze. The two extreme cases are plug flow, which assumes no longitudinal mixing, and perfectly mixed, which assumes uniform properties in the flow domain [28]. These

assumptions simplify modeling, but may not always be suitable for systems experiencing non-ideal phenomena. There are several different approaches that have been used to account for deviation from ideal flow in hollow fiber membrane systems. Most non-ideal flow models that have been used to model membrane systems are based either on the axial dispersion model or the tanks-in-series model [29].

The axial dispersion model represents mixing by superimposing a dispersion term onto the plug flow model [30]. The axial dispersion coefficient introduces longitudinal dispersion to the standard one-dimensional plug flow. A dispersion coefficient may also be introduced for each direction in multidimensional models. Marriot and Sorenson [31] proposed a general modeling approach for hollow fiber membrane modules in two-dimensional cylindrical coordinates and introduced axial and radial dispersion coefficients to the shell-side flow model. Dindore *et al.* [27] also used an approach derived from the dispersion model to described shell-side flow maldistribution in a rectangular hollow fiber membrane module. This group performed a series of tracer studies on the shell-side of the membrane and quantified the mixing behaviour by determining the dispersion coefficient in three directions.

While the dispersion model may provide a high degree of accuracy, it is usually at the cost of complicated resolution methods. A disadvantage of approaches based on the dispersion model is that they often require the solution of partial differential equations. Another drawback of the axial dispersion model is that it may not be appropriate for systems that deviate significantly from plug flow.

An alternative non-ideal flow model is the tanks-in-series model, where the system is represented by a number, *N*, of equally-sized perfectly-mixed tanks in series. Perfect mixing can be achieved by employing a single tank ($N = 1$), and plug flow behaviour is approached by increasing the number of units in series until true plug flow is achieved when the number of tanks approaches infinity. An axial dispersion model can be replicated by tuning the number of tanks.

A variant of the tanks-in-series model has been previously applied in membrane separations to describe deviations from ideal flow models. Katoh *et al.* [32] used this

approach to model the dynamic performance of a hollow fiber membrane module. They considered non-ideal flow by varying the number of mixed tanks to independently describe mixing on the shell-side and tube-side of the membrane.

A key advantage of the tanks-in-series approach is that the dynamic governing equations are easily resolved compared to alternative dynamic models. Since dynamics are important for this application of anesthesia administration, the model must be able to handle these types of predictions. Since hollow fiber membrane modules are susceptible to flow maldistribution, it is also important for the model to be able to capture these effects. Also, since the model will be used to perform sizing calculations and optimization studies, it should be fast enough to permit these case studies in a timely matter. Based on these criteria, a tanks-in-series approach will be used for the design model development, with membrane transport coupling the tube and shell sides.

In this chapter, a variant of the tanks-in-series model is derived for gas separation by a hollow fiber membrane module. The number of segments was determined by fitting the model to steady-state experimental data over a range of flow rates. The membrane permeation properties for CO_2, O_2 and N_2, which have been determined in Chapter 4, were used in the model. Several membrane module configurations were studied as part of the system optimization, including a double-pass arrangement and modules with different packing densities [18], so the model was adapted to account for these variations.

3.2 Model Description

3.2.1 System Overview

Assembled PMP membrane modules (with hollow fiber membrane bundles supplied by 3M, Membranes Business Unit in Wuppertal, Germany), were used in this study. The membrane bundle consists of a cross-wound hollow fiber mat wrapped around a cylindrical perforated hollow core that is glued on either end to separate the shell and tube flows. For the double-pass configuration, an O-ring was placed on the lower surface of the fiber bundle, forcing the tube-side flow to pass through the bundle twice. A diagram of the module and flow arrangement is shown in Figure 3.1. The shell-side fluid enters the fiber

bundle through the inner core and flows radially outward across the membrane bundle. A sweep gas is administered through the hollow fibers.
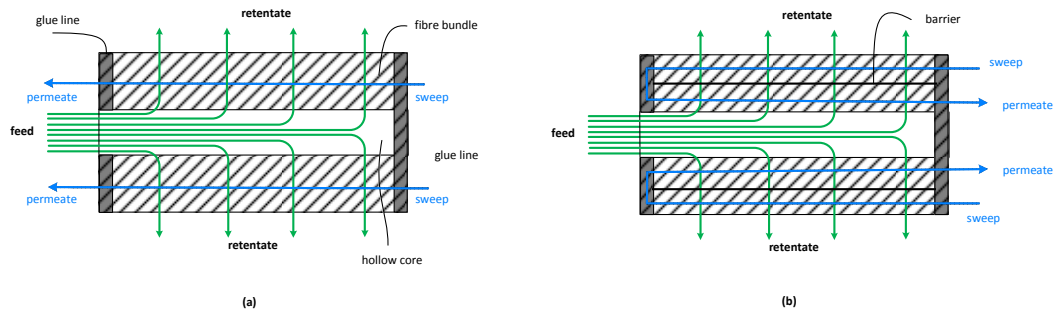
Figure 3.1. Schematic diagram of membrane module: (a) single-pass, and (b) double pass.

The model was formulated by dividing the membrane module into discrete completely-mixed control volumes (or segments). Figure 3.2a shows the module discretization for a simple cross-flow configuration, while Figure 3.2b provides a more accurate representation of the streams entering and exiting each control volume. The model has also been adapted to simulate multiple membrane passes, as shown in Figure 3.2c.
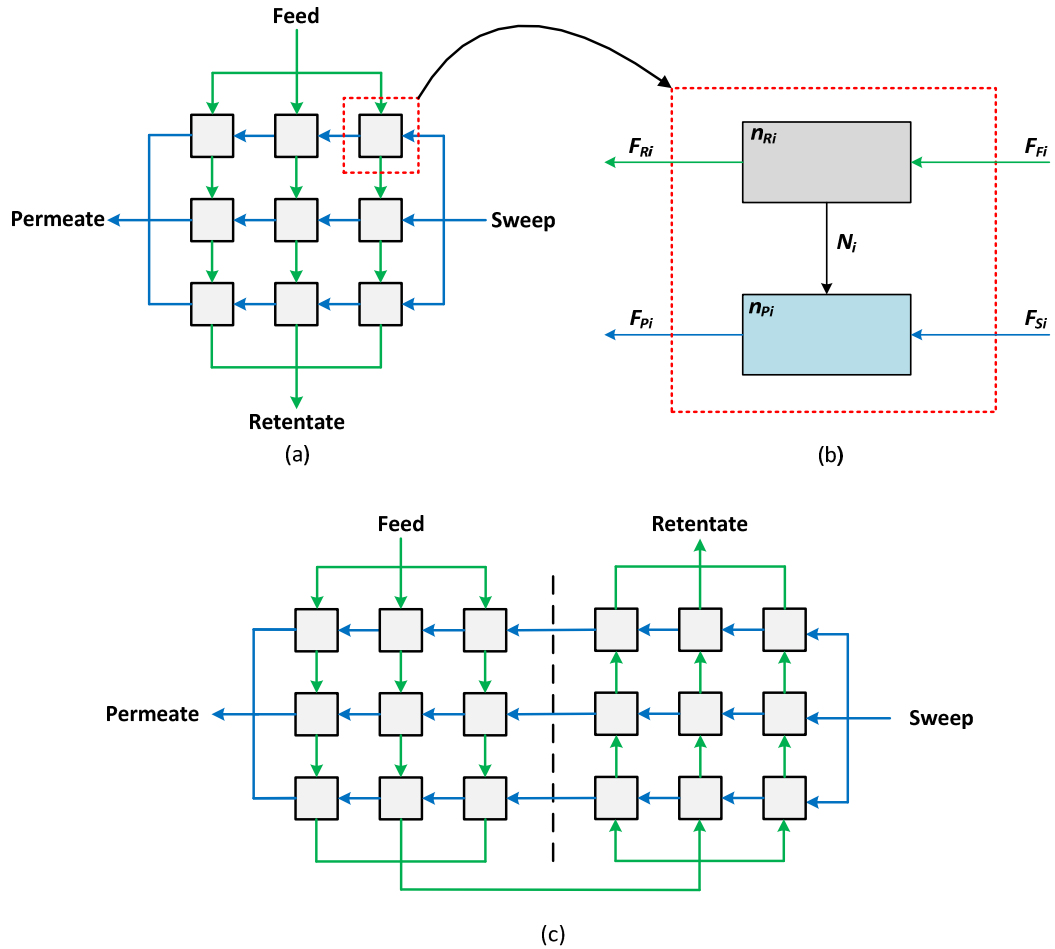
Figure 3.2. Schematic representation of discrete module subdivisions for (a) simple single-pass cross-flow arrangement, (b) control volume over each feed and sweep subdivision, and (c) two-pass arrangement.

The model was derived by solving the total and component mass balances, coupled with the local membrane permeation rate expressions for each segment. The outlet conditions were used to determine the permeation rate for each segment (*i.e.*, completely-mixed control volumes). Each segment includes control volumes for both the feed and sweep (shell and tube) sides of the membrane. In this system, the feed gas is allocated to the shell side of the membrane module, while a pure sweep gas is delivered to the tube-side.

3.2.2 Model Derivation

The following assumptions were applied when deriving the model:

- Ideal gas behavior

- Uniform membrane properties

- Membrane permeances are constant

- Membrane transport follows the solution-diffusion model [23]

- Negligible shell and tube-side mass transfer resistance (mass transfer is governed only by membrane resistance)

- Isothermal system

- Negligible shell-side pressure drop

- Negligible tube-side pressure drop

These assumptions are frequently employed in hollow fiber membrane modeling [32]–[35].

Using the solution-diffusion model, the flux of a given species across dense membranes can be determined by multiplying the membrane permeance of a specific component by the partial pressure difference of the component between the feed and permeate side of the membrane. Applying the ideal gas assumption, the mole fractions, and bulk pressures on either side of the membrane can be substituted for the partial pressures. The flux can then be multiplied by the mass transfer area to determine the molar permeation rate of component i for a given segment:

$$N_{iA} = K_i A_{MA}(y_{i,RA} P_R - y_{i,PA} P_P) \qquad (3.1)$$

Where N_{iA} is the molar flow rate of component i across the membrane for segment A (mol s^{-1}), K_i is the membrane permeance for component i (mol m^{-2} s^{-1} bar^{-1}), A_{MA} is the membrane area of a segment A (m^2), $y_{i,RA}$ and $y_{i,PA}$ are the molar fractions of component i on the retentate and permeate sides of the membrane for segment A, respectively, and P_R and P_P are the bulk pressures (bar) of the retentate and permeate side. Note that P_R and P_P have not been given subscripts of A because pressure drop through the segments was neglected.

Since both pressure and temperature on either side of the membrane are assumed to be constant for each control volume, there is no change in molar density (or molar volume) for each control volume with time. Additionally, the control volumes have a fixed size, and therefore there is no change in volume with time. Thus, there cannot be any total material

19

accumulation with time in any control volume. It follows that the molar flow rate of the retentate stream exiting a given control volume is equal to the total molar permeation rate subtracted from the molar feed rate coming in:

$$\frac{dn_{RA}}{dt} = F_{FA} - F_{RA} - \sum N_{i,A} = 0 \tag{3.2}$$

Where F_{FA} and F_{RA} are the molar feed and retentate flow rates entering and exiting segment A (mol s^{-1}), the sum of $N_{i,A}$ is the total molar permeation rate for segment A, n_{RA} is the total number of moles on the feed/retentate side of the membrane for segment A (mol), and t is time (s). Similarly, the molar flow rate of the permeate stream exiting a given control volume is equal to the total molar permeation rate added to the sweep flow rate coming in:

$$\frac{dn_{PA}}{dt} = F_{SA} - F_{PA} + \sum N_{i,A} = 0 \tag{3.3}$$

Where F_{SA} and F_{PA} are the molar sweep and permeate flow rates entering and exiting segment A (mol s^{-1}), and n_{PA} is the number of moles on the permeate side of the given segment.

The total retentate and permeate flow rates leaving segment i can then be calculated from:

$$F_{RA} = F_{FA} - \sum N_{i,A} \tag{3.4}$$

$$F_{PA} = F_{SA} + \sum N_{i,A} \tag{3.5}$$

The amount of gas (in moles) on the retentate and permeate sides for a given segment can be calculated using the ideal gas law:

$$n_{RA} = \frac{P_R V_R}{N \cdot R \cdot T} \tag{3.6}$$

$$n_{PA} = \frac{P_P V_P}{N \cdot R \cdot T} \tag{3.7}$$

Where N is to total number of segments, P_R and P_P are the bulk retentate and permeate pressures (bar), V_R is the total retentate-side volume (m^3), V_P is the total permeate-side volume (m^3), T is the system temperature (K), and R is the universal gas constant

(m^3 bar K^{-1} mol^{-1}). Since the pressure is assumed to be constant, the retentate and permeate pressures are assumed to equal the feed and sweep inlet pressures. Additionally, since the system was assumed to be isothermal, no energy balance equations needed to be solved, and no other equations are required to estimate the pressure drop. In the current study, the feed was on the shell-side of the membrane and the sweep was on the tube side. Therefore, the retentate volume is the total shell-side volume, while the permeate-side volume is the total volume inside the fibers.

The species balances for a molar quantity of component i for segment A on each side of the membrane are given by:

$$\frac{d(n_{RA}y_{i,RA})}{dt} = y_{i,FA}F_{FA} - y_{i,RA}F_{RA} - N_{i,A} \tag{3.8}$$

$$\frac{d(n_{PA}y_{i,PA})}{dt} = y_{i,SA}F_{SA} - y_{i,PA}F_{PA} + N_{i,A} \tag{3.9}$$

Where $y_{i,FA}$ and $y_{i,SA}$ are the feed and sweep mole fractions of species i entering segment A, and $y_{i,RA}$ and $y_{i,PA}$ are the retentate and permeate mole fractions exiting the segment. Since the total molar accumulation rates on both sides of the membrane are negligible (equations 3.2 and 3.3), the total molar quantity in each segment on each side of the membrane can be factored out of the time derivative. Therefore, the temporal rate of change of the mole fractions leaving each segment are given by:

$$\frac{dy_{i,RA}}{dt} = \frac{y_{i,FA}F_{FA} - y_{i,RA}F_{RA} - N_{i,A}}{n_{RA}} \tag{3.10}$$

$$\frac{dy_{i,PA}}{dt} = \frac{y_{i,SA}F_{SA} - y_{i,PA}F_{PA} + N_{i,A}}{n_{PA}} \tag{3.11}$$

The model is configured to allow transient simulations because it will be used to simulate the membrane performance in an actual, time-dependent anesthesia setting. However, this study is focused on comparing model predictions with steady-state performance data. Steady-state simulations were performed by solving equations 3.1, 3.4, 3.5, 3.10, and 3.11.

3.2.3 Numerical Implementation

The model was solved using a MATLAB [36] program that solved the total (Eqs. 3.4 and 3.5) and component (Eqs. 3.10 and 3.11) material balances coupled by the local membrane permeation rate (Eq. 3.1) for each discrete section of membrane. The resulting equations were solved using two approaches to ensure consistency. First, the time derivatives in Equations 3.10 and 3.11 were set to zero, and the *fsolve* function in MATLAB was used to solve the resulting nonlinear system of algebraic equations. Second, the time derivatives were retained in Equations 3.10 and 3.11, and the *ode15s* function in MATLAB was used to integrate the resulting coupled system of first-order ordinary differential and algebraic equations until steady state was reached. As expected, both approaches yielded the same steady-state results. Thus, due to its greater computational efficiency, the first approach was used for the steady-state simulations. In addition to solving the system of equations, the MATLAB program also performed mixing and post-processing calculations where these were required. One of the major goals of the study was to determine the number of segments required in the model to fit the experimental data. Therefore, simulations were performed with a large range of combinations for the number of segments (*i.e.* in the feed and sweep directions).

3.3   Experimental

3.3.1 Materials

Membrane bundles were supplied by 3M, Membranes Business Unit in Wuppertal, Germany (3M). The membrane bundle consists of a cross-wound fiber mat wrapped around a cylindrical perforated hollow core. The fibers are potted in a disk-shaped glue line on either end and planted inside a glue line to separate the feed and sweep sides. The feed enters the fiber bundle through the inner core and flows radially outward into the fiber bundle, where it contacts the surface of the hollow fibers. The sweep enters on the tube side of the bundle and flows through the hollow fibers. Each membrane bundle was placed in a custom housing (manufactured using SLS Rapid Prototyping, Stratasys Ltd., Eden Prairie, Minnesota, USA) to form a membrane module having appropriate connections to the rest of the system.

The standard membrane module in this study was intended to be used to reduce the CO_2 concentration in anesthesia circuits from 5% to 0.5% by volume. The surface area required to meet this target was determined with preliminary simulations. Given the size constraints in an anesthesia system, a two-pass configuration was also explored with the goal of improving separation performance and optimizing the membrane area. The two-pass configuration was obtained by implanting an O-ring on the lower surface of the fiber bundle, forcing the sweep to take two passes through the bundle.

Two additional double-pass modules were also studied in these experiments, with varying dimensions and hollow fiber packing densities. Table 3.1 provides the dimensions of the membrane modules used in this study.

Table 3.1. Module dimensions

	Module number			
	1	**2**	**3**	**4**
Number of passes	two	two	one	two
Packing density, φ	0.213	0.302	0.45	0.45
Fiber inner diameter, d_i (µm)	200	200	200	200
Fiber thickness, δ (µm)	90	90	90	90
Number of fibers, N	9440	13365	27400	29500
Active membrane length, L_M (mm)	120	120	120	120
Fiber bundle diameter d_B (mm)	80	80	100	100
Core diameter, d_C (mm)	20	20	20	20
Area ratio of inner to outer pass	0.60	0.60	-	0.61
Active inside membrane area, A_M (m^2)	0.61	0.86	2.14	2.10

The membrane permeance used in the model was determined using a two-dimensional computational fluid dynamics (CFD) model (as described in Chapter 4). Table 3.2 shows the membrane permeance values that were determined using this approach.

Table 3.2. Membrane permeance values obtained from fitting procedure with CFD model

Membrane permeance (mol m^{-2} h^{-1} bar^{-1})		
CO$_2$	O$_2$	N$_2$
45.0	18.0	4.5

3.3.2 Methods

The purpose of the steady-state experiments was to obtain tuning and validation data over a representative range of feed and sweep flow rates. Pure oxygen (O$_2$) was used as the sweep gas, and a 5% carbon dioxide (CO$_2$) in O$_2$ mixture was used as the feed. The gas concentrations were measured using a quadrupole mass spectrometer (Omnistar Model PTM81217131, Pfeiffer Vacuum, Aßlar, Germany) with a minimum detection limit of 1 ppm. The mass spectrometer was operated using Secondary Electron Multiplier (SEM) ion detection and can measure masses in the range of 1 to 300 AMU. Pfeiffer Vacuum's Quadera software (v4.50.004) was used to control the mass spectrometer. A spectral resolution of 50 and a dwell of one second was used for the experiments. The mass spectrometer has a stainless steel capillary gas connection which was operated at 150°C.

The mass spectrometer was calibrated for mass specific concentration determination using Pfeiffer Vacuum's recommended calibration procedure [37], [38]. An offset calibration was performed to eliminate any inherent offset of the measured SEM signal. A mass scale adjust calibration was conducted to tune the mass scale to adjust the measured value of each mass of interest to an integer value. A background determination calibration was performed to identify any mass peaks from residual gases that were not associated with the gases being measured. Background spectra from this calibration were subtracted from subsequent measurements. The final calibration was the gas specific calibration, where ion peaks are translated to concentration by the gas specific calibration, which entails the assignment of compounds to mass peaks. A calibration factor library was then constructed using certified calibration gas mixtures. The mass spectrometer calibration was maintained throughout the course of the experimental testing.

After measuring the initial feed concentration, the feed was supplied to the shell-side of module while the sweep was supplied to the tubes at predetermined flow rates. The flow rates are summarized in Table 3.3. The flow rates were controlled using a Scott Specialty Gases glass tube rotameter ($\pm$ 5% of full scale, 15.61 L min^{-1}) and measured using an Aalborg XFM digital mass flow meter ($\pm$ 5% of full scale, 20 L min^{-1}).

Table 3.3. List of flow rates used in experiments

Feed flow rates (L min^{-1})	Sweep flow rates (L min^{-1})
5	1
10	3
15	5
	7
	9
	11
	13
	15

Since the mass spectrometer can only monitor one gas at a time, the retentate and permeate concentrations were measured separately. First, the retentate was measured continuously for the full range of flow rates. The flow conditions were then replicated and the permeate was measured continuously. The concentration for each flow rate was recorded once the system stabilized. Figure 3.3 shows a diagram of the experimental configuration.
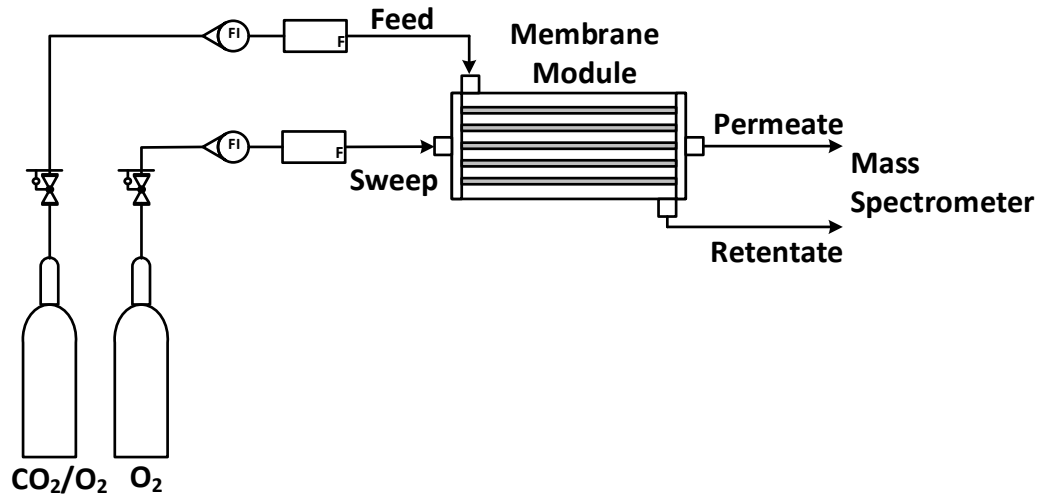
Figure 3.3. Schematic diagram of the experimental setup used for steady-state validation experiments.

3.4 Results and Discussion

3.4.1 Model Calibration

To calibrate the model, the experimental conditions were simulated with different numbers of segments in the model. The exiting retentate and permeate concentrations predicted by the model were then compared to the experimental measurements. An appropriate number of segments was chosen based on the overall best fit for the full range of flow rates for the permeate and retentate measurements. Figure 3.4 shows the experimental data of the exiting permeate and retentate concentrations for the 5 L min^{-1} feed flow rate case with three different discretization schemes. The results shown in this figure are for the single-pass module.
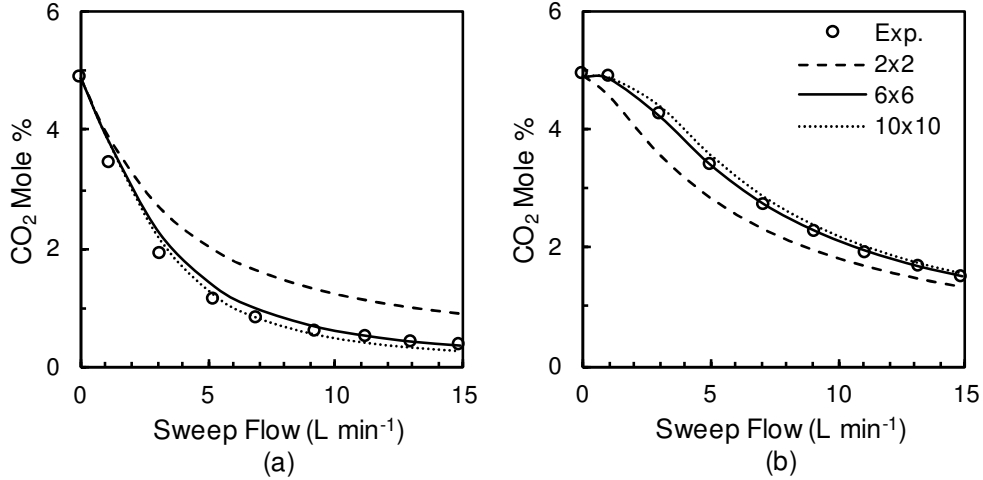
Figure 3.4. Single-pass (Module 3) experimental and simulated data for 5 L min^{-1} feed flow and varying sweep flow rates (0, 1, 3, 5, 7, 9, 11, 13, and 15 L min^{-1}) with three segmental models (2×2, 6×6, 10×10) for the exiting CO_2 concentration in (a) the permeate and (b) the retentate.

Depending on the data point, the best fit model is not always consistent across the full range of flow rates. This is exemplified in Figure 3.4b, where the 5 L min^{-1} sweep flow rate is more accurately predicted by the 10×10 model, while the 6×6 model provides a better fit for the 15 L min^{-1} sweep flow rate case. Furthermore, it would normally be expected that the permeate and retentate concentrations would be best predicted by the same model for a given data point. However, Figure 3.4 shows that the permeate concentration for the 5 L min^{-1} flow rate is better predicted by the 6×6 model, while the retentate concentration for the same case is better predicted by the 10×10 case. Such a difference in model fit could be due to experimental uncertainties (*e.g.*, flow rate measurement error) and/or the simplifying assumptions used to derive the model. Since the general fit of the model was relatively good and the experimental data was consistent, a model configuration was selected so that it provided a reasonable global fit for the full range of flow rates and concentration measurements.

Selecting the model with the best fit was not trivial, given the large amount of data for all the different model combinations. To facilitate this process, the root-mean-square error (RMSE) over the full range of flow rates was calculated for each unique model structure. The RMSE was calculated using the following equation:

27

$$RMSE = \sqrt{\frac{\sum_{i=1}^{n}(y_{Exp}-y_{sim})^2}{n}}$$ (3.12)

where y_{Exp} is the experimental concentration, y_{sim} is the simulated concentration, and n is the total number of data points. The RMSE was computed separately for the permeate and retentate concentration measurements as well as for the combined dataset. Surface contour plots of the RMSE were then generated for each combination of feed and sweep discretization schemes to provide insight into the appropriate range of segments that minimize the deviation between the experimental and simulated values. An example of the error surface contour plots is shown in Figure 3.5 for Module 4. The permeate error is shown in Figure 3.5a, the retentate error in Figure 3.5b, and the combined error in Figure 3.5c.
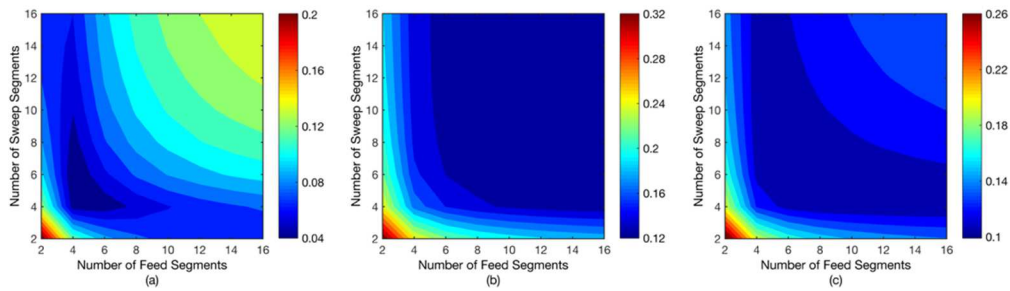
Figure 3.5. Surface contour of the root-mean-square error for Module 4 for varying number of segments showing (a) permeate, (b) retentate, and (c) combined.

These surface figures were generated for each membrane module to assist in selecting a reasonable model. Additionally, the numerical values of the errors were analyzed. However, as shown in Figure 3.5, there are multiple combinations of the number of segments that provide nearly the same numerical error values. Therefore, the optimal number of segments for each module was selected using the numerical error values and judgement based on the physical configuration of the module. This relative insensitivity of the model to the number of segments over a range of values is an important finding in this study because it means that it is possible to use the model to extrapolate predictions for smaller and larger modules. Specifically, this means that it would be possible to fit a model for one membrane configuration and size, and then use that number of segments to make

performance predictions for modules with smaller and/or larger surface areas. The calibrated number of segments for each module tested in this study is shown in Table 3.4.

Table 3.4. Tuned number of segments for each membrane module

Module number	Number of feed segments	Number of sweep segments	Number of passes
1	2	2	2
2	6	6	2
3	6	6	1
4	10	6	2

A comparison between experimental and simulated results over the full range of feed and sweep flow rates using the calibrated model are shown in parity plots in Figure 3.6 for each membrane module used in this study.
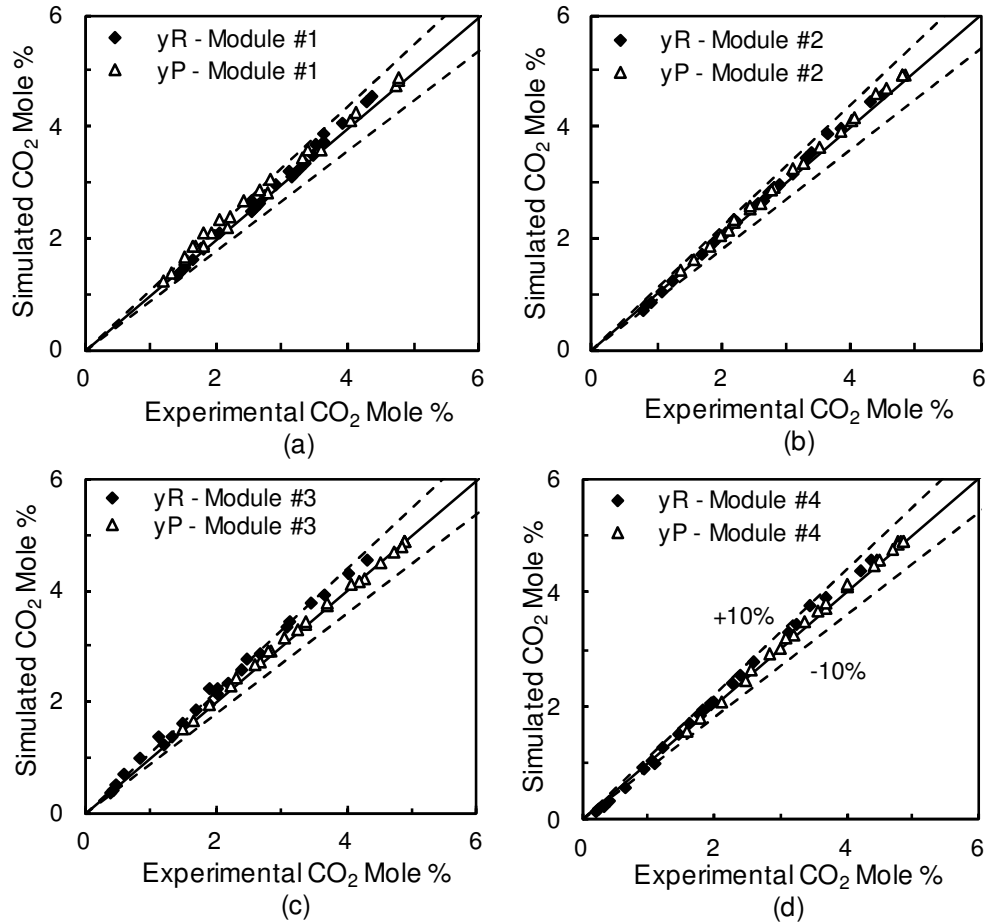
Figure 3.6. Parity plot for permeate and retentate CO_2 concentration for each module: (a) Module 1, (b) Module 2, (c) Module 3, and (d) Module 4.

A model structure that over-predicts performance would result in a higher permeate concentration and lower retentate concentration. This would be easy to identify on a parity plot and could be addressed by re-tuning the model. Overall, there do not appear to be significant data mismatches that could be addressed with more tuning. The calibrated models fit the experimental data reasonably well, with most of the simulated data points lying within 10% of the experimental values.

The simulations for the permeate (triangles) of Module 1 (Figure 3.6a) seem to have a greater (positive) deviation from the experiment, while the retentate measurements are better predicted. The model structure resulting from the tuning procedure for this module is an outlier (2×2) compared to the other modules, which were tuned to have many more segments. The tanks-in-series model interpretation is that a greater number of segments

30

indicates increased plug flow behaviour. Plug flow also leads to better membrane performance when compared to perfect mixing since the average driving force is higher. Module 1 has the lowest packing density, so it is possible that there could be some flow bypassing or short-circuiting, which would result in reduced performance. If this is the case, then the tuned number of segments is not as reflective of the relative mixing patterns compared to the other modules.

3.4.2 Effect of Flow Rates on Performance

The predicted and measured exiting concentrations are shown as a function of sweep flow rate for the three feed flow rates in Figure 3.7 for the single-pass module (Module 3). Overall, the model predicts the steady-state data reasonably well over the full range of flow rates studied. The main discrepancy appears in the retentate concentration at a high feed flow rate. However, it is important to keep in mind that the predictions were made using a model with only one fixed number of segments for all flow rates. Since mixing behaviour in the module can change with flow rate (or gas velocity), such small deviations are to be expected. Nonetheless, it was important to retain a single model (fixed number of segments for different flow rates), since the model was ultimately intended to be used to simulate performance under conditions with time varying flow rates.
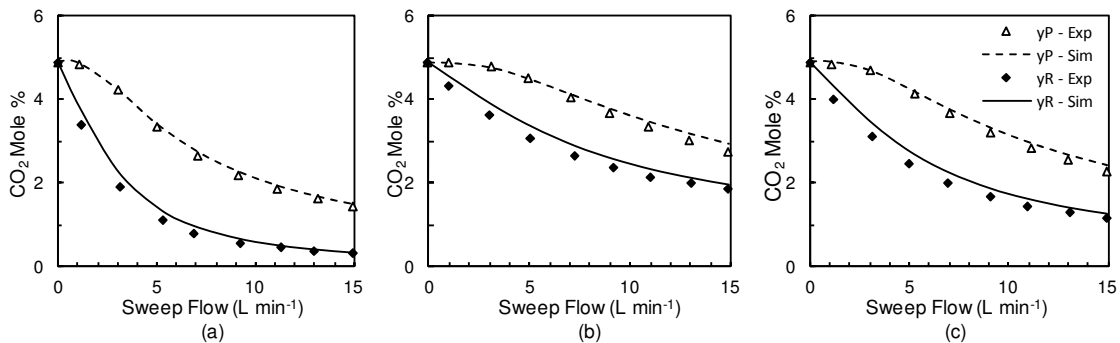
Figure 3.7. Single-pass permeate and retentate CO_2 concentration comparison of model predictions with experimental data over a range of sweep flow rates and a feed flow rate of (a) 5 L min^{-1}, (b) 10 L min^{-1}, and (c) 15 L min^{-1}.

3.4.3 Effect of Multiple Sweep Gas Passes

To optimize the mass transfer efficiency in the membrane module, a two-pass configuration was assembled so that the sweep gas was forced to enter through one section of the fibers

and return through the remaining fibers. The objective of this modification was to manipulate the flow so that the driving force in the low feed concentration regions would be increased, resulting in a higher purity (*i.e.* approaching a counter-current flow configuration). The predicted and measured retentate concentrations for the single- and double-pass membrane modules are shown in Figure 3.8a and b.
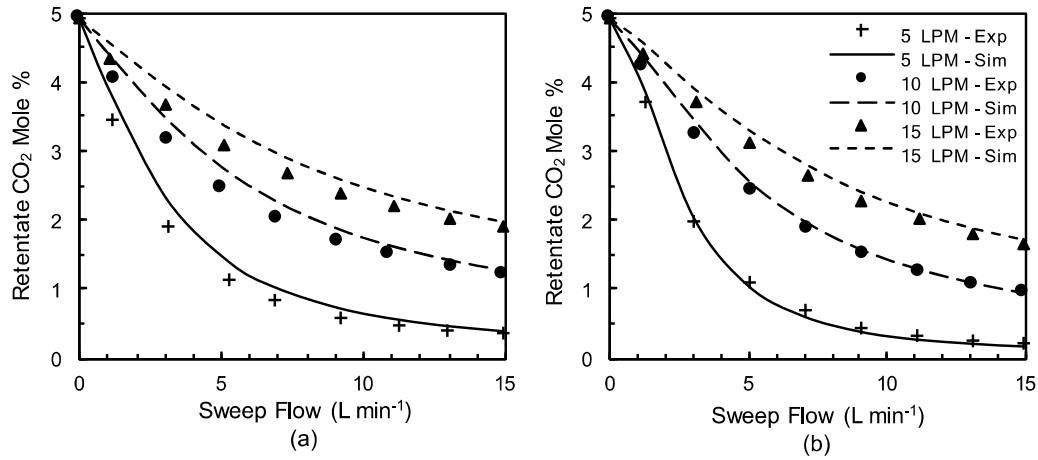
Figure 3.8. Retentate CO_2 concentration comparison of model predictions with experimental data for three feed flow rates over a range of sweep flow rates for two membrane modules: (a) single-pass (Module 3), and (b) double-pass (Module 4).

As expected, the retentate concentration obtained using the two-pass configuration was consistently lower than the single-pass version for very similar experimental conditions and membrane area. The model was also able to predict performance reasonably well in both cases.

3.4.4 Effect of Hollow Fiber Packing Density

The model was also used to explore the performance of two other double-pass modules with lower hollow fiber packing densities. The packing densities of these two additional modules were 21.3% and 30.2%, while the original module had a packing density of 45.4%. It is also worth noting that these membrane modules had a bundle diameter of 80 mm, compared to 100 mm for the original module. Therefore, the effective membrane surface area in these modules was significantly lower. The measured and predicted permeate and retentate concentrations as a function of sweep flow rate for the 10 L min^{-1} feed flow rate

are shown in Figure 3.9. The three-paneled figure shows the results for the 21.3% module (Module 1), the 30.2% module (Module 2), and the two-pass 45.4% module (Module 4).
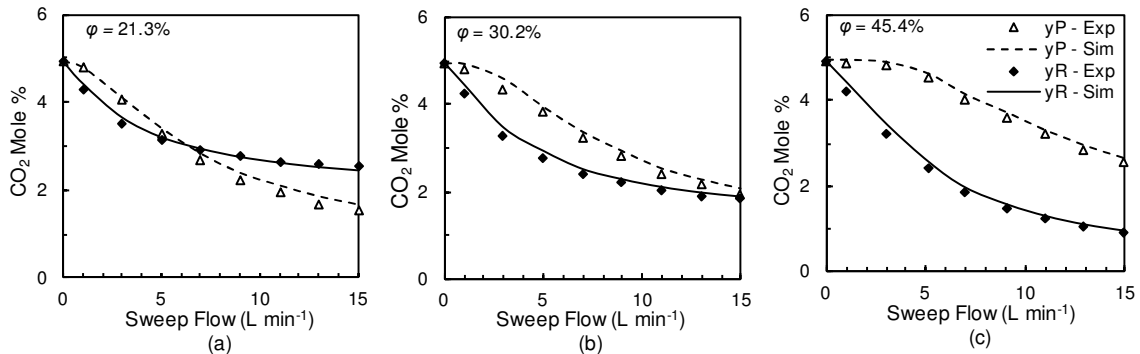
Figure 3.9. Permeate and retentate CO_2 concentration comparison of model predictions with experimental data for a feed flow rate of 10 L min^{-1} over a range of sweep flow rates for double-pass modules with packing densities of (a) 20.3% (Module 1), (b) 31.2 % (Module 2), and (c) 45.4% (Module 4).

The membrane area of the low packing density modules is considerably lower than in the standard module due to both the low packing density as well as the smaller bundle size. For the 21.3% module, the retentate concentration seems to level off at a sweep flow rate of 7 L min^{-1}. This seems to indicate that the amount of membrane surface area available for mass transfer is the limiting factor since increasing the sweep flow rate only has a small effect on the final retentate concentration at higher flow rates.

3.4.5 General Discussion

The model fits the experimental data relatively well when the number of segments is calibrated for each membrane module configuration. However, the physical interpretation of number of segments is more challenging than initially expected. The tanks-in-series model interpretation is that a greater number of segments indicates increased plug flow behaviour. Plug flow leads to better performance when compared to perfect mixing since the average driving force is higher. However, besides local mixing, other effects can also reduce performance. Therefore, when a small number of segments is predicted through model tuning, this may indicate more mixing, but it could also be due to other effects such as bypassing, which reduce the effective membrane area. This is quite possibly the case for the lowest packing density module.

33

For some of the cases, a certain model structure provided a best fit for the permeate measurements but a different structure gave a best fit for the retentate data. This discrepancy points to possible experimental error. One possible explanation could be a small leak in the membrane system. Another explanation could be the drift in mass spectrometer reading over the course of the experimental measurements. The simulations were based on the initial feed concentration, which was measured for a single point before the series of measurements for the range of flow rates. Additionally, there could have been small amounts of contaminants in the system during the initial feed concentration reading which may have skewed the feed concentration or subsequent measurements. One other explanation could be a small offset or measurement error in the flowmeters. Despite any weaknesses in the approach, the experimental data were consistent and the tuning procedure resulted in generally good model fits for the data. Therefore, the chosen modeling approach appears to be valid for this type of system.

3.5 Conclusions

Inhalation anesthesia is normally delivered through partial rebreathing circuits, which permit the reuse of anesthetic vapours but require the removal of CO_2. Currently, CO_2 removal is accomplished using soda lime absorbers, but by-products produced in these devices have been linked to negative health outcomes. Therefore, a simple membrane-based CO_2 separation system has previously been proposed for integration into the rebreathing circuit [18]. This study focused on the development and validation of a simple design model for the hollow fiber membrane modules proposed for this application. A series of steady-state experiments were performed to test the performance of four different membrane module configurations. A design model was then derived using a modified tanks-in-series formulation. Although the developed model can provide transient predictions, only steady-state simulations were presented in this study. Transient predictions will be validated in a future study. The experimental data were used to tune the number of segments in the model, and model predictions were compared to the experimental data for the full range of conditions.

The results indicated that the type of segmental design model proposed in this study could provide adequate predictions of steady-state performance of the membrane module over a

relatively wide range of operating conditions. Specifically, it was observed that the number of segments in the model did not need to be changed for different combinations of flow rates. This seems to suggest that mixing behaviour is only minimally affected by flow rate for the investigated module configurations and operating conditions. It was also observed that membrane model validity is relatively insensitive to the number of segments over a relatively broad range of combinations. It should therefore be possible to use the model for scale-up/down predictions with minimal need for model recalibration. It was shown that, as expected, double-pass configurations outperform single-pass module configurations. It was also observed that the module having the lowest hollow fiber packing density performed significantly different than the other modules. It was suggested that this decreased performance is likely due to increased mixing in the module, and could also be due to flow short-circuiting.

3.6 Nomenclature

Symbols

A_M	membrane area (m^2)
F	molar flow rate (mol s^{-1})
K_i	membrane permeance for component i (mol m^{-2} s^{-1} bar^{-1})
N_i	molar flow rate of component i across the membrane (mol s^{-1})
n	number of moles
P	bulk pressure (bar)
R	universal gas constant (m^3 bar K^{-1} mol^{-1})
RMSE	root-mean-square error
t	time (s)
T	system temperature (K)
V	total volume (m^3)
y_{Exp}	experimental mole fraction
y_{sim}	simulated concentration
y	molar fractions

Subscripts

A	discrete sub-section property
i	component i

35

F	feed
P	permeate
R	retentate
S	sweep

Chapter 4: Modeling a Membrane System for Anesthetic Gas Separation using Computational Fluid Dynamics

4.1 Introduction

In the recent years, hollow fiber membranes have become an important separation technology in a variety of applications. Despite being a relatively new separation process, membrane separations have been increasingly employed as an alternative to conventional separation methods. Advantages of hollow fiber membrane operations, such as a high mass transfer area to volume ratio, operational flexibility, and ease of scale-up, make it a desirable unit operation. Hollow fiber membranes have been studied for a wide variety of applications including CO_2 capture, wastewater treatment, pharmaceutical production, and many others. Membranes are also commonly used in medical applications. For example, patients with kidney failure commonly receive dialysis treatment, in which a membrane is used to remove excess waste solutes from the patient's blood. During cardiopulmonary bypass surgery, a polymeric membrane acts as an artificial lung (a so-called blood oxygenator) to facilitate the exchange of O_2 and CO_2 into and out of the blood, respectively.

The growing popularity of membrane technology has prompted significant mathematical modeling efforts. The performance of a membrane separation system depends on several factors. Simulation studies provide valuable insight into the influence of operating parameters and system configuration on the performance. Numerous modeling methodologies have been proposed, with varying degrees of complexity. During model development, it is important to consider the trade-off between model accuracy and computational burden. While a sophisticated high-fidelity model may provide more accuracy and insight into system complexities and physical mechanisms, these models take a long time to solve, which makes them less optimal to be used for parametric sensitivity studies and optimization. On the other hand, simplifying assumptions employed in design models usually provide fast results, but sometimes this comes at the expense of accuracy and/or detailed physical insight. It is therefore important to be mindful of the modeling objectives when striking a balance between simple and sophisticated modeling approaches.

A simplified segmental model was developed for the system being investigated in this study in Chapter 3. This model was derived to permit both steady-state and dynamic simulations. It was validated using experimental data and used to make predictions about the steady-state performance. The simplified design model was then used to perform sensitivity studies and predict the required membrane area. However, there are certain complexities (*e.g.*, flow patterns) that are not captured directly by the design model. Conversely, computational fluid dynamics (CFD) simulations provide a means for detailed analysis of local transport phenomena in such systems. Therefore, the primary goal of this study was to develop a detailed CFD model to provide more insight into the fundamental process governing the performance of the system, and to cross-validate the predictions of the design model with the more detailed CFD model. Since flow patterns are directly resolved by the CFD model, this model was also used in this study to determine the permeance of the membrane to key gases based on predictions of steady-state experimental data. These permeance values were previously used in the design model, and the model was shown to provide good predictions of the steady-state dataset.

Computational fluid dynamics generally refers to the use of numerical methods to determine how fluids flow through or around objects. Most commonly, the Navier-Stokes equations are solved along with the continuity equation to resolve multidimensional features of the flow. The information about the flow field can then be used to solve the energy and species equations, which are coupled to the Navier-Stokes and continuity equations through the velocity field and the physical properties of the fluid. Although there are a variety of methods available to solve these partial differential equations, finite volume and finite element methods are most commonly used in commercial and open-source software packages.

In this study, a CFD model was developed using a porous media approach to represent the hollow fiber membrane. COMSOL Multiphysics was used to implement and solve this model. The membrane system was modeled by approximating the hollow fiber membrane bundle zone as two communicating porous domains for the shell and tube sides of the membrane. Flow in the porous domain was described by the Brinkman equation, while the Navier-Stokes equation was solved in the zones of the module that do not contain fibers.

Separate species transport equations were solved on each side of the membrane, coupled with the separate flow fields, and the two porous domains were coupled by a source term representing mass transfer across the membrane.

4.2 System Overview

In this study, a dense hollow fiber membrane system is used for gas separation. The membrane module is composed of a cross-wound hollow fiber mat wrapped around a cylindrical tube. The fibers are potted at each end to separate the shell and tube-side flows. The assembly of the membrane and the hollow core will be referred to as the membrane bundle. The assembled membrane bundle was supplied by 3M, Membranes Business Unit, and then implanted into a custom housing (manufactured using SLS Rapid Prototyping, Stratasys Ltd., Eden Prairie, Minnesota, USA). To optimize the system performance, the membrane assembly was configured into a two-pass configuration using an O-ring on the bottom of the bundle to force the tube-side flow to take two passes through the module.

This membrane system was developed specifically for CO_2 removal from anesthesia rebreathing circuits using a sweep gas. In this application, the feed gas enters through the core on the shell side and flows radially outward across the membrane bundle. A sweep gas is administered to the outer pass of tubes and then returns through the inner pass. Figure 4.1 shows a schematic of the membrane bundle and housing, with indicated flow paths.

For this study, the feed was assumed to be a mixture of 5% CO_2 in O_2 and pure O_2 was used as the sweep gas. The 5% CO_2 feed stream is representative of a typical exhaled stream from a patient during anesthesia, but it is a simplification because the actual gas would also contain anesthetic vapors, nitrogen, and water vapor.
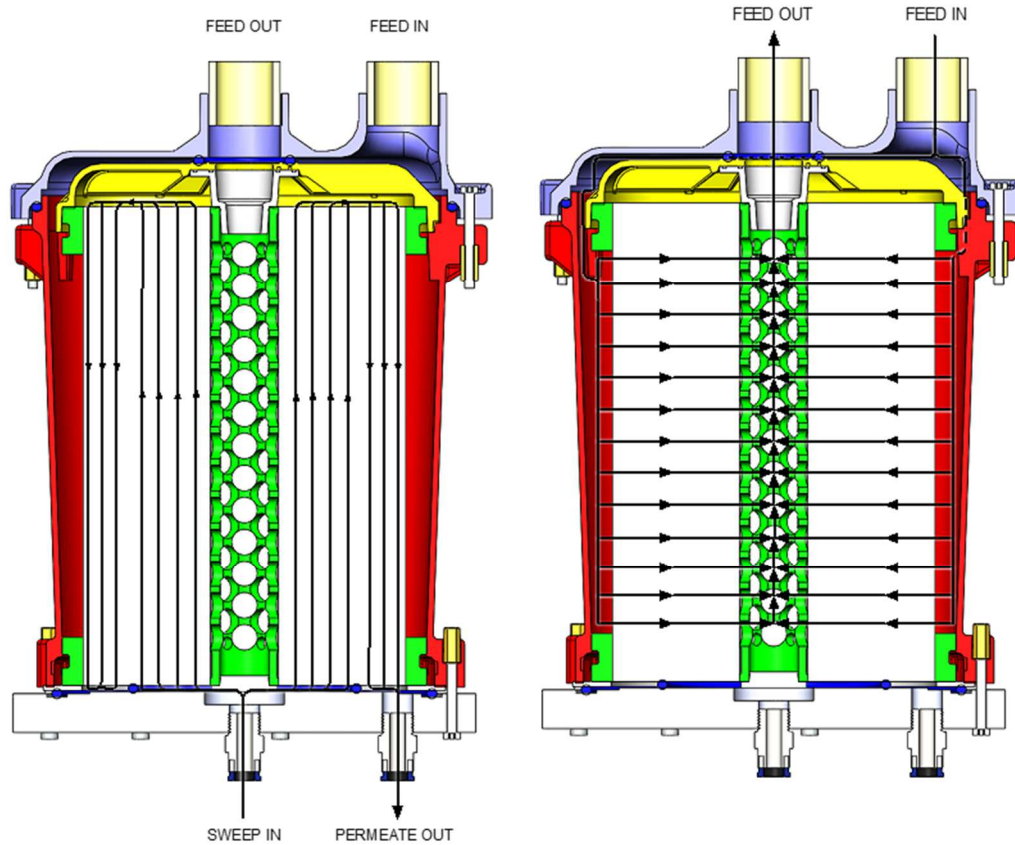
Figure 4.1. Schematic of two-pass membrane module in its housing showing the flow paths for (a) the sweep on the tube-side and (b) the feed on the shell-side.

As described in the previous study [26], the hollow fibers were an asymmetric polymethylpentene (PMP) membrane with a thin dense skin. The geometrical parameters and characteristics of the membrane module are summarized in Table 4.1.

Table 4.1. Membrane module parameters

Parameter	Value
Membrane material	PMP
Active membrane area (m^2)	2.10
Packing density	0.45
Fiber inner diameter (μm)	200
Fiber outer diameter (μm)	380
Number of fibers	29500
Active membrane length (mm)	120
Core diameter (mm)	20
O-ring diameter (mm)	70
Bundle diameter (mm)	100
Housing diameter (mm)	119

4.3 Model Description

4.3.1 Geometry

To generate the cylindrical geometry of the membrane module, the fluid domain was represented using a two-dimensional, axisymmetric coordinate system. The shell and tube-sides of the membrane were represented as two separate domains, coupled by the mass transfer rate through the membrane. Figure 4.2 shows a flow diagram of the two-dimensional computational domain and the resulting three-dimensional geometry. For the shell-side, the feed flow rate enters through the core in the center of the domain, flows outward through the membrane bundle, and then exits through a gap at the outer radius of the housing. The core in the center of the bundle and gap at the outer radius do not contain fibers and are free from other obstructions. Conversely, the bundle contains blockages due to the presence of the hollow fibers, and therefore this region was modeled as a porous medium. For the tube-side, the sweep enters a porous domain through the outer division of the bundle at the bottom of the module, flows up to the top of the module, and enters a hollow zone. Subsequently, it is forced back down through the inner pass of the bundle.
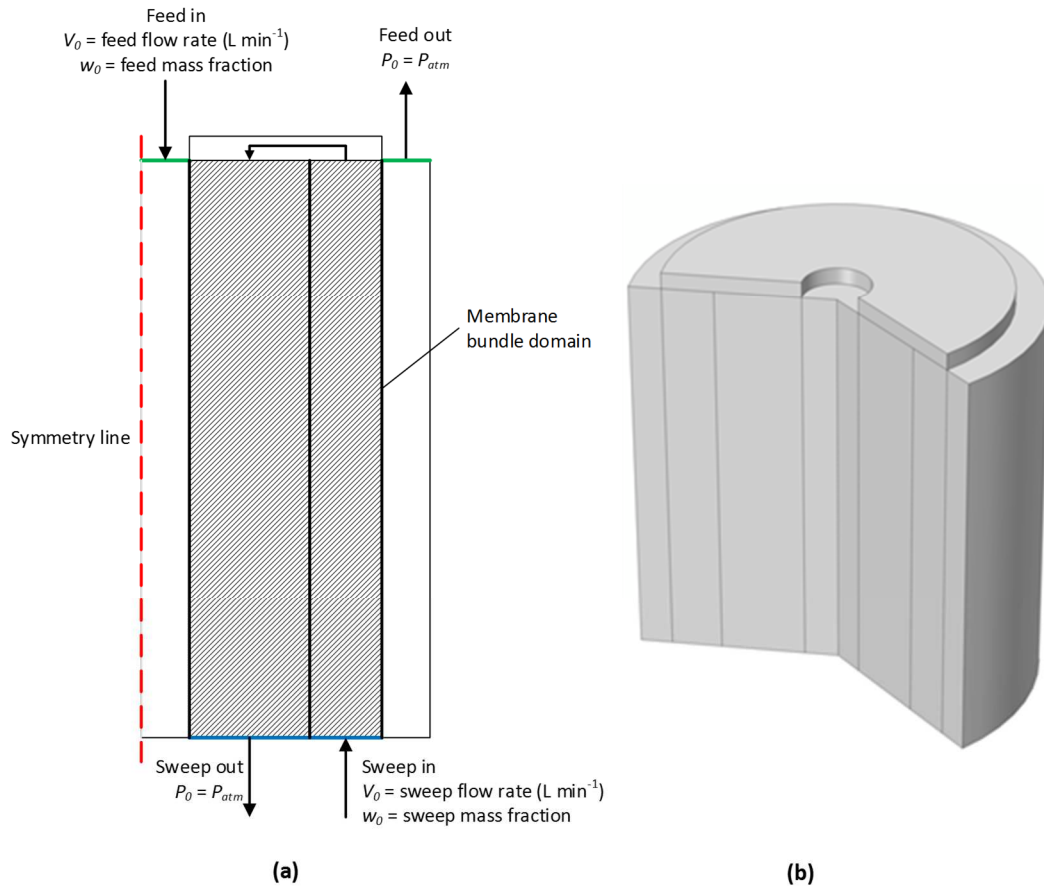
Figure 4.2. (a) Diagram of membrane module represented over two-dimensional axisymmetric model domain showing feed and sweep flows used in steady-state simulations, and (b) computational domain rotated around the line of symmetry.

The shell and tube sides of the membrane were represented using two separate porous domains, with their own porous media properties defined based on the module geometry. In the regions where there is no membrane bundle (inner core, sweep mixing region, outer housing), no extra resistance was added to the momentum equations. The boundary conditions for the two domains are summarized in Figure 4.3.
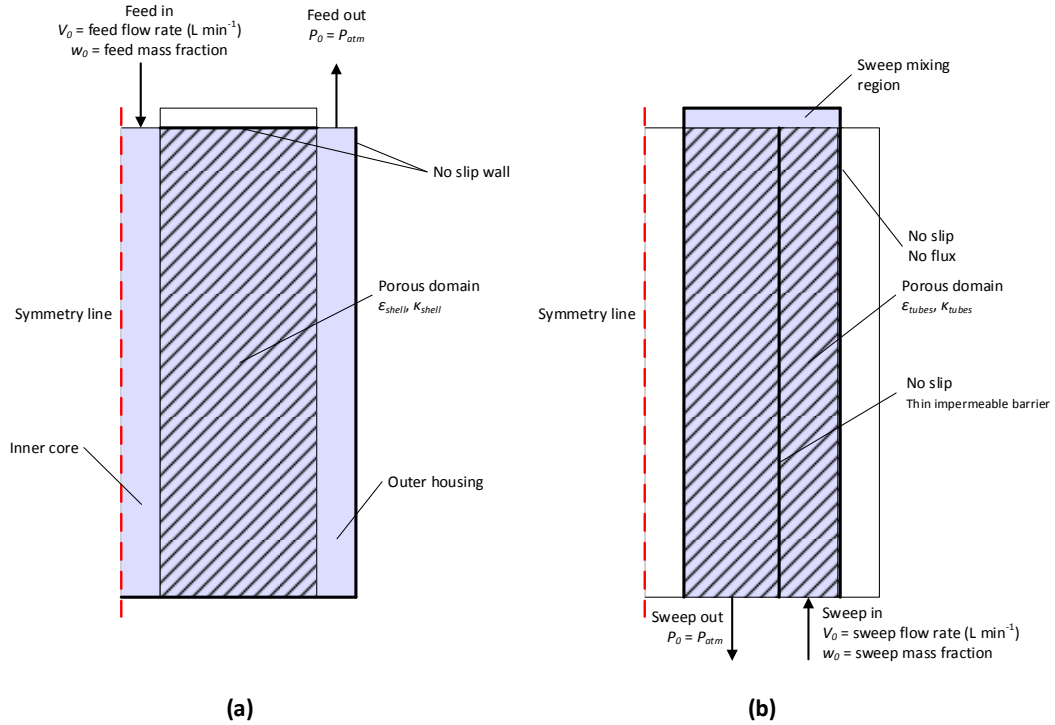
Figure 4.3. Boundary conditions implemented in the COMSOL model for the (a) shell-side and (b) tube-side.

4.3.2 Governing Equations

The flow fields were obtained by solving the momentum conservation equations and the continuity equations for constant viscosity, isothermal, laminar flow. The appropriateness of the laminar flow assumption was confirmed by calculating the Reynolds number for extreme flow rates in high velocity regions. The Reynolds number of the feed entering the core ($d = 0.02$ m) at 18 L min^{-1} with a density and viscosity of 1.2 kg m^{-3} and 1.85×10^{-5} kg m^{-1} s^{-1}, respectively was calculated using the following equation:

$$Re = \frac{\rho u d}{\mu} \tag{4.1}$$

where ρ is the density (kg m^{-3}), d is the core diameter (m), μ is the dynamic viscosity (kg m^{-1} s^{-1}), and u is the average velocity (m s^{-1}) calculated from the flow rate and cross-sectional area of the core ($u = 0.95$ m s^{-1}). The resulting Reynolds number with the described values is 1238, which is within the laminar flow regime for flow in a duct (Re < 2300) [39].

43

In the zones that did not contain hollow fibers (so-called free flow zones), the Navier-Stokes equations were solved together with the continuity equations to determine the velocity and pressure fields. For a single side of the membrane k:

$$\rho_k \frac{\partial u_k}{\partial t} + \rho_k (u_k \cdot \nabla) u_k = \nabla \cdot \begin{bmatrix} -P_k \boldsymbol{I} + \mu_k (\nabla u_k + (\nabla u_k)^T) \\ -\frac{2}{3} \mu_k (\nabla \cdot u_k) \boldsymbol{I} \end{bmatrix} + F_k \tag{4.2}$$

$$\rho_k \nabla \cdot u_k = 0 \tag{4.3}$$

where k refers to either the shell or tube-side of the membrane, u_k is the superficial velocity on the kth side of the membrane (m s^{-1}), P_k is the fluid pressure (Pa), ρ_k is the fluid density (kg m^{-3}), μ_k is the dynamic viscosity (kg m^{-1} s^{-1}), and F_k includes any additional volume forces (N m^{-3}). Additional volume forces (*e.g.*, gravity) were neglected in this model. As mentioned above, the system was assumed to be isothermal. The mixture density was calculated using the ideal gas law, and therefore varied only with concentration and pressure.

For the porous domains, the Brinkman equations were solved together with the continuity equation to obtain the pressure and velocity fields in the system. The momentum and continuity equations for the porous zones are given by:

$$\frac{\rho_k}{\varepsilon_k} \left(\frac{\partial u_k}{\partial t} + (u_k \cdot \nabla) \frac{u_k}{\varepsilon_k} \right) = \nabla \cdot \begin{bmatrix} -P_k \boldsymbol{I} \\ +\frac{\mu_k}{\varepsilon_k} (\nabla u_k + (\nabla u_k)^T) \\ -\frac{2\mu_k}{3\varepsilon_k} (\nabla \cdot u_k) \boldsymbol{I} \end{bmatrix} - \left(\frac{\frac{\mu_k}{\kappa_k}}{+\frac{S_{total,k}}{\varepsilon_k^2}} \right) u_k + F_k \tag{4.4}$$

$$\rho_k \nabla \cdot u_k = S_{total,k} \tag{4.5}$$

where κ_k is the permeability of the porous medium (m^2), ε_k is the porosity, and $S_{total,k}$ is the total mass source term due to membrane permeation (kg m^{-3} s^{-1}). The source term is the sum of the component transfer rates across the membrane per unit volume.

The mass transport is governed by the species conservation equations, and was resolved over the complete domain. Separate species equations were solved on each side of the membrane (*i.e.*, using the separate flow fields), and these equations were coupled through

44

source terms in the porous zones. The species conservation equation for a single species i on side k of the membrane is given by:

$$\rho_k \frac{\partial w_{i,k}}{\partial t} + \rho_k(u_k \cdot \nabla)w_{i,k} = -\nabla \cdot j_{i,k} + S_{i,k} \tag{4.6}$$

where $w_{i,k}$ is the mass fraction of component i on side k of the membrane, ρ_k is the mixture density (kg m^{-3}), $j_{i,k}$ is the diffusion mass flux of species i relative to the mass average velocity (kg m^{-2} s^{-1}), and $S_{i,k}$ is the mass source of species i on side k of the membrane (kg m^{-2} s^{-1}). The source term was set to zero in the membrane-free domains and in the porous domains it was set equal to the flux across the membrane. In the membrane-free zones, the superficial velocity term was used, and in the porous zones the interstitial velocity was used. The interstitial velocity is defined as the superficial velocity divided by the porosity.

Fick's law was assumed to be adequate to represent the diffusion mass flux of species i:

$$j_{i,k} = -\left(\rho_k D_{i,k} \nabla w_{i,k} + \rho_k w_{i,k} D_{i,k} \frac{\nabla M_k}{M_k}\right) \tag{4.7}$$

Where $D_{i,k}$ is the diffusion coefficient of component i in the mixture on side k of the membrane (m^2 s^{-1}), and M is the average molar mass of the mixture (g mol^{-1}).

In Chapter 3, the solution-diffusion model was used to determine the permeation rates of individual species across the membrane. Therefore, this study will also apply this model. Using the solution-diffusion model and assuming ideal gas behaviour, the molar permeation rate of species i through the membrane can be determined by multiplying the permeance by the partial pressure driving force and the surface area:

$$N_i = K_i A_M\left(y_{i,R} P_R - y_{i,P} P_P\right) \tag{4.8}$$

Where N_i is the molar flow rate of component i across the membrane (mol s^{-1}), K_i is the membrane permeance for component i (mol m^{-2} s^{-1} bar^{-1}), A_M is the membrane area (m^2), $y_{i,R}$ and $y_{i,P}$ are the molar fractions of component i on the retentate and permeate sides of the membrane, and P_R and P_P are the bulk pressures (bar) on the retentate and permeate sides. This molar permeation rate can be converted into a volumetric mass source term

45

through multiplication by the surface area density of the membrane (m^2 of membrane surface area per m^3), a, and the molar mass of the permeating species. Therefore, the volumetric mass source terms for the species equations are given by:

$$S_{i,R} = -K_i M_i \left(\frac{w_{i,R}/M_i}{\sum w_{i,R}/M_i} P_R - \frac{w_{i,P}/M_i}{\sum w_{i,P}/M_i} P_P \right) a \qquad (4.9)$$

$$S_{i,P} = K_i M_i \left(\frac{w_{i,R}/M_i}{\sum w_{i,R}/M_i} P_R - \frac{w_{i,P}/M_i}{\sum w_{i,P}/M_i} P_P \right) a \qquad (4.10)$$

where K_i is the membrane permeance for species i (mol m^{-2} s^{-1} bar^{-1}), M_i is the molar mas of species i (g mol^{-1}), $w_{i,R}$ is the local retentate mass fraction, $w_{i,P}$ is the permeate mass fraction, P_R is the local pressure on the retentate side of the membrane (bar), P_P is the local pressure on the permeate side of the membrane (bar), and a is the membrane surface area per unit of volume in the membrane bundle (m^{-1}).

The volumetric total mass source terms for the retentate and permeate in the porous zones are simply the sum of the species source terms:

$$S_{total,R} = \sum S_{i,R} \qquad (4.11)$$

$$S_{total,P} = \sum S_{i,P} \qquad (4.12)$$

4.3.3 Numerical Details

The model described above was implemented using COMSOL Multiphysics version 5.2 [40], a commercial general-purpose multiphysics simulation software which uses finite element analysis to solve coupled partial differential equations numerically with the appropriate boundary conditions. Both steady-state and dynamic simulations were performed. A mapped mesh was generated over the computational domain and the number of elements was increased until a mesh independent solution was obtained. Figure 4.4 shows two results from the mesh refinement study. Figure 4.4a compares the radial velocity profile as a function of the horizontal coordinate on the shell-side of the membrane for three different mesh resolutions. Figure 4.4b shows how the predicted exiting retentate mass fraction varies with mesh resolution. Other values were also compared, and the

differences between simulations using various mesh densities were also compared visually. Finally, a mesh with 22365 quadrilateral elements was considered to be sufficient to ensure accuracy for the simulations in this study. This mesh, shown in Figure 4.5, was used in all simulations.
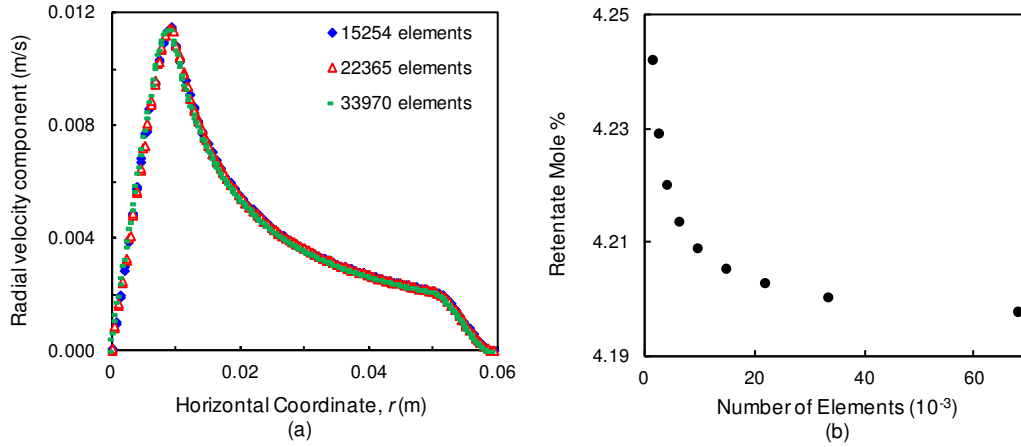
Figure 4.4. Effect of the number of mesh elements on the (a) radial shell-side velocity over the radial coordinate, and (b) predicted outlet retentate concentration.
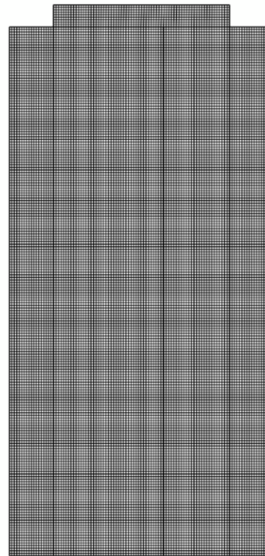
Figure 4.5. Representation of the mapped mesh used for the simulations (22365 quadrilateral elements).

Table 4.2 contains the parameters used in the COMSOL model.

Table 4.2. Parameters used in COMSOL model

Parameter	Value	Units
Viscosity, μ	$1.5\text{x}10^{-5}$	Pa s
Shell porosity, ε_s	0.55	-
Tube porosity, ε_t	0.12	-
Shell permeability, κ_s	$2.0\text{x}10^{-9}$	m^2
Tube permeability, κ_t	$1.0\text{x}10^{-10}$	m^2
O_2 diffusion coefficient, D_{CO2}	$1.5\text{x}10^{-5}$	$m^2\,s^{-1}$
O_2 diffusion coefficient, D_{O2}	$1.5\text{x}10^{-5}$	$m^2\,s^{-1}$
N_2 diffusion coefficient, D_{N2}	$1.5\text{x}10^{-5}$	$m^2\,s^{-1}$
Membrane area to volume ratio, a	2230	m^{-1}

Permeability is a proportionality constant which relates superficial velocity to pressure drop in porous media by Darcy's Law [41]. A smaller permeability translates to higher resistance to flow. Rough estimates of the permeability for the effective shell and tube-side porous media were calculated using empirical equations. The shell-side permeability was approximated using the Blake-Kozeny equation for flow in packed columns [39], [42]. The Blake-Kozeny equation is the frictional component of the Ergun equation. The tube-side permeability was estimated based on the Hagen-Poiseuille equation for laminar flow in straight pipes [43], [44].

4.3.4 Simulation Conditions

4.3.4.1 Steady-state Simulations

A series of steady-state experiments was performed to provide validation and tuning data for the model. The experimental method was already described in detail in a previous study (Chapter 3). In these experiments, pure O_2 was used as the sweep gas, and a 5% CO_2 in O_2 mixture was used as the feed. After measuring the initial feed concentration, using a quadrupole mass spectrometer, the feed was supplied to the shell-side of module and the sweep was supplied to the tubes at predetermined flow rates. The feed flow rates were 5, 10 and 15 L min^{-1}, and the sweep flow rates were 1, 3, 5, 7, 9, 11, 13 and 15 L min^{-1}.

Since the mass spectrometer can only monitor one gas at a time, the retentate and permeate concentrations were measured separately. First, the retentate outlet concentration was monitored continuously by the mass spectrometer for the full range of flow rates. The flow conditions were then replicated and the feed outlet concentration was measured continuously. Figure 4.6 shows a diagram of the experimental configuration.
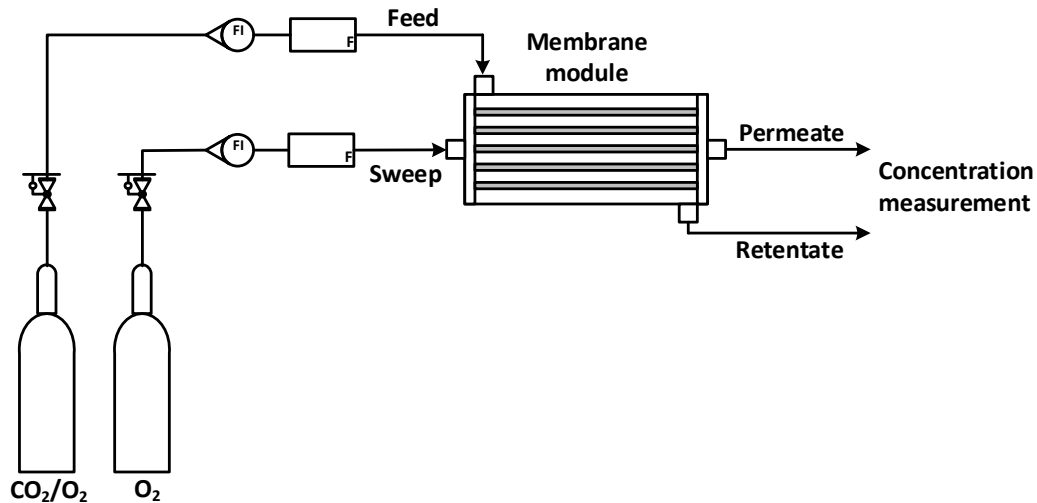
Figure 4.6. Schematic of experimental setup for steady-state permeation measurements.

In this study, simulations were performed to match all steady-state experimental conditions. The membrane permeance for CO_2 was then adjusted to fit the model to the experimental data. The ratio of the CO_2 permeance to the O_2 permeance of the membrane (often called the ideal separation factor or selectivity of the membrane) was assumed to be 2.5. Similarly, the ratio of the CO_2 permeance to the N_2 permeance of the membrane was assumed to be 10. These values were based on pure gas permeation experiments that were performed with smaller samples of the membrane [26].

4.3.4.2 Dynamic Tracer Simulations

In addition to using the CFD model to determine the permeance of CO_2 through the membrane, another major objective of this study was to investigate the detailed steady-state and dynamic behaviour of the membrane system. A comparison between the predictions made by the previously developed design model (Chapter 3) and the present CFD model under dynamic conditions is provided in a subsequent study (Chapter 5). This study provides an analysis of the concentration distributions and flow patterns existing

within the membrane under steady-state and dynamic conditions. A useful way to assess the flow regime and mixing behavior in a system is by analyzing the residence time distribution. The residence time distribution may be obtained by injecting an inert tracer into the system and monitoring the exit response.

The tracer input was implemented as a time-dependent inlet concentration boundary condition. The input concentration was modeled using a Gaussian distribution with a variance of 0.025 seconds and a mean of one second. The peak concentration was arbitrarily scaled to a mass fraction of 0.16. The same input was used for each simulation, so the residence time distribution curves (*E(t)*) are directly proportional to the concentration.

Simulations were performed to study the tracer response of both the shell and tube-side of the membrane separately. For the shell-side tracer, a steady flow rate of O_2 was supplied to the shell-side of the membrane, while all ports on the tube side were plugged. The tracer was then injected according to the Gaussian distribution at the shell-side inlet. For the tube-side tracer, a steady flow rate of O_2 was supplied to the tube-side of the membrane, while all ports of the shell side were plugged. The tracer was then injected at the tube-side inlet.

Experimental tracer studies are typically executed with an inert tracer so that the results can be attributed to flow patterns directly, without consideration of reaction or permeation rates. However, in practice it is difficult to find a truly impermeable species or a method of preventing permeation that would not impact the properties of the membrane in further tests. Therefore, both permeable and non-permeable tracer simulations were performed in this study to facilitate comparison.

4.3.5 Residence Time Distribution Theory

The flow regime and mixing behaviour of flow reactors may be experimentally assessed by performing a residence time distribution (RTD) study. A complete description and derivation of the relevant equations is detailed in Levenspiel [45]. The experimental RTD profile can be compared to a predicted response for ideal flow to evaluate the degree of non-idealities and characterize the flow regime. The RTD is obtained experimentally by

injecting an inert tracer into the system and monitoring the response as it exits the system. For a pulse injection, the RTD is calculated using the following equation:

$$E(t) = \frac{C(t)}{\int_0^\infty C(t)dt} \tag{4.13}$$

where C is the tracer concentration leaving the system at time t (in seconds). The RTD may then be used to determine average experimental residence time:

$$t_m = \frac{\int_0^\infty tC(t)dt}{\int_0^\infty C(t)dt} \tag{4.14}$$

where t is time after the pulse injection and t_m is the mean residence time (both in units of seconds). It is often useful to compare the mean residence time calculated from the tracer curve to the theoretical space-time (τ) estimated from the volume and flow rate:

$$\tau = \frac{V}{\dot{V}} \tag{4.15}$$

Where V is the flow volume (L), $\dot{V}$ is the volumetric flow rate (L s^{-1}), and τ is the space-time (s). For the membrane system, the volume in the tubes and the volume on the shell side is used for the respective space-time calculation.

The average residence time may be compared to the theoretical residence time to assess the degrees of mixing and identify the presence of non-idealities such as stagnant areas, channeling, or dead space. A residence time smaller than the space-time suggests that there may be dead zones or stagnant regions in the system, since the effective volume is smaller than the reactor volume. Likewise, a residence time that is greater than the space-time could be interpreted as the tracer flowing through a volume larger than the reactor volume [45].

The spread of the pulse tracer may be characterized by calculating the variance (σ^2) of the $E(t)$ curve:

$$\sigma^2 = \frac{\int_0^\infty t^2 C(t)dt}{\int_0^\infty C(t)dt} - t_m^2 \tag{4.16}$$

51

The variance has units of s^2. The variance may also be expressed in dimensionless form to allow a comparison of cases with different residence times. It is often useful to non-dimensionalize the RTD profile to permit a comparison for different flow rates and reactor volumes. The dimensionless time (θ) is given by:

$$\theta = \frac{t}{t_m} \tag{4.17}$$

The dimensionless variance is given by:

$$\sigma_\theta^2 = \frac{\sigma^2}{t_m^2} \tag{4.18}$$

The experimental mean residence time and variance may then be compared to the modeled parameters to assess the degree of variation from ideal flow models. For the tanks-in-series model, the number of representative tanks is the inverse of the dimensionless variance:

$$N = \frac{1}{\sigma_\theta^2} \tag{4.19}$$

The validity of the experimental residence time distribution relies on the tracer being truly inert, so that the response obtained is due only to hydrodynamics and not impacted by other effects (*e.g.*, reaction, permeation, *etc.*). A truly inert tracer must be non-reactive to ensure that the response is based only on flow conditions. The tracer should also be similar to the flow phase, so that it does not disrupt the flow patterns when it is injected. However, this may be challenging in membrane systems because many of the tracer choices may permeate across the membrane, creating local mass transfer phenomena, and altering the exit distribution. One way to prevent this is to fill the opposite side of the membrane with water (or another liquid) to prevent membrane permeation. However, this is not always possible because filling the membrane with water could alter the permeation characteristics of the membrane. As a result, the tracer used in the subsequent experimental study (Chapter 6) has a low, but not negligible, permeance across the membrane. However, the CFD model can be used to assess the degree of influence that permeation has on the obtained residence time distribution. The response of a permeating and non-permeating tracer is compared below. Since the RTD cannot be experimentally validated with an inert tracer, the

permeating tracer will be used to help validate the flow patterns. In the CFD simulations, a non-permeating tracer can easily be obtained by setting the permeance across the membrane to zero.

4.4   Results and Discussion

4.4.1 Membrane Permeance Calibration

The CFD model was used to estimate the membrane permeance of CO_2. To accomplish this, the model was executed with the conditions used in the steady-state experiments, using varying values of the permeance. The predicted permeate and retentate concentrations were then compared to the experimental values. To be consistent with experimental measurements, the average outlet mass fraction in the simulations was calculated by dividing the component mass flow rate by the total mass flow rate:

$$w_i = \frac{\int_{r1}^{r2} w_i \rho u 2\pi r dr}{\int_{r1}^{r2} \rho u 2\pi r dr} \tag{4.20}$$

Where r_1 and r_2 are the inner and outer radius of the outlet specific area. The mass fraction was then converted to molar units and compared to the experimental results. The membrane permeance used in the model was adjusted to obtain results close to those measured in the experiment over the full range of flow rates. Figure 4.7 shows the experimental and simulated results with three different permeance values.
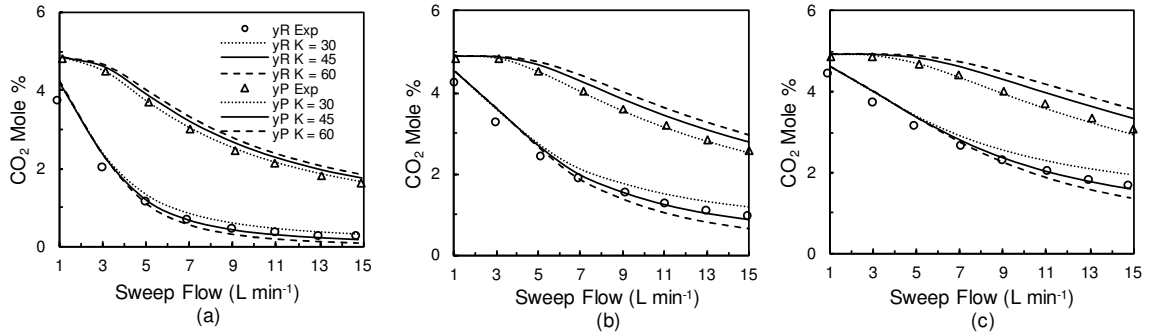
Figure 4.7. Retentate and permeate CO_2 concentration simulated using three membrane permeance values compared to experimental results over a range of sweep flow rates and feed flow rates of (a) 5 L min^{-1}, (b) 10 L min^{-1}, and (c) 15 L min^{-1}.

The fitting procedure resulted in a global best fit CO_2 permeance of 45 mol m^{-2} h^{-1} bar^{-1}. A parity plot showing the comparison of predicted and experimental outlet retentate and permeate concentrations is shown in Figure 4.8. Despite a small offset at higher outlet concentrations, the fitted permeance is able to provide a good prediction of the experimental data.
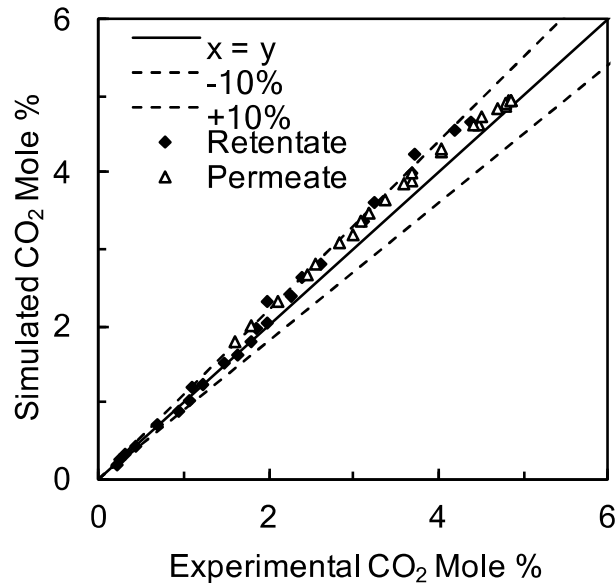
Figure 4.8. Parity plot of experimental and simulated CO_2 mole fraction using the final calibrated membrane permeance.

Variations of the PMP membrane used in this study have been characterized in detail in a separate study [26]. Different iterations of the membrane were formed under a range of conditions, which altered the separation performance. These membranes were supplied as

miniature modules and were characterized in detail. Unfortunately, the actual membrane variation used in the steady-state experiments in this study was not characterized using this approach. However, the selectivity of CO_2 over O_2 and N_2 was similar for different membranes that were tested. Since data was not available to determine the permeance of these components, it was instead calculated using the average pure gas selectivity measured in the characterization study. Given the good fit of the model to the experimental data, this procedure appears to be reasonable. The resulting permeance for the three gases are shown in Table 4.3.

Table 4.3. Calibrated membrane permeance

Membrane permeance (mol m^{-2} h^{-1} bar^{-1})		
CO$_2$	O$_2$	N$_2$
45.0	18.0	4.5

4.4.2 Steady-state Velocity Profile

One purpose of the CFD model was to allow visualization of the velocity and concentration profiles within the module to help identify potential inefficiencies in the configuration. Given the configuration (*i.e.*, locations of the inlet and outlet ports), the shell-side of the hollow fiber membrane modules could be particularly susceptible to flow maldistribution, which would reduce the effective membrane area and thereby also the separation performance. Figure 4.9 shows the two-dimensional steady-state velocity profiles on the shell side for different flow rates.
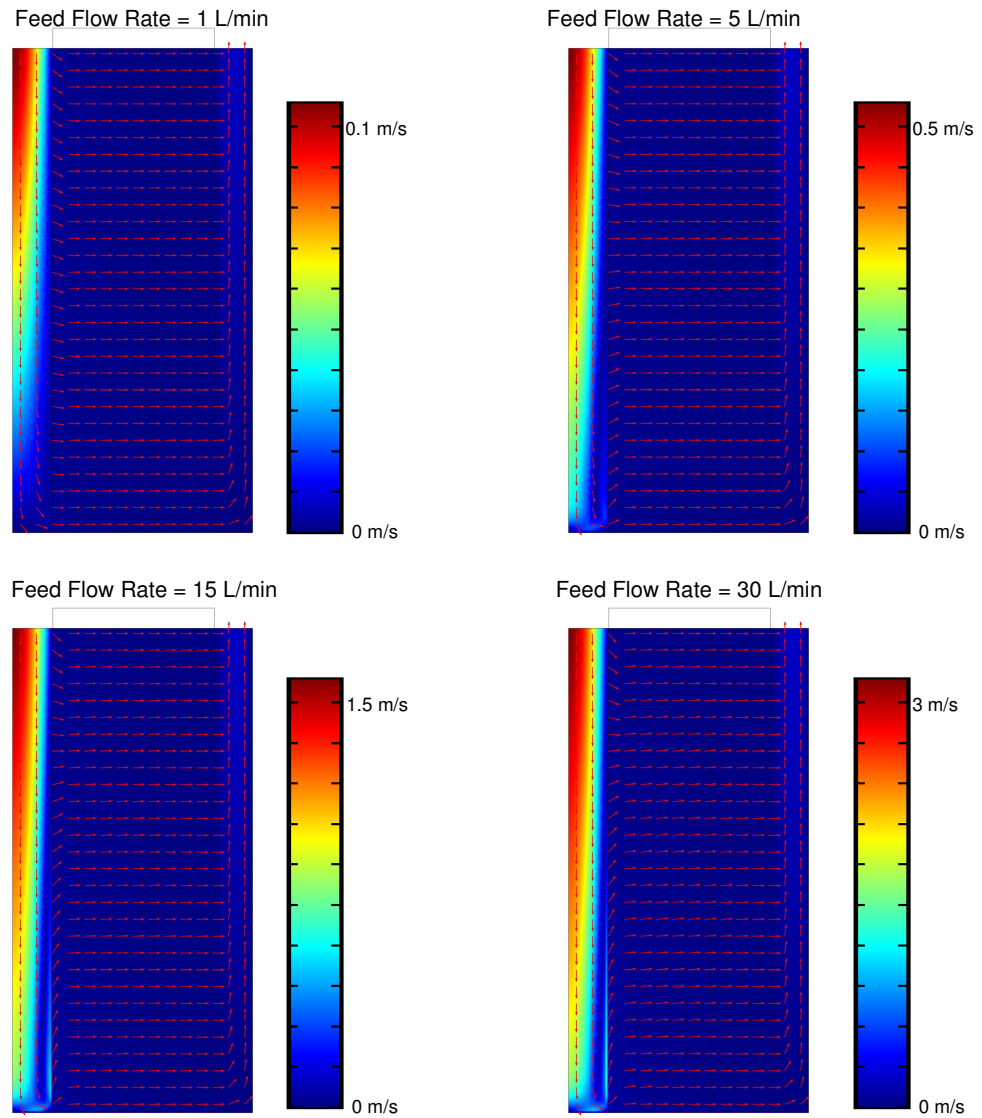
Figure 4.9. Steady-state shell-side velocity profiles for feed flow rates of 1 L min⁻¹ (top left), 5 L min⁻¹ (top right), 15 L min⁻¹ (bottom left), and 30 L min⁻¹ (bottom right). Colours indicate velocity magnitude and vectors indicate direction.

Clearly, higher flow rates lead to increasing recirculation in the velocity field at the bottom of the inner core. This is interesting because it could lead to maldistribution across the membrane bundle, which would reduce the membrane performance. However, for the membrane investigated in this study, the amount of maldistribution resulting from this recirculation was not significant. This is a direct result of the relatively high packing

density used for the hollow fibers. Lower packing densities would result in more maldistribution.

The tube-side velocity profile for a flow rate of 15 L min^{-1} is shown in Figure 4.10. As expected, given the geometry of the tube side and the higher flow resistance, the velocity distribution on the tube side was not significantly affected by the flow rate over the studied range.
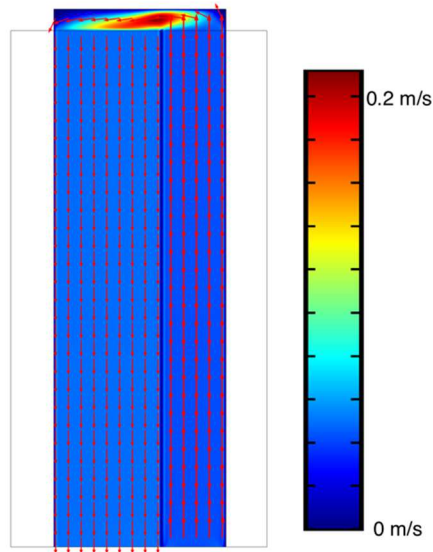
Figure 4.10. Steady-state tube-side velocity profile for a flow rate of 15 L min^{-1}. Colours indicate velocity magnitude and vectors indicate direction.

4.4.3 Steady-state Concentration Distribution

The two-pass configuration was developed to optimize the sweep gas efficiency in regions with low feed-side concentrations. Figure 4.11 shows the CO_2 concentration on the shell (feed) side and tube (sweep) side of the membrane for feed flow rates of 5, 10 and 15 L min^{-1} and a constant sweep flow rate of 10 L min^{-1}. The feed gas concentration was 5 mol% CO_2 in O_2.
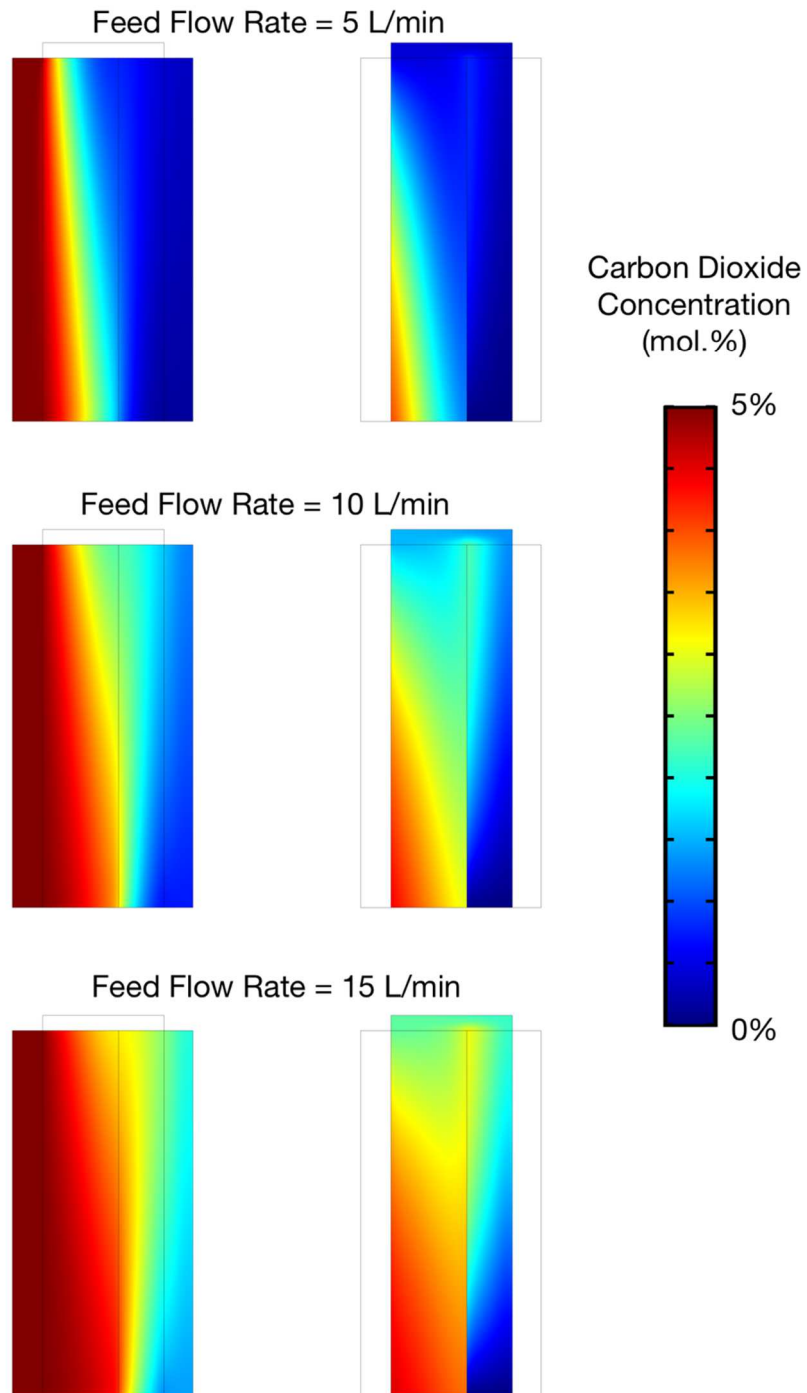
Figure 4.11. CO_2 concentration on the shell side (left column) and tube side (right column) for a 5 mol% CO_2 in O_2 feed stream with flow rates of 5 L min^{-1} (top), 10 L min^{-1} (middle) and 15 L min^{-1} (bottom), and a pure O_2 sweep stream with a flow rate of 10 L min^{-1}.

Regions of high CO_2 concentration are indicated by dark red and low concentrations are dark blue. As previously shown in Figure 4.11, the feed gas enters at the top of the module through the core, flows radially outward across the bundle, and then exits through the gap

between the bundle and housing. Conversely, the sweep gas enters at the bottom on the outer pass, flows upward through the tubes and mixing zone, and then returns downward through the inner pass.

The concentration contours on Figure 4.11 clearly indicate that, as expected, CO_2 is transferred from the shell-side of the membrane to the sweep gas on the tube side. The results also show that the concentration leaving the outer edge of the membrane bundle is relatively uniform for all flow rates, indicating that the two-pass configuration is useful in reducing the exiting retentate concentration.

Although not presented in detail in this study, a single-pass configuration shows a much larger axial variation in the shell-side concentration flowing through the bundle. This effect was explored in more detail in a separate study [18], and an example is shown in Figure 4.12.
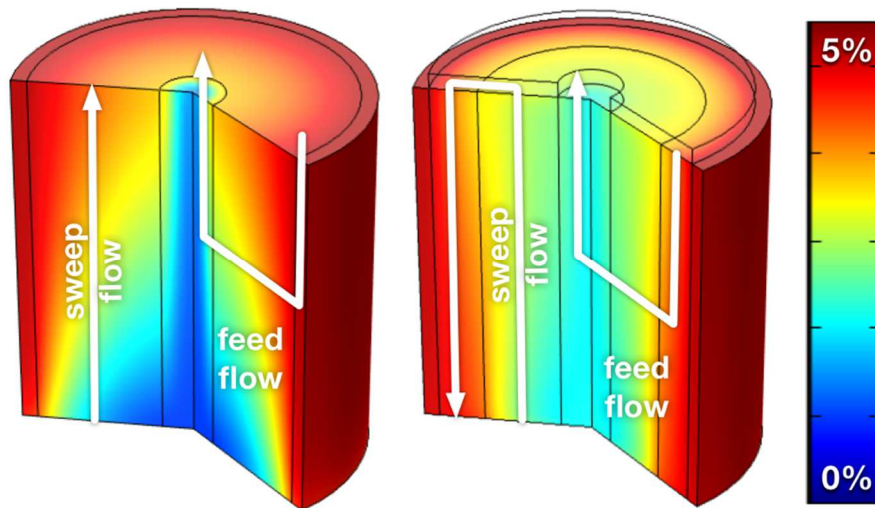
Figure 4.12. Retentate CO_2 concentration distribution comparison for a single-pass module (left) and double-pass module (right) with a feed flow rate of 15 L min^{-1} and sweep flow rate of 10 L min^{-1}. Figure reproduced from reference [18].

On the tube-side of the membrane, the sweep gas becomes enriched in CO_2 as it flows upward and is contacted by the feed gas. On the second (outer) pass, the sweep gas is further enriched as it flows downward.

Although using more than two sweep passes would obviously result in even more efficient use of the sweep gas, the two-pass configuration is a relatively good compromise between efficient use of sweep gas and complexity in module design/assembly.

4.4.4 Residence Time Distribution

4.4.4.1 Shell-side Tracer Simulations

For shell-side tracer simulations, a constant flow rate and a time-dependent input concentration pulse was applied to the shell-side of the membrane, while the tube side was effectively closed. Since the same input was used for each simulation, the residence time distribution curves ($E(t)$) are directly proportional to the concentration. The residence time distribution of the shell side for three flow rates is shown in Figure 4.13 for a non-permeating ($K = 0$) tracer (Figure 4.13a) and for the permeating N_2 tracer (Figure 4.13b).
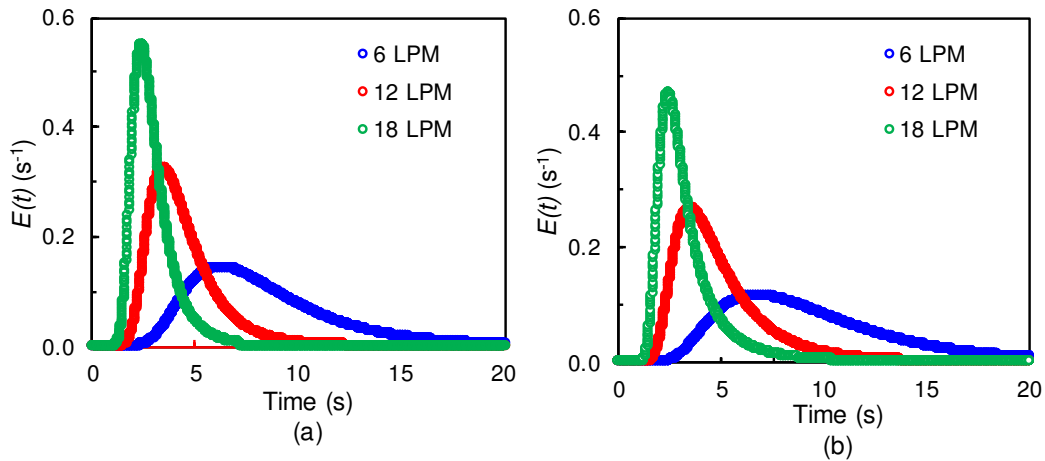
Figure 4.13. Residence time distributions for the shell-side tracer simulations using different flow rates and (a) a non-permeating tracer ($K = 0$) and (b) a permeating N_2 tracer ($K = K_{N2}$).

As expected, the permeating tracer has a lower peak concentration than the inert tracer due to permeation. The RTD curves for the N_2 tracer are also slightly more spread. The increased spreading is likely due to N_2 permeation to the tube-side of the membrane at one location/time, and then back-permeation at a different location/time. To visually explore this effect, the tracer mass fraction for the $6 \, L \, min^{-1}$ case is shown at different time intervals in Figure 4.14 for the non-permeating tracer and in Figure 4.15 for the permeating (N_2)

tracer. The time intervals and color scales are the same for both figures to allow a direct comparison.
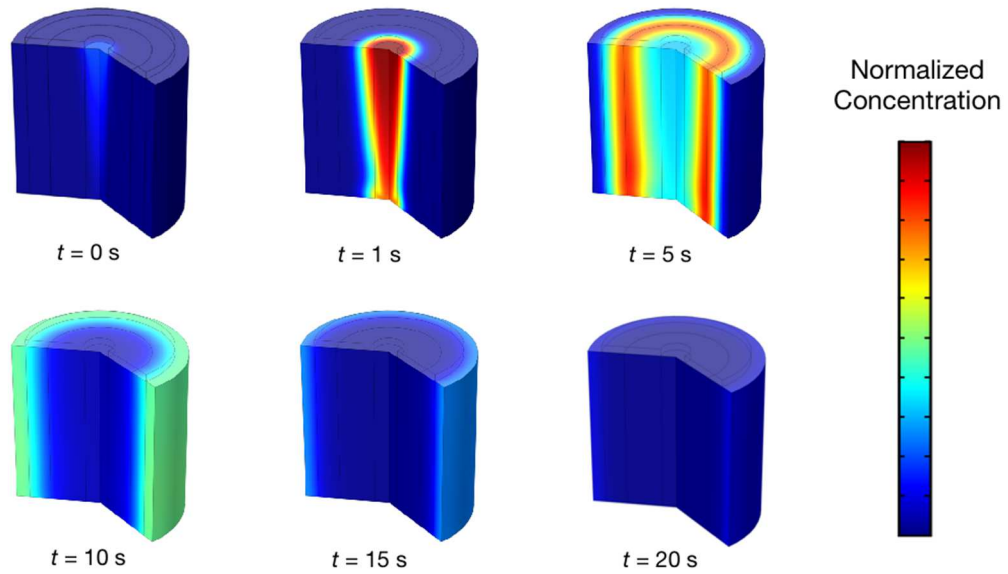
Figure 4.14. Shell-side tracer evolution of a non-permeating tracer at times of 0 s (top left), 1 s (top middle), 5 s (top right), 10 s (bottom left), 15 s (bottom middle) and 20 s (bottom right) after injection into an O_2 stream flowing at 6 L min^{-1}.
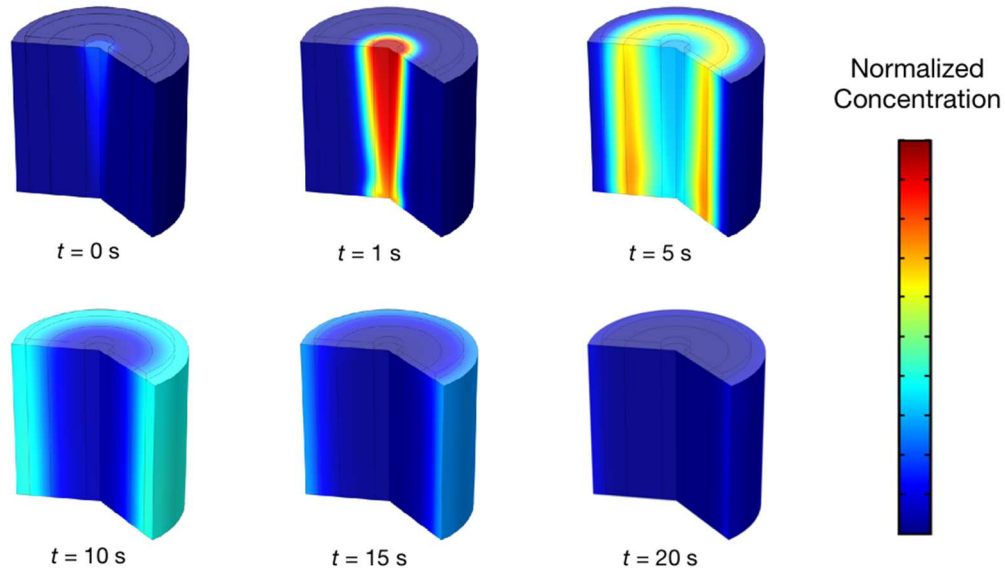
Figure 4.15. Shell-side tracer evolution of a permeating (N_2) tracer at times of 0 s (top left), 1 s (top middle), 5 s (top right), 10 s (bottom left), 15 s (bottom middle) and 20 s (bottom right) after injection into an O_2 stream flowing at 6 L min^{-1}.

The concentration of the permeating tracer is noticibly lower at the 5 and 10 second intervals (Figure 4.15) than they are for the non-permeating tracer at the same times (Figure 4.14). Additionally, although it is somewhat more difficult to see on the figures, the concentration of the permeating tracer is higher at the 15 and 20 second intervals (Figure 4.15) than it is for the non-permeating tracer at the same times (Figure 4.14). This reduction and subsequent increase in concentration can only be due to permeation followed by back-permeation. The spreading of the RTD for the shell-side tracer is limited due to the relatively small volume on the tube side. Spreading would increase if this volume were increased.

4.4.4.2   Tube-side Tracer Simulations

For tube-side tracer simulations, a constant flow rate and a time-dependent input concentration pulse was applied to the tube side of the membrane, while the shell side was effectively closed. The RTD curves for the non-permeating ($K = 0$) and N_2 tracer for the tube-side are shown in Figure 4.16 for three flow rates.
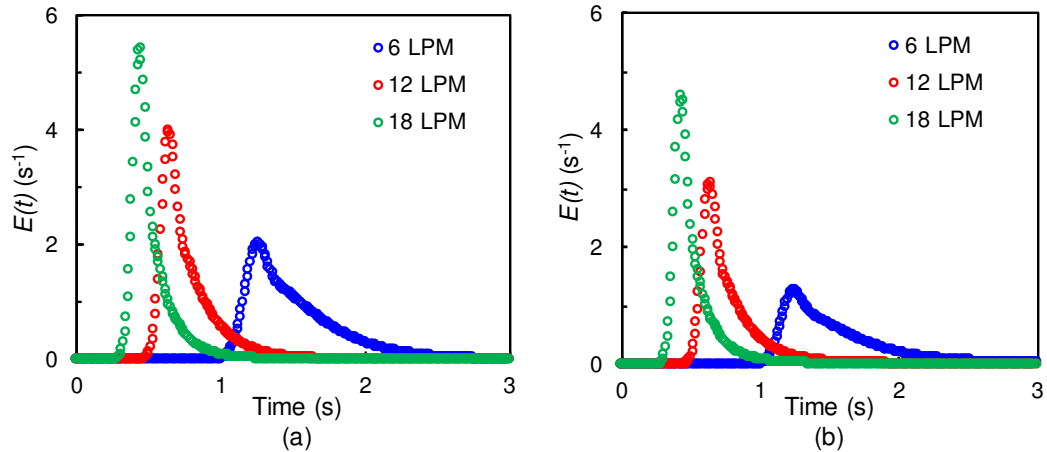
Figure 4.16. Residence time distributions for the tube-side tracer simulations using different flow rates and (a) a non-permeating tracer ($K = 0$) and (b) a permeating N_2 tracer ($K = K_{N2}$).

The responses for the permeating and non-permeating tracer are quite different. The disparity between the two tracers seems to be more dramatic than for the shell-side studies. The permeating tracer peak for each flow rate is lower than for the corresponding flow rate for the non-permeating case. The length of the tail in the RTD is also more significant in the permeating cases, and it takes longer for the concentration to return to zero. As for the shell side, the differences in the RTD are likely due to N_2 permeation to the shell side, followed by subsequent back-permeation. The tube-side concentration fields at different time intervals are shown for the non-permeating and permeating case in Figure 4.17 and Figure 4.18.
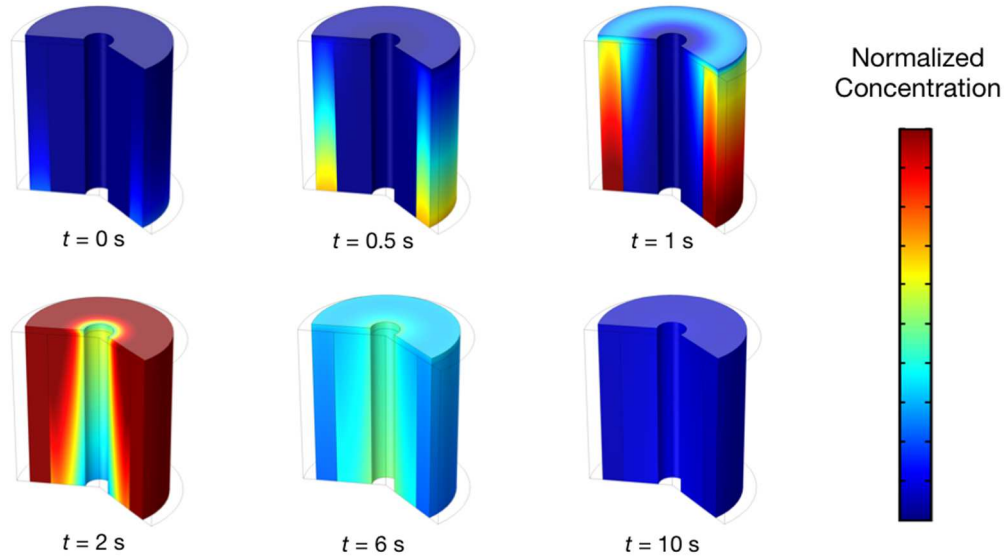
Figure 4.17. Tube-side tracer evolution of a non-permeating tracer at times of 0 s (top left), 0.5 s (top middle), 1 s (top right), 2 s (bottom left), 6 s (bottom middle) and 10 s (bottom right) after injection into an O_2 stream flowing at 6 L min^{-1}.
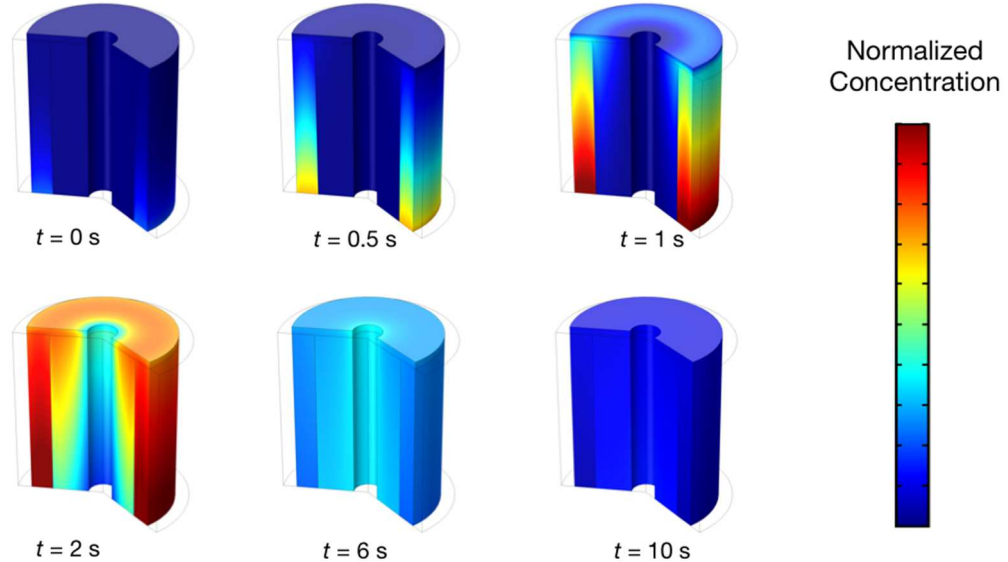
Figure 4.18. Tube-side tracer evolution of a permeating (N_2) tracer at times of 0 s (top left), 0.5 s (top middle), 1 s (top right), 2 s (bottom left), 6 s (bottom middle) and 10 s (bottom right) after injection into an O_2 stream flowing at 6 L min^{-1}.

The concentration of the permeating tracer is clearly lower throughout the tube-side of the module than the non-permeating tracer for times up to 6 s (Figure 4.17 and Figure 4.18).

64

However, at 10 s it is apparent that the concentration of the permeating tracer (Figure 4.18) is still more distributed through the module than for the non-permeating tracer (Figure 4.17). This is the direct result of back-permeation from the shell side. The shell-side concentration during the permeating tube-side tracer simulation (in Figure 4.18) is shown in Figure 4.19.
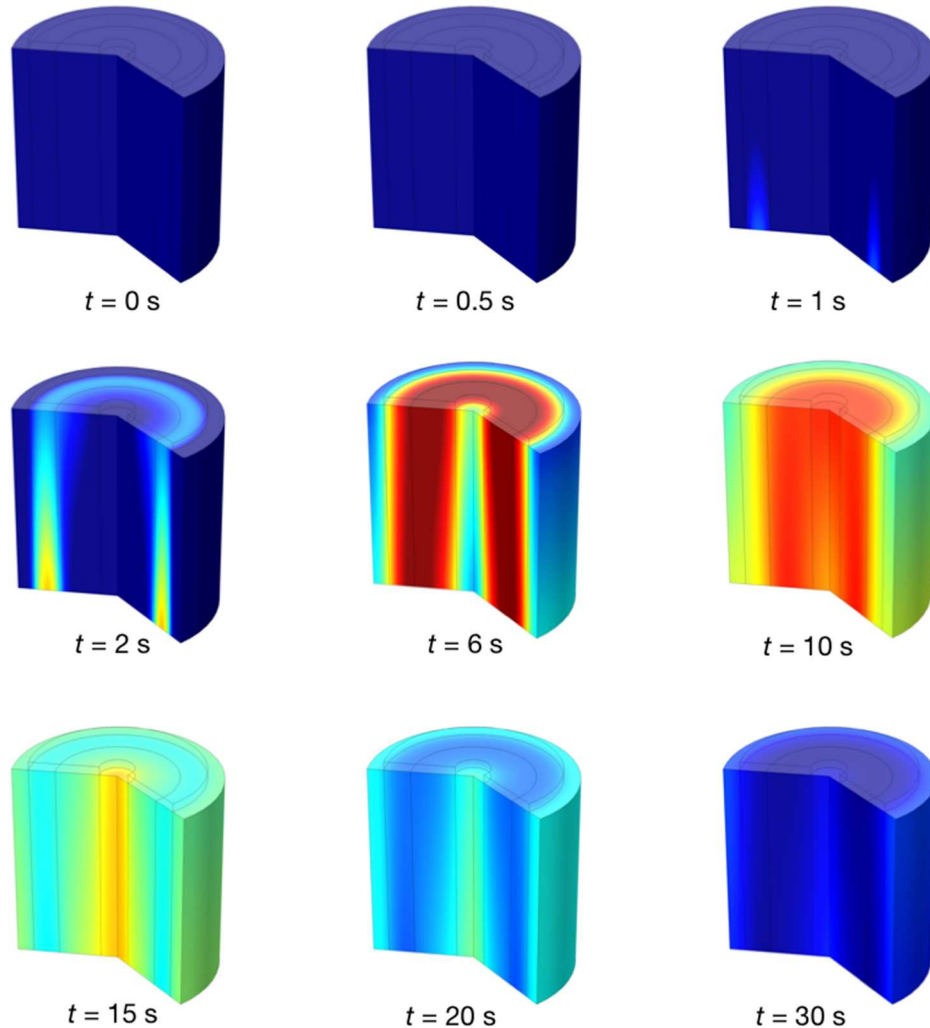
Figure 4.19. Shell-side concentration during the tube-side permeating tracer evolution at times of 0 s (top left), 0.5 s (top middle), 1 s (top right), 2 s (center left), 6 s (center middle), 10 s (center right), 15 s (bottom left), 20 s (bottom middle) and 30 s (bottom right) after injection into an O_2 stream flowing at 6 L min^{-1} on the tube-side.

The change in concentration on the shell side confirms that the tracer permeated to the shell side and then slowly permeated back to the tube side. It also indicates that at the later time steps, the concentration is higher in the membrane free zones of the core and housing than

it is in the fiber bundle. These concentrations at the later time steps correspond with the long tail of the permeating tracer response curve compared to the non-permeating case.

Qualitative analysis of the residence time distribution curves and visualization of the concentration fields provides useful insight into the phenomena occurring in the system. However, it is also useful to directly compare the calculated parameters of the output curves. Table 4.4 contains a summary of the calculated hydraulic parameters for the permeating and non-permeating tracer simulations.

Table 4.4. Summary of residence time distribution for a non-permeating and permeating tracer for the shell and tube side

Flow rate	Shell-side				Tube-side			
L min^{-1}	τ (s)	t_m (s)	σ_θ^2	N	τ (s)	t_m (s)	σ_θ^2	N
Non-permeating								
6	9.27	8.32	0.19	5.40	1.46	1.53	0.05	20.08
12	4.64	4.36	0.15	6.85	0.73	0.78	0.07	14.35
18	3.09	2.88	0.11	9.13	0.49	0.53	0.08	11.80
Permeating								
6	9.27	9.49	0.21	4.70	1.46	3.97	1.21	0.83
12	4.64	4.94	0.21	4.76	0.73	2.17	2.65	0.38
18	3.09	3.36	0.23	4.40	0.49	1.50	4.09	0.24

The values listed in Table 4.4 largely confirms the visual observations made above. The shell-side tracer results show smaller differences between permeating and non-permeating tracer simulations. This is due to the comparatively small volume of the tube side compared to the shell side. Conversely, the tube-side parameters are significantly different for the permeating and non-permeating tracer cases. Again, this is due to the large volume of the shell side, and due to the relatively large size of the membrane free zones (which can retain permeated tracer for a prolonged period of time).

Residence time distribution studies can be quite useful for providing data for modeling approaches that capture non-ideal hydrodynamic behaviour in flow reactors. These types

of experiments are also useful for studying the effect of different operating parameters on fluid flow and identifying limitations of model applicability. The non-permeating simulations meet the criteria for RTD studies (non-reactive tracer, comparable properties of bulk system) so computing and interpreting model parameters with this data is reasonable, while keeping in mind that characterizing the CFD model flow patterns is not that useful unless it is confirmed with experimental data (Chapter 5). In general, the computed numbers of tanks in series (N) in Table 4.4 compare relatively well with the fitted values from Chapter 3.

4.4.5 General Discussion

The tracer studies with a permeating and non-permeating tracer show that it is not appropriate to assume that a component with a low permeance behaves the same as an inert tracer. This is especially true when the tracer can permeate into a relatively large volume. This makes it challenging to compare experimental tracer results in the present gas membrane system to the simple residence time distribution models that assume an inert tracer. Instead, experimental results from studies with permeating tracers should be compared directly to detailed models, which can perform tracer studies with a permeating component.

The typical tanks-in-series approach is complicated by the coupling effect of permeation across the membrane. For an ideal tanks-in-series approach, the output RTD signal is used to tune the number of tanks in series based on the assumption that the response curve is exclusively from hydrodynamics. In the membrane system, tracer permeation effects may also contribute to the output response. Since both the number of segments and the membrane permeance impact the membrane performance, an expanded set of validation experiments should be performed, which depend on both the flow patterns and membrane mass transfer.

4.5 Conclusions

In inhalation anesthesia, CO_2 removal is critical to allow the reuse of the anesthetic vapours in the breathing circuit. Conventional soda lime absorbers have been linked to negative health effects, and therefore a new membrane-based system has been developed to enable

CO_2 removal. This membrane system is currently configured as a two-pass cross-flow hollow fiber membrane contactor, and uses a sweep gas to drive the transfer of CO_2 across the membrane. In this study, a detailed CFD model was developed to analyze the performance of the membrane module. Steady-state experimental data were used to tune membrane permeance values for the membrane. Model predictions were then compared to the full set of steady-state experimental data. A series of steady-state simulations was performed and visualizations were generated to analyze the separation performance and flow behaviour in the system. A series of tracer simulations was also used to investigate mixing behaviour in the module.

The results showed that the CFD model could provide good predictions of steady-state separation performance, even though the only tuning parameters for the model were the membrane permeance values. Visualization of the steady-state two-dimensional velocity and concentration fields showed that flow distribution remained very uniform on both the shell and tube sides of the membrane. The results also seem to indicate that flow maldistribution could become a problem for significantly higher shell-side flow rates and/or a significantly decreased hollow fiber packing density. Analysis of the tracer simulations revealed that such studies would be quite sensitive to tracer permeation through the membrane. Since it is difficult to find a real tracer to which the membrane is truly impermeable, analysis of experimental tracer studies would therefore not be trivial. The recommendation is therefore to use a real tracer (having a finite permeability) and to analyze the results by comparison to a sufficiently detailed model.

4.6 Nomenclature

Symbols

a	membrane surface area per unit of volume in the membrane bundle (m^{-1})
A_M	membrane area (m^2)
C	tracer concentration leaving the system at time t
d	core diameter (m)
D	diffusion coefficient $(m^2\ s^{-1})$
$E(t)$	residence time distribution (s^{-1})

F	volume force (N m^{-3}).
j	mass averaged flux (kg m^{-2} s^{-1})
K	membrane permeances (mol m^{-2} h^{-1} bar^{-1})
M	molar mass (g mol^{-1})
N	tanks-in-series model parameter
N_i	molar flow rate of component i across the membrane (mol s^{-1})
P	pressure (bar)
r_1	inner radius of the outlet specific area
r_2	outer radius of the outlet specific area
Re	Reynolds number
RTD	residence time distribution
S_i	mass source of species i (kg m^{-2} s^{-1})
$S_{total,k}$	total mass source term due to membrane permeation (kg m^{-3} s^{-1})
T	temperature (K)
t	time after the pulse injection (s)
t_m	mean residence time (s)
u	average velocity (m s^{-1})
V	flow volume (m^3)
$\dot{V}$	volumetric flow rate (m^3 s^{-1})
w	local mass fraction
y	molar fractions

Greek letters

ε	porosity
θ	dimensionless time
κ	permeability of the porous medium (m^2)
μ	viscosity (kg m^{-1} s^{-1})
ρ	density (kg m^{-3})
σ^2	variance (s^2)
τ	space-time (s)

Subscripts

k	shell or tube side of the membrane
i	species i

P	permeate
R	retentate

Chapter 5:   Dynamic Membrane Model Validation using Experimental Tracer Studies

5.1 Introduction

Membrane technology has emerged as a promising alternative to conventional gas separation processes for a wide range of applications. Hollow fiber membrane contactors offer several advantages over other technologies, including high mass transfer to surface area to volume ratio, operational flexibility, and ease of modular scale-up [19]. These contactors consist of many membrane fibers (small diameter polymeric tubes) arranged in a module to give optimal contacting with the fluid phases on either side of the barrier. In most contactor arrangements, a feed fluid (gas or liquid) is introduced into one side of the module (either to the shell-side or to the tube-side), while a contacting fluid (gas or liquid) is introduced to the opposite side. Most systems involve the contacting of a gas phase with a liquid phase on the other side (*e.g.*, absorption, stripping, evaporation, *etc.*), or the contacting of two liquid phases to facilitate transfer of one or more solutes between them (*e.g.*, dialysis, liquid extraction, *etc.*). The membranes used in such systems may be porous, providing a non-selective or selective physical barrier between the phases. Alternatively, the membranes may be effectively non-porous (or dense), providing a selective physical barrier between the phases.

The specific system considered in this thesis is intended to be used for the removal of CO_2 from anesthesia circuits using a dense CO_2-selective hollow fiber membrane module. Since anesthetic compounds are not metabolized during anesthesia, they may be re-administered to the patient if excess CO_2 is removed from the exhaled gas stream. The CO_2 concentration must be reduced from approximately 5 mol% to at most 0.5 mol% before the gas stream is reused. In the current system, the gas exhaled by the patient (having concentration of 5 mol% CO_2) is introduced to the shell-side of the membrane module. Pure O_2 is introduced as a sweep gas on the tube-side to increase the partial pressure driving force and thereby facilitate transport of CO_2 across the membrane. High and/or vacuum pressures are not used to enhance transfer rates for safety reasons.

A relatively simple dynamic design model was developed for the membrane module in Chapter 3 using a series of interconnected perfectly-mixed control volumes (*i.e.*, tanks-in-series approach). The number of control volumes (or segments) used to represent the membrane module was tuned to match steady-state experimental data. Additionally, a computational fluid dynamics (CFD) model was developed in Chapter 4, and this model was used to tune the membrane permeance and to visualize the velocity and concentration fields in the system. Although both models provided good predictions of the steady-state experimental data, anesthesia circuits have inherently dynamic flows and concentration changes. It is therefore important to validate both models under dynamic conditions through comparison with appropriate experimental results.

The separation performance of hollow fiber membrane modules is governed, in part, by the flow patterns and mixing regimes within the module, so it is important for the model to reflect these parameters appropriately. While flow inside the fibers has been generally well described using appropriate mass transfer analogies, shell-side mass transfer has been more challenging to model due to unknown mixing behavior and the possibility of flow maldistribution [27]. Mixing behaviour and hydrodynamics in reactors are commonly characterized by analyzing residence time distributions (RTD) following the injection of an inert tracer. The validity of residence time distribution analysis relies on an inert tracer. This ensures that the response observed may be attributed only to the hydrodynamics in a system, as opposed to other effects (*e.g.* reaction). It is often challenging to perform RTD studies in membrane systems because many tracers that are sufficiently similar to the fluids of interest permeate across the membrane, changing the shape of the output curve and its interpretation. Of course, it is possible to prevent permeation during an RTD study by, for example, sealing the membrane or filling the other side of membrane with a fluid that blocks permeation [46]. However, such techniques will often prevent the use of the module in further studies. The CFD model was previously used to compare RTD responses for an ideal non-permeating tracer and a real tracer with a relatively low permeance (Chapter 4). The results of this study showed that the RTD output is significantly altered by membrane permeation, even when the tracer has a relatively low permeance. For this reason, it is difficult to perform an experimental RTD study and then compare the results to simple models meant for inert tracers.

The main objective of this study is to validate and analyze dynamic predictions made by the previously developed design and CFD models. It is particularly important to confirm the validity of the design model because the goal is ultimately to couple this model to a full model of an anesthesia circuit. Predictions from the CFD model are important for comparison and cross-validation, but the computational cost of such a model is currently still too high to permit direct incorporation into a full circuit simulation. Since the models can make RTD predictions for permeating or non-permeating tracers, RTD experiments were only performed with gases of interest in the current application, all of which can permeate through the membrane. This permits comparison between experimental data and model predictions, but the main disadvantage is that the experimental data cannot be analyzed directly using typical simplified models for inert tracers.

5.2 Experimental

5.2.1 Materials

The assembled polymethylpentene (PMP) membrane bundle was supplied by 3M, Membranes Business Unit in Wuppertal, Germany (3M). In the bundle, hollow fibers are woven into a mat and wrapped around a cylindrical perforated hollow core. The fibers are potted in a disk-shaped glue line on either end to separate the shell and tube flows. The membrane bundle was implanted into a custom manufactured housing that provided sealing and connections with the inlet and outlet ports. As previously described (Chapter 3), the module has been used in single- and double-pass configurations for the sweep gas. In this study, only the double-pass configuration was used. A diagram of the module in the double-pass flow arrangement is shown in Figure 5.1. The shell-side fluid enters the fiber bundle through the inner core and flows radially outward across the membrane bundle. A sweep gas is administered through the inside of the hollow fibers.
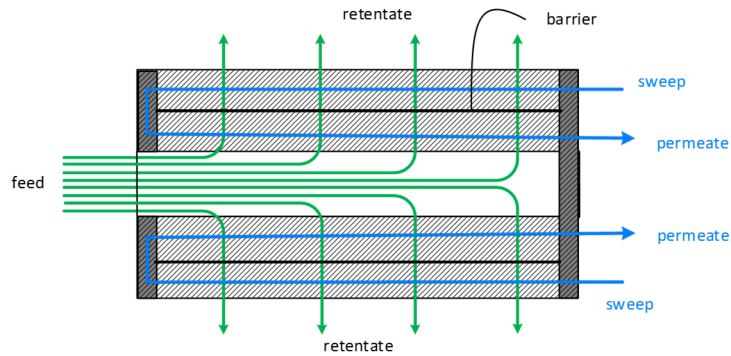
Figure 5.1. Flow diagram of double-pass membrane module.

The module properties are listed in Table 5.1.

Table 5.1. Membrane module geometrical properties

Parameter	Value
Active membrane area (m^2)	2.1
Packing density	0.45
Fiber inner diameter (μm)	200
Fiber outer diameter (μm)	380
Number of fibers	29500
Active membrane length (mm)	120
Core diameter (mm)	20
O-ring average diameter (mm)	70
Bundle diameter (mm)	100

5.2.2 Methods

All tracer experiments were performed using O_2 (USP grade, 99.99% pure, DIN: 02014408, Praxair, Mississauga, ON, CA) and N_2 (Air Liquide, Dartmouth, NS, CA). The membrane permeances of O_2 and N_2 are known to be approximately 18.0 and 4.5 mol m^{-2} h^{-1} bar^{-1} from previous fitting with experimental data [26]. During the experiments, gas concentrations were measured using a quadrupole mass spectrometer (Omnistar Model PTM81217131, Pfeiffer Vacuum, Aßlar, Germany) with a minimum detection limit of 1 ppm. Pfeiffer Vacuum's Quadera software (v4.50.004) was used to control the mass spectrometer. Two sets of tracer experiments were performed, with each set involving both

shell-side and tube-side experiments. In the first set, the tracer was supplied to one side of the membrane and the other side was blocked, thereby minimizing permeation. In the second set, the tracer was supplied to one side of the membrane and sweep gas was supplied to the other side, which encourages permeation. Gas flow rates were chosen to be within the range of interest in anesthesia circuits.

5.2.2.1 Single-side Nitrogen Tracer

The configurations used for the first set of tracer experiments are shown in Figure 5.2. In the first tracer experiments, pure O_2 was supplied to the shell side of the membrane module, while the tube-side ports were plugged (Figure 5.2a). In the second tracer experiments, pure O_2 was supplied to the tube side of the membrane module, while the shell-side ports were plugged (Figure 5.2b). The injection syringe, containing 5 mL of pure N_2, was connected to the inlet flow line with a three-way valve. The tracer was injected as close to the module as possible and the tubing between the module and mass spectrometer sampling point was minimized and held constant for all experiments. The O_2 flow rate was controlled using a Scott Specialty Gases glass tube flow meter ($\pm$ 5% of full scale, 15.61 L min^{-1}) and was measured using an Aalborg XFM digital mass flow meter ($\pm$ 5% of full scale, 20 L min^{-1}). Once the O_2 flow rate was set, the tracer was injected by the syringe and the time of injection was recorded. The outlet concentration was measured continuously using the mass spectrometer and, once the system returned to steady-state, the time and concentration data were exported to a spreadsheet for post-processing. The procedure was then repeated for the next flow rate. The flow rates used in this study were 3, 6, 12 and 18 L min^{-1}. Nitrogen was selected as the tracer gas for this set of experiments because it has the lowest permeance in the membrane of the available tracer gases based on the characterization study [26].
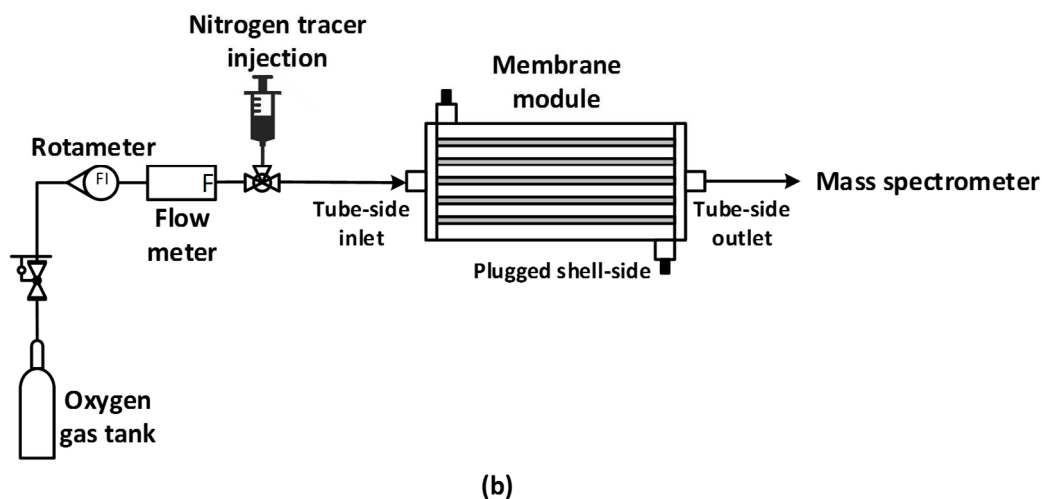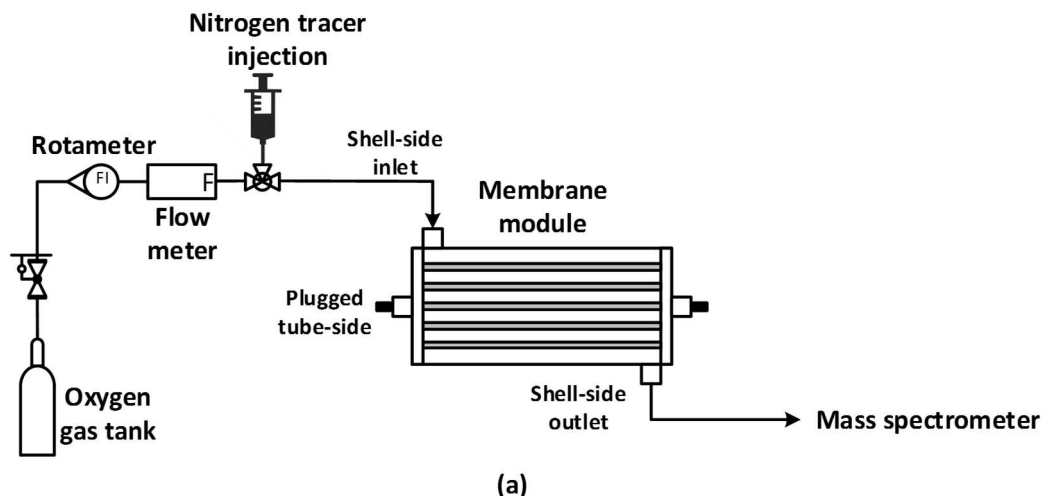
Figure 5.2. Schematic of the experimental configurations for single-side tracer experiments for the (a) shell-side and (b) tube-side of the membrane module.

5.2.2.2 *Oxygen Tracer with Nitrogen Sweep Gas*

The configurations used for the second set of tracer experiments are shown in Figure 5.3. In the first tracer experiments, pure N_2 was supplied to both the shell and tube side of the membrane, and the pure O_2 tracer was injected into the shell-side feed (Figure 5.3a). In the second tracer experiments, pure N_2 was supplied to both the shell and tube side of the membrane, and the pure O_2 tracer was injected into the tube-side feed (Figure 5.3b). The sweep gas flow rate was 6 L min^{-1} for all cases and the tracer-side flow rates used were 6, 12 and 18 L min^{-1}. The N_2 flow rates were controlled using a Scott Specialty Gases glass tube flow meter ($\pm$ 5% of full scale, 15.61 L min^{-1}) and measured using an Aalborg XFM

digital mass flow meter (± 5% of full scale, 20 L min^{-1}). The combination of flow rates for all experiments is summarized in Table 5.2.

As for the previous set of experiments, a 5 mL syringe was used to inject the pure O_2 tracer into the N_2 feed stream. Since only one mass spectrometer was available to measure the outlet concentration, it was necessary to perform an experiment at one set of conditions and measure the evolution of the tracer concentration on only the tracer side of the membrane. The experiment was then repeated at the same conditions to measure the evolution of the tracer concentration on only the sweep side of the membrane. The outlet concentration was measured continuously and once the system returned to steady-state, the time and concentration data were exported.

Table 5.2. Nitrogen flow rates for O_2 tracer experiments with nitrogen sweep

	Shell flow rate (L min^{-1})	Tube flow rate (L min^{-1})
Shell-side tracer	6	6
Shell-side tracer	12	6
Shell-side tracer	18	6
Tube-side tracer	6	6
Tube-side tracer	6	12
Tube-side tracer	6	18
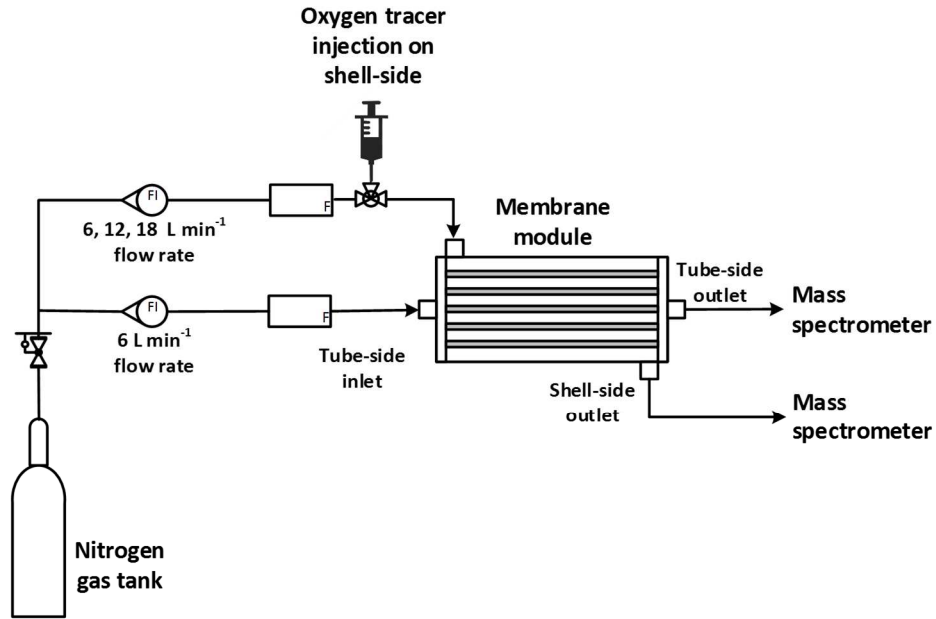
(a)
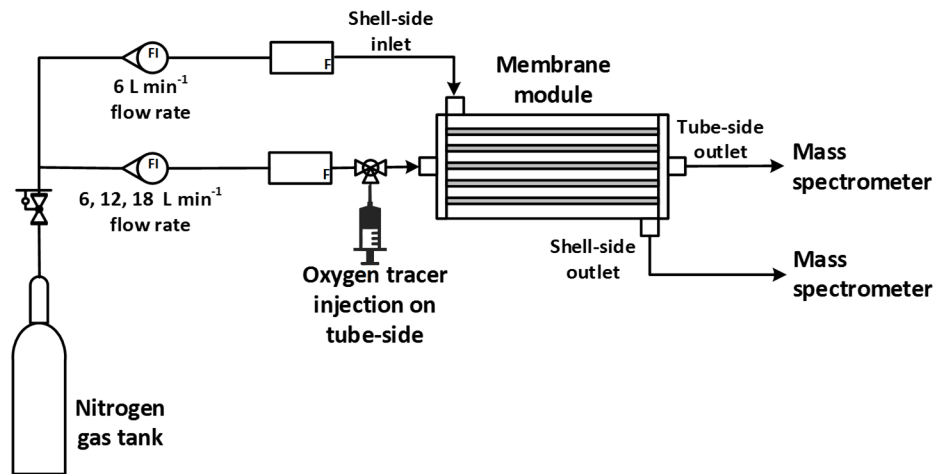
(b)

Figure 5.3. Schematic of the experimental configurations used for O_2 tracer experiments with a N_2 sweep gas for (a) shell-side and (b) tube-side tracer injection.

5.3 Model Description

5.3.1 Tracer Input Signal

To accurately compare predictions made by the design and CFD models with the data from the tracer experiments, it is necessary to ensure that the time-dependent concentration input curves used in the models match the experimental curves. Since a perfect pulse input is

difficult to obtain in practice, the system response curve may be misinterpreted if the input signal deviates from the assumed ideal signal. To prevent modeling errors resulting from an incorrect input signal, the signal was determined by injecting the tracer directly into the system without the membrane module. The measured concentration data were then exported. The input signal was obtained for the four flow rates used in the tracer studies (3, 6, 12 and 18 L min^{-1}). The input curve was normalized by the peak concentration for the four flow rates. An example of the input signal for the 18 L min^{-1} flow rate is shown in Figure 5.4.
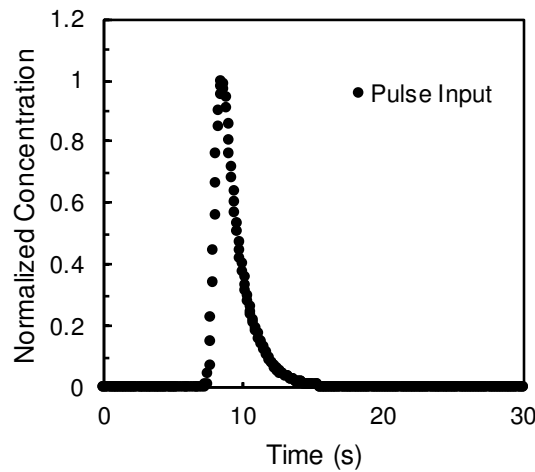
Figure 5.4. Example of tracer injection signal for a flow rate of 18 L min^{-1}.

The design model was implemented using MATLAB and Simulink [36]. Therefore, the input signals for the design model were generated from the measured data using MATLAB's spline interpolation. The CFD model was implemented using COMSOL Multiphysics 5.2 [40]. For the CFD model, the experimental input curves were imported into COMSOL and its interpolation function was used to develop a time-dependent inlet concentration boundary condition.

For the single-side cases, the tracer response was obtained for both the shell and tube sides of the membrane by setting the flow rate of the opposing side of the membrane to zero. The time-dependent outlet concentration profiles were then normalized. For the permeating cases, the flow rate on each side was set and the outlet permeate and retentate concentration profiles were exported.

5.3.2 CFD Model

Computational fluid dynamics (CFD) simulations provide a means for detailed analysis of local transport phenomena in a variety of systems. The CFD model, which was implemented in COMSOL Multiphysics 5.2, was described in detail in Chapter 4. The membrane system was modeled by solving separate momentum, continuity and species equations for the shell and tube sides of the module. The equations were then coupled by incorporating appropriate local volumetric total mass and species mass source terms into the equations to represent mass transfer across the membrane. Flow through both the shell and tube sides of the membrane bundle were approximated by applying a porous media flow model. In these porous zones, the flow was modeled using the Brinkman equation. The permeability of the porous media, which directly controls resistance to flow through the media, was adjusted to match the properties of the woven hollow fiber mat on the shell-side and the inner diameter of the hollow fibers on the tube side. Flow in the membrane-free zones of the module (inner core, outer housing gap and tube mixing zone) was modeled using the Navier-Stokes equations. The membrane module was represented using a two-dimensional, axisymmetric computational domain. The main difference between the CFD simulations performed in this study and the simulations performed in Chapter 4 is the use of the special time-dependent input concentration (described above) for the tracers. An overview of the geometry and settings used for these simulations is provided in Figure 5.5.
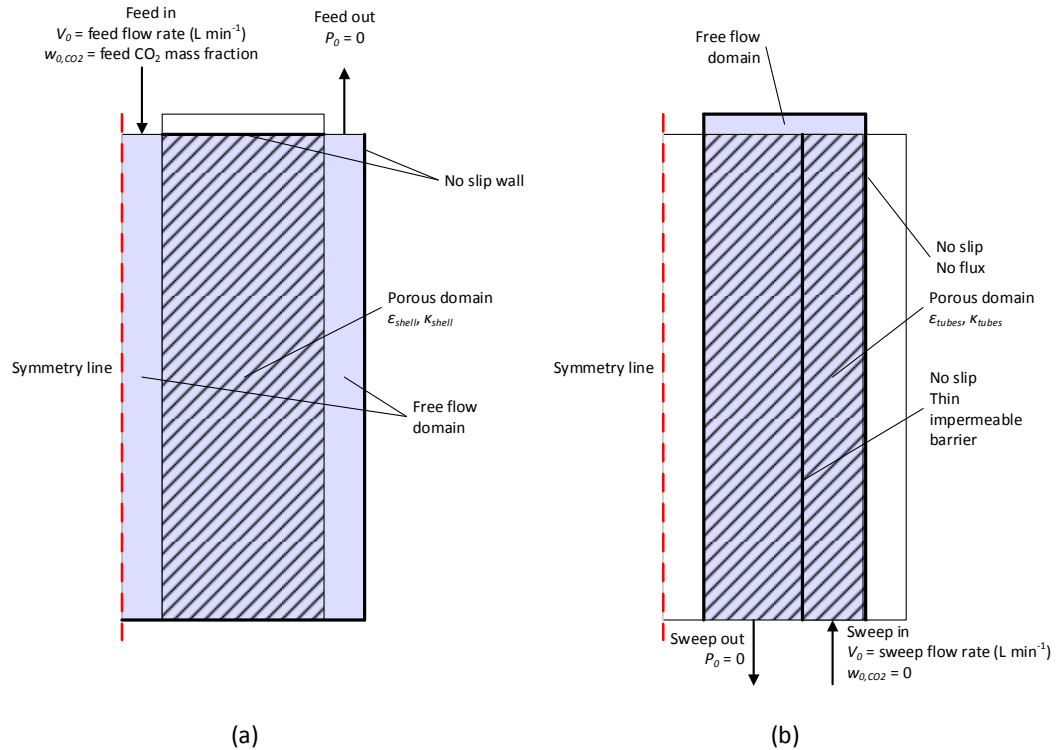
Figure 5.5. Overview of the geometry and conditions in the COMSOL model for the (a) shell-side and (b) tube-side domain.

5.3.3 Design Model

5.3.3.1 Model Summary

A design model was derived for the membrane system in Chapter 3 and predictions were validated using steady-state experimental data. The model was formulated by dividing the membrane module into a system of interconnected perfectly-mixed control volumes (or segments). Dynamic material balance equations were then written for each segment. The shell and tube-side material balances were coupled using a transmembrane species permeation rate equation based on the solution-diffusion model. Coupling between segments was achieved by transferring outlet conditions from one segment as the feed conditions to a subsequent segment. Practically, this methodology is very similar to the tanks-in-series approach, which is very commonly used in reactor modeling. The model equations are summarized in Table 5.3 with respect to component i.

81

Table 5.3. Summary of segment model equations

Transmembrane flow rate

$$N_i = K_i A_M (y_{i,R} P_R - y_{i,P} P_P)$$

Retentate and permeate flow rates

$$F_R = F_F - \sum N_i$$

$$F_P = F_S + \sum N_i$$

Retentate and permeate concentrations

$$\frac{dy_{i,R}}{dt} = \frac{y_{i,F} F_F - y_{i,R} F_R - N_i}{n_R}$$

$$\frac{\partial y_{i,P}}{\partial t} = \frac{y_{i,S} F_S - y_{i,P} F_P + N_i}{n_P}$$

In the segmental model, N_i is the molar flow rate of component i across the membrane of the segment (mol s^{-1}), K_i is the membrane permeance (mol m^{-2} s^{-1} bar^{-1}), A_M is the segment membrane area (m^2), $y_{i,R}$ and $y_{i,P}$ are the molar fractions of component i on the retentate and permeate side of the membrane, P_R and P_P are the bulk pressures (bar) of the retentate and permeate side, and F_F, F_S, F_R and F_P are the molar flow rates of the feed, sweep, retentate and permeate (mol s^{-1}).

The number of discrete segments was determined by setting the membrane permeance and tuning the segments to match the steady-state experimental data. The final number of segments that was determined for the membrane module used in this study was 10 representing the tube side and 6 representing the shell side, as depicted in Figure 5.6.

In the simulations presented in Chapter 3, only steady-state predictions were analyzed and compared to experimental data. Under steady-state conditions, only the membrane surface area and the feed conditions affect the outlet concentrations. The volumes of the segments in the bundle and empty volumes within the module do not affect the steady-state predictions directly. However, under dynamic conditions (*e.g.*, during tracer injection), these volumes change the residence time and therefore the predicted RTD is affected by their size. A major difference between the segmental model used in this study and the one

used in Chapter 3 is that the current model includes the volumes of the membrane-free regions within the module (shown as dark gray blocks in Figure 5.6).
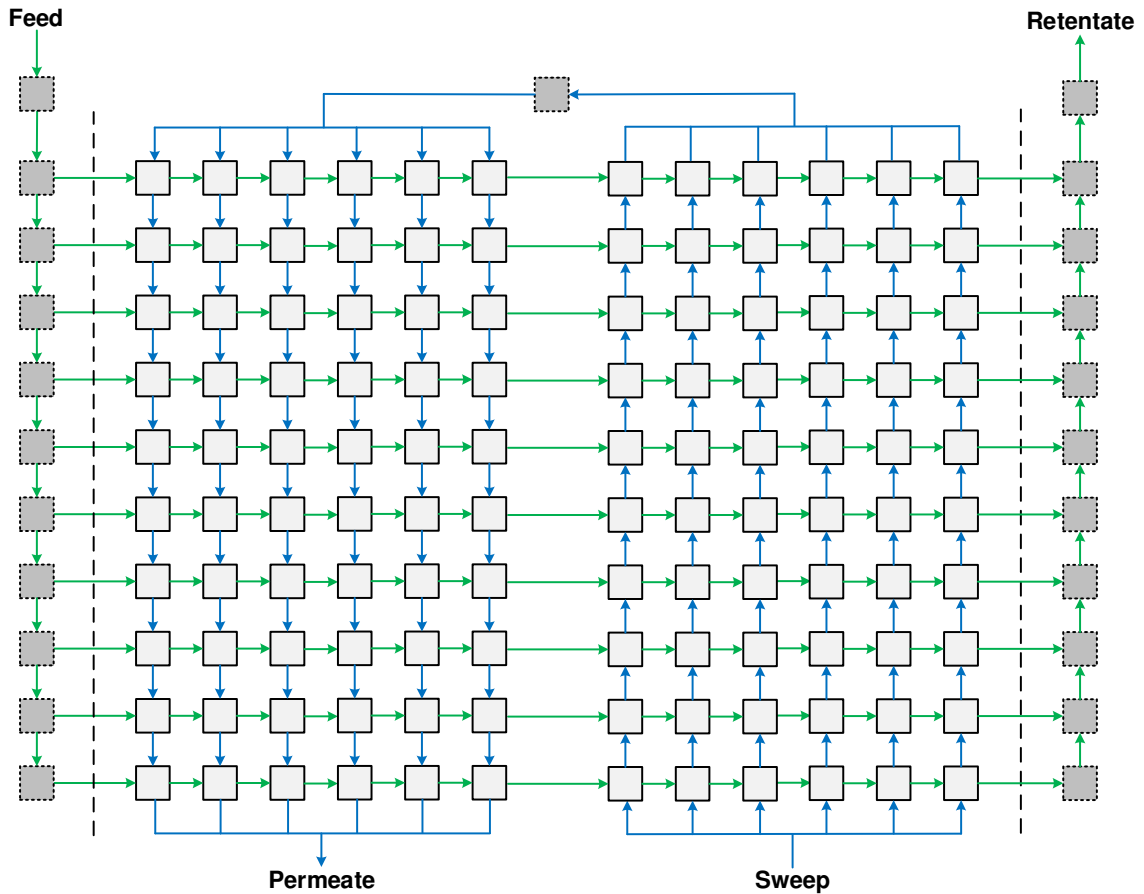
Figure 5.6. Representation of the segmental model discretization scheme used in this study. The light gray blocks represent space containing hollow fibers and the darker gray blocks represent the extra volumes within the housing.

As mentioned above, the tracer studies were simulated by solving the dynamic model equations and specifying the inlet concentration based on the signal interpolated from the experimental pulse input. For the single-sided N_2 tracer cases, the response was obtained separately for both the shell and tube-sides of the membrane by setting the flow rate of the opposing side of the membrane to zero. The membrane permeances for N_2 and O_2 were specified and the initial concentration was assumed to be pure O_2. The time-dependent outlet concentration profiles were then normalized by the peak concentration. For the sweep gas O_2 tracer cases, the N_2 flow rate was set for each side and the O_2 pulse input was specified. The concentration on the shell and tube side were both exported. The output

curves were then normalized by the peak concentration of all the runs for the specific membrane side.

5.3.3.2 Numerical Implementation

The design model equations form a coupled system of differential and algebraic equations (DAEs). In this study, these model equations were solved using a combination of MATLAB and Simulink. A MATLAB script was written to provide data and input conditions for the Simulink model, and to automate its execution. A Simulink block diagram was used to represent the discretization shown in Figure 5.6. Simulink was chosen as a convenient tool to implement this model because the block diagram looks very similar to the representation shown in Figure 5.6 (*i.e.*, similar blocks and connections).

The Simulink block diagram was constructed by making use of built-in blocks for signal routing and manipulation. However, separate custom MATLAB function blocks were written to represent the bundle segments and the membrane-free segments. Copies of these custom blocks were then made, and the resulting blocks were arranged into the configuration shown in Figure 5.6. Once built, the MATLAB script was used to execute the Simulink model, which was solved using the explicit variable step *ode45* solver. The effect of solution tolerances on predicted concentrations was investigated to ensure accuracy of the solution.

5.4 Results and Discussion

5.4.1 Single-side Nitrogen Tracer

Figure 5.7 shows the experimental and simulated shell-side tracer response for flow rates of 3, 6, 12 and 18 L min^{-1}.
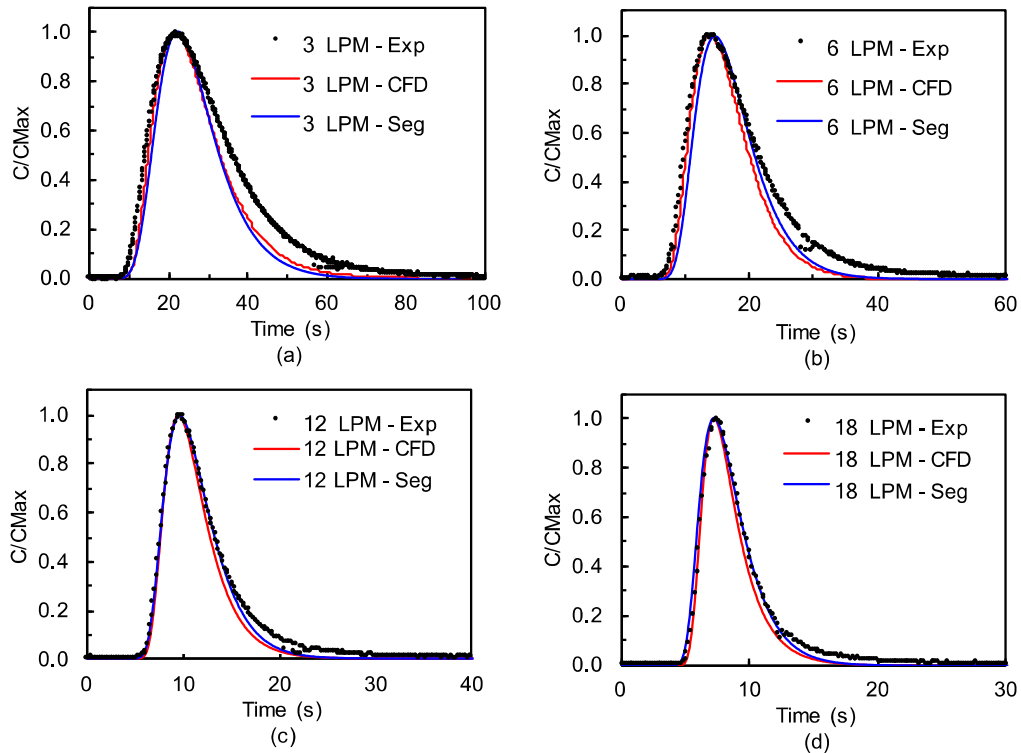
Figure 5.7. Shell-side N_2 tracer response obtained experimentally and simulated with CFD and segmental models. The shell-side flow rates are (a) 3 L min^{-1}, (b) 6 L min^{-1}, (c) 12 L min^{-1}, and (d) 18 L min^{-1}.

The spread of the experimental tracer is higher at lower flow rates compared to the simulated results. Both models under-predict the spread of the tracer at the lower flow rates (3 and 6 L min^{-1}). The model predictions provide a good fit to the experimental data at the two higher flow rates (12 and 18 L min^{-1}). The segmental model predictions are very close to the CFD model predictions for the entire range of flow rates. One reason for this could be that the membrane permeance used in the model was very close to the actual permeances for the membrane. Inaccuracies in the permeance could cause deviations because some of the tracer input on the shell side permeates to the tube side and then returns to the shell side until the concentration gradient has diminished.

Figure 5.8 shows the experimental and predicted tracer response for the tube-side at flow rates of 3, 6, 12 and 18 L min^{-1}.
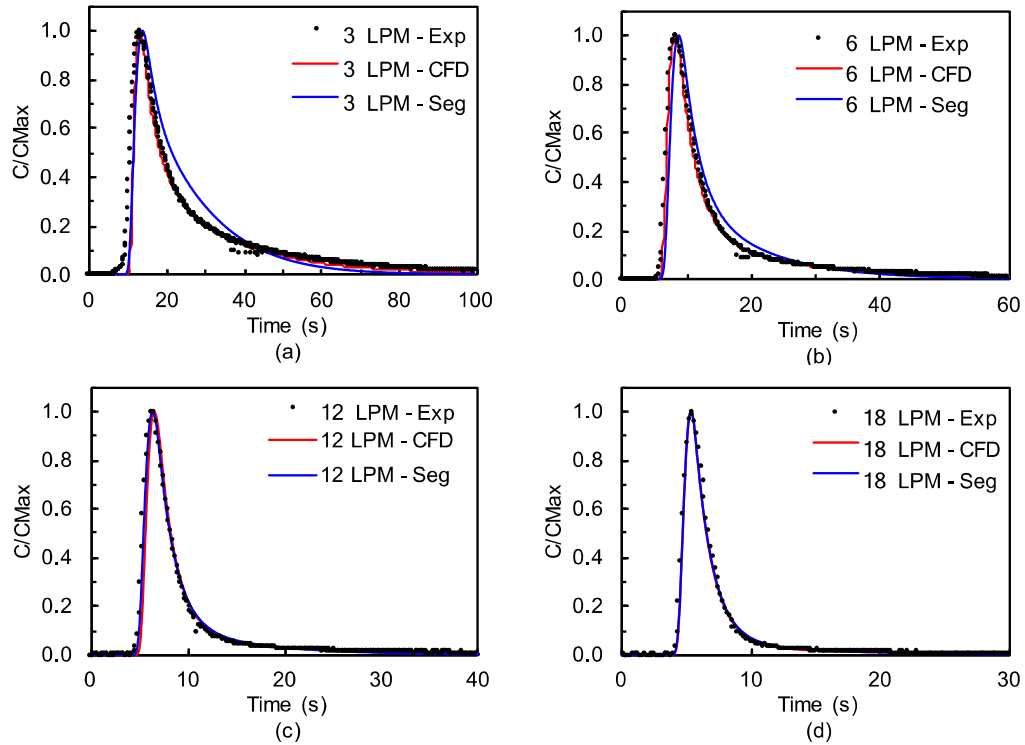
Figure 5.8. Tube-side N_2 tracer response obtained experimentally and simulated with CFD and segmental models. The tube-side flow rates are (a) 3 L min^{-1}, (b) 6 L min^{-1}, (c) 12 L min^{-1}, and (d) 18 L min^{-1}.

Both models provide an excellent fit to the experimental data at the two higher flow rates (12 and 18 L min^{-1}). This good fit is expected because the residence time is very low at these high flow rates and therefore the signal will not deviate very much from the input signal. The CFD model also fits the experimental data very well for the lower flow rates. However, the segmental model over-predicts the spreading of the tracer at 3 L min^{-1} somewhat. This over-prediction is likely due to the representation of the tube-side mixing volume (membrane-free space between the passes) as a single perfectly-mixed volume. Another reason might be that the lower flow rate data would be better represented by a model with more segments in the tube direction, but the purpose of this study was to validate the model for dynamic predictions and not to recalibrate it for different flow rates. Also, the primary benefit of the segmental model is its simplicity and efficiency, and having to recalibrate for different flow rates would defeat its purpose for cases with time-dependent flow rates (*e.g.*, anesthesia circuits). Overall, the segmental model seems to serve its purpose of predicting the RTD relatively well for a range of flow rates without

requiring modification, but its range of applicability is likely somewhat more limited than that of the CFD model.

5.4.2 Sweep-gas Tracer

For the shell-side tracer response with a sweep gas, the O_2 tracer was injected into the N_2 feed flow rate entering the shell side. A 6 L min^{-1} N_2 flow was fed to the tube side. In the following figures, "shell" refers to the response appearing on the shell side while "tubes" refers to the response on the tube side. Figure 5.9 shows the results for the shell-side tracer for N_2 feed flow rates of 6, 12 and 18 L min^{-1}. The red data series are the shell-side responses and the blue data series are the tube-side responses. The first row of graphs shows experimental results, the second row shows the CFD simulations, and the third row shows the segment model predictions.
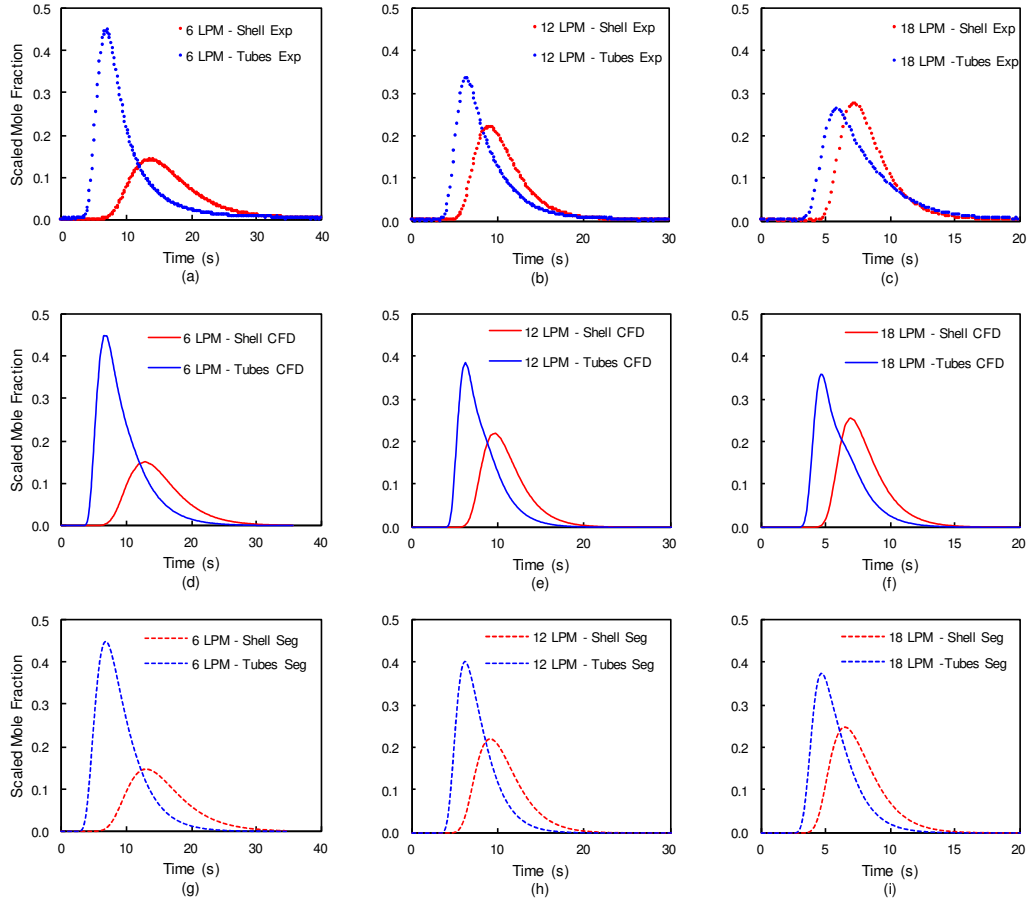
Figure 5.9. Shell-side tracer with 6 L min^{-1} tube-side sweep gas flow: (a) experimental data for 6 L min^{-1} shell flow rate, (b) experimental data for 12 L min^{-1} shell flow rate, (c) experimental data for 18 L min^{-1} shell flow rate, (d) CFD model predictions for 6 L min^{-1} shell flow rate, (e) CFD model predictions for 12 L min^{-1} shell flow rate, (f) CFD model predictions for 18 L min^{-1} shell flow rate, (g) segment model predictions for 6 L min^{-1} shell flow rate, (h) segment model predictions for 12 L min^{-1} shell flow rate, and (i) segment model predictions for 18 L min^{-1} shell flow rate.

The relative peak heights in Figure 5.9 are predicted well by both models at 6 and 12 L min^{-1} feed flow rates. However, at 18 L min^{-1}, the experimental peak tube-side concentration is slightly lower than the shell peak height, while the tube peak is considerably higher than the shell peak height for both simulations. The CFD and segmental models seem to agree with each other for all flow rates.

For the tube-side tracer response with a sweep gas, the O_2 tracer is injected into the N_2 feed entering the tube side. A 6 L min^{-1} N_2 flow is fed to the shell side. Figure 5.10 shows the results for the tube-side tracer for N_2 feed flow rates of 6, 12 and 18 L min^{-1}. The red data

series are the shell-side responses and the blue data series are the tube-side responses. The first row of graphs shows experimental results, the second row shows the CFD simulations, and the third row shows the segment model predictions.
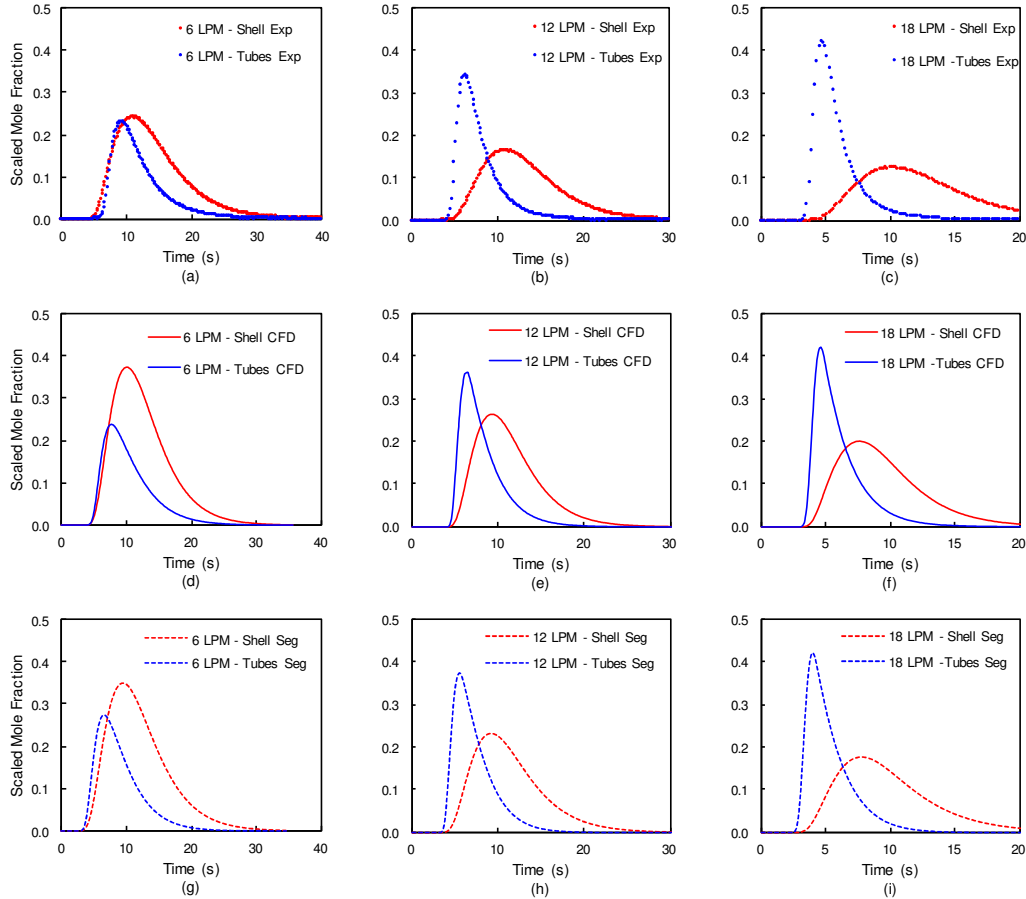
Figure 5.10. Tube-side tracer with 6 L min^{-1} shell-side sweep gas flow: (a) experimental data for 6 L min^{-1} tube flow rate, (b) experimental data for 12 L min^{-1} tube flow rate, (c) experimental data for 18 L min^{-1} tube flow rate, (d) CFD model predictions for 6 L min^{-1} tube flow rate, (e) CFD model predictions for 12 L min^{-1} tube flow rate, (f) CFD model predictions for 18 L min^{-1} tube flow rate, (g) segment model predictions for 6 L min^{-1} tube flow rate, (h) segment model predictions for 12 L min^{-1} tube flow rate, and (i) segment model predictions for 18 L min^{-1} tube flow rate.

The shape of the tube-side response is predicted well by both models when compared to experimental data. However, the shell-side response curves are noticeably more dispersed in the experimental data compared to the simulated results. The predicted shell-side peak height is also higher than the experimental result for all cases. One possible explanation for this could be that the tuned permeance used in the model predictions is higher than the

actual permeance. Decreasing the permeance would mean that less tracer transfers from the tube side to the shell side, translating into a lower shell-side peak height. Since the flow patterns also impact mass transfer, it is challenging to decouple the permeance from the hydrodynamics in this experiment. Considering sources of experimental variabilities and the complexity of the system, the predictions are still quite good.

5.4.3 General Discussion

The comparison between the experimental tracer data and model predictions presented in this study generally yielded consistent results. However, the comparison also highlighted some challenges in performing this type of study. Specifically, unless modifications can be made to the membrane module to prevent permeation or a truly impermeable tracer can be found, it is not possible to perform a simplified analysis of the RTD results. In this case, it is then necessary to compare tracer results directly with more complex models. Another challenge is the generation of consistent tracer inputs. A step change input signal is simpler to generate, but can be more difficult to analyze accurately. On the other hand, it is difficult to generate a sharp and symmetric pulse input, which also makes the results more difficult to analyze. Finally, although it is possible to minimize extra volumes in the system, these cannot be completely eliminated. Therefore, the inclusion of these extra volumes in the model are critical for comparison, but they may only be known within certain tolerances and may also be challenging to represent in the model.

5.5 Conclusions

The purpose of this study was to collect tracer data for a hollow fiber membrane module that is intended to be used for CO_2 removal in anesthesia circuits, and to use this data to validate the dynamic predictions of previously developed mathematical models for the system. In this study, tracer experiments were performed using O_2 and N_2, since these two gases are already present in a typical anesthesia circuit. Unfortunately, the membrane is selectively permeable to both gases, and the membrane module was not modified to prevent permeation their permeation. It was therefore not possible to analyze the results directly using simplified methods for inert tracers. However, it was possible to compare model predictions made with known gas permeances to the experimental data. Two types of tracer

experiments were performed. In the N$_2$ tracer experiments, N$_2$ was injected into a flowing O$_2$ stream entering one side of the membrane, while the other side of the membrane was blocked. In the O$_2$ tracer experiments, O$_2$ was injected into a flowing N$_2$ stream entering one side of the membrane, while a N$_2$ sweep gas was applied to the other side. The results showed consistent predictions between the design and CFD models. The model predictions were also relatively similar to the experimental results for most of the cases. However, the predictions were not perfect, which highlighted the difficulties in both running experimental tracer studies of this type and effectively determining model tuning parameters.

5.6 Nomenclature

Symbols

A_M	membrane area (m^2)
F	molar flow rate (mol s^{-1})
n	number of moles
K	membrane permeance (mol m^{-2} h^{-1} bar^{-1})
N	molar flow rate across the membrane (mol s^{-1})
P	pressure (bar)
t	time (s)
y	molar fraction

Subscripts

i	species i
F	feed
P	permeate
R	retentate
S	sweep

Chapter 6: Dynamic Segmental Membrane Model Validation using a Simulated Anesthesia Circuit

6.1 Introduction

The hollow fiber membrane system under investigation was already described in detail in the previous studies. This membrane system is intended to be used to replace the CO_2 absorber in an anesthesia circuit. The membrane module consists of a woven hollow fiber mat, wrapped around a cylindrical hollow core. The feed gas flows radially outward from the inner core, through the fiber mat, and then out through a gap between the bundle and the housing. The sweep gas is arranged to flow through the tubes in a two-pass counter-current cross-flow configuration. In Chapter 3, a segmental model was derived and validated for steady-state predictions. The number of segments in the model was tuned to match the experimental data. In Chapter 4, a CFD model implemented in COMSOL Multiphysics was used to determine the membrane permeance, again by tuning to match steady-state experimental data. The permeance was used in the segmental model predictions. In Chapter 5, a series of experimental tracer studies were conducted to provide validation data for dynamic predictions made by using the segmental and CFD models. The results indicated that both models provided reasonable predictions of the residence time distributions for permeating tracers.

The primary goal of this study is to validate the segmental model through comparison with data that is representative of conditions encountered in an actual anesthesia circuit. A secondary objective is to investigate how the current membrane module performs under realistic patient scenarios, which will guide future scale-up or scale-down studies. The experimental data was generated by connecting the membrane unit into an anesthesia circuit comprising an anesthesia machine with a ventilator and a lung simulator (to represent the patient). Only O_2 and CO_2 were used in the experiments, since previous preliminary experiments have shown that the anesthetic vapours have minimal effects on the separation performance of the membrane.

6.2   System Overview

6.2.1 Inhalation Anesthesia

During general anesthesia, muscle-relaxing drugs are administered to suppress spontaneous respiration. To maintain pulmonary gas exchange in the absence of spontaneous respiration, mechanical ventilation is used to supply gas into the patient's lungs. Ventilation is also used to deliver anesthesia compounds during inhalation anesthesia. Current inhalation anesthesia machines are designed to mix breathing gases with anesthetic compounds and deliver them to the patient via mechanical ventilation. Different parameters are set on the mechanical ventilator based on the patient's metabolic needs. These machines are programmed to deliver distinct set tidal volumes and breaths per minute of the anesthetic gas mixture. The gas mixture typically contains O_2 and anesthetic compounds such as sevoflurane, desflurane, or isoflurane. These compounds are not metabolized, so they may be recirculated to the patient upon removal of excess CO_2.

The expired or end tidal CO_2 (etCO_2) is the concentration measured on exhalation, which is then recirculated to the anesthesia circuit. The fraction of inspired CO_2 (FiCO_2) is the concentration delivered on inhalation, after CO_2 has been removed by a CO_2 removal device. The expired CO_2 varies depending on the metabolic needs of the patient, but is typically around 5% by volume (or mole). The inspired CO_2 must be maintained below 0.5 vol%. For the membrane system, 0.5 vol% is therefore used as the target CO_2 concentration that must be achieved at the outlet of the membrane system. A drawing of a partial rebreathing anesthesia circuit is shown in Figure 6.1.
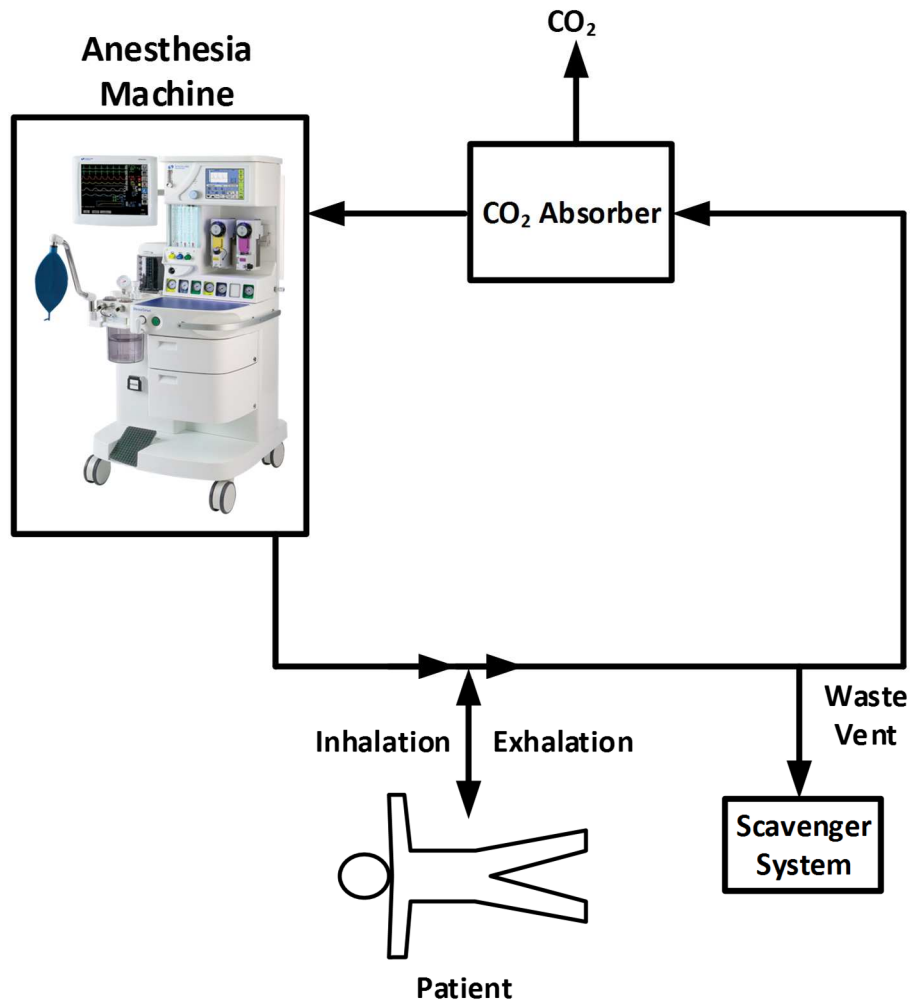
Figure 6.1. Flow diagram of an anesthesia breathing circuit.

Another important parameter in ventilation is the minute volume, or the total volume delivered to the patient per minute. The minute volume is the product of the breathing frequency and patient tidal volume:

$$MV = f \cdot TV \qquad (6.1)$$

where MV is the minute volume (mL min^{-1}), f is the breathing frequency (min^{-1}), and TV is the tidal volume (mL).

6.2.2 Membrane System

In this study, a hollow fiber membrane module was used to replace the CO_2 absorber typically used in anesthesia circuits (see Figure 6.3). The membrane bundle is composed

of a cross-wound hollow fiber mat wrapped around a hollow cylindrical tube. The fibers are potted at each end to separate the shell and tube-side flows. The assembled membrane bundle was supplied by 3M, Membranes Business Unit. The bundle was then placed into a custom housing (manufactured using SLS Rapid Prototyping, Stratasys Ltd., Eden Prairie, Minnesota, USA). To optimize the system performance, the membrane assembly was configured into a two-pass system using an O-ring on the bottom of the bundle to force the tube-side flow to take two passes through the module.

During operation, the feed gas (exhaled stream from the patient) enters the membrane bundle through the core on the shell-side and flows radially outward across the membrane bundle. A sweep gas is administered to the outer pass of tubes and then returns through the inner pass.

6.3 Experimental

6.3.1 System Description

Experiments were performed using a simulated anesthesia circuit, as shown in Figure 6.2. During the experiments, a Tangens 2C anesthesia machine (EKU Elektronik, Leiningen, Germany [47]) was operated in controlled mode. An O_2 fresh gas flow rate was supplied to the circuit at a rate of 0.2 L min^{-1}. The ratio of inspiration to expiration was set to 1:1. The positive end-expiratory pressure (PEEP) was set to 5 mbar and the maximum pressure was set to 50 mbar. The tidal volume and minute volume were set for each patient case. The delivered tidal volume accuracy was $\pm$ 10% of the set value. The accuracy for other measured values were $\pm$ 8% for tidal volume, $\pm$ 8% for minute volume, and $\pm$ 1 min^{-1} for the breathing frequency. For the time-dependent parameters, the resolution for flow was $\pm$ 0.1 L min^{-1} and the relative accuracy was $\pm$ 10%, and for pressure the resolution was 1 mbar and the accuracy is $\pm$ 1 mbar.

In these experiments, the CO_2 absorber was replaced by the membrane module and the patient was replaced by a lung simulator. The anesthesia machine provided mechanical ventilation to a lung simulator (ASL 5000, IngMar Medical, Pittsburgh, PA, USA), which was operated in passive mode. Lung characteristics, such as compliance and resistance,

were defined in the software operating the lung simulator. These lung properties influence the pressure, volume, and flow curves associated with mechanical ventilation. Compliance relates the change in pressure to the change in volume in the patient [48]. Practically, the compliance is governed by the elasticity of the lungs and chest wall. The lung mechanical properties were kept the same for this study. The lung compliance was set to 10 mL cmH$_2$O^{-1} and the resistance was set to 5 cmH$_2$O L^{-1} s^{-1}. Different tidal volumes and breathing frequencies were set on the anesthesia machine. These values were selected based on typical patient parameters that would be observed in clinical practice.

The lung simulator was connected to a Y-fitting, which was attached to an expiratory and an inspiratory tube. The anesthesia machine was connected to the inspiratory tube. A constant flow rate of CO_2 was provided to the expiratory tube to mimic the expected metabolic generation from the patient. The expiratory tube was attached to the shell-side of the membrane module, permitting the CO_2-enriched expiratory gas stream to flow into the module. The outlet of the membrane was attached to the anesthesia machine. Pure O$_2$ was used as a sweep gas on the tube-side of the membrane. The sweep flow rate was controlled using a Scott Specialty Gases glass tube flow meter (± 5% of full scale, 15.61 L min^{-1}) and measured using an Aalborg XFM digital mass flow meter (± 5% of full scale, 20 L min^{-1}). For the higher sweep flow rate cases (30 L min^{-1}), two flow meters were used in parallel and the two flows were combined with a three-way fitting. The outlet sweep gas concentration was monitored using a quadrupole mass spectrometer (Omnistar Model PTM81217131, Pfeiffer Vacuum, Aßlar, Germany) with a minimum detection limit of 1 ppm. Pfeiffer Vacuum's Quadera software (v4.50.004) was used to control the mass spectrometer. The time-dependent concentration data for each trial were exported to Microsoft Excel for post-processing.

The inspired and expired CO_2 concentrations were continuously measured using a Datex Ohmeda patient monitor (accuracy ± 0.3 vol.% [49]). The CO_2 flow rate was adjusted to obtain the target expired CO_2 concentration on the patient monitor, which was defined for the different patient cases.

The effective end tidal CO_2 concentration was measured on the expiratory limb, after the CO_2 flow rate is added to the mixture. The gas stream exiting the lung simulator (having the end tidal CO_2 concentration) was directed to the shell-side of the membrane module. The retentate leaving the membrane, which should have a breathable CO_2 concentration, was then recirculated back to the anesthesia machine and subsequently back to the lung simulator.

The concentration entering the membrane is assumed to be equal to the end tidal CO_2 concentration and the concentration leaving the membrane is effectively the inspired CO_2 concentration. As a result, the inspired CO_2 can be used as a metric to compare the membrane performance. A schematic of the experimental setup is shown in Figure 6.2.
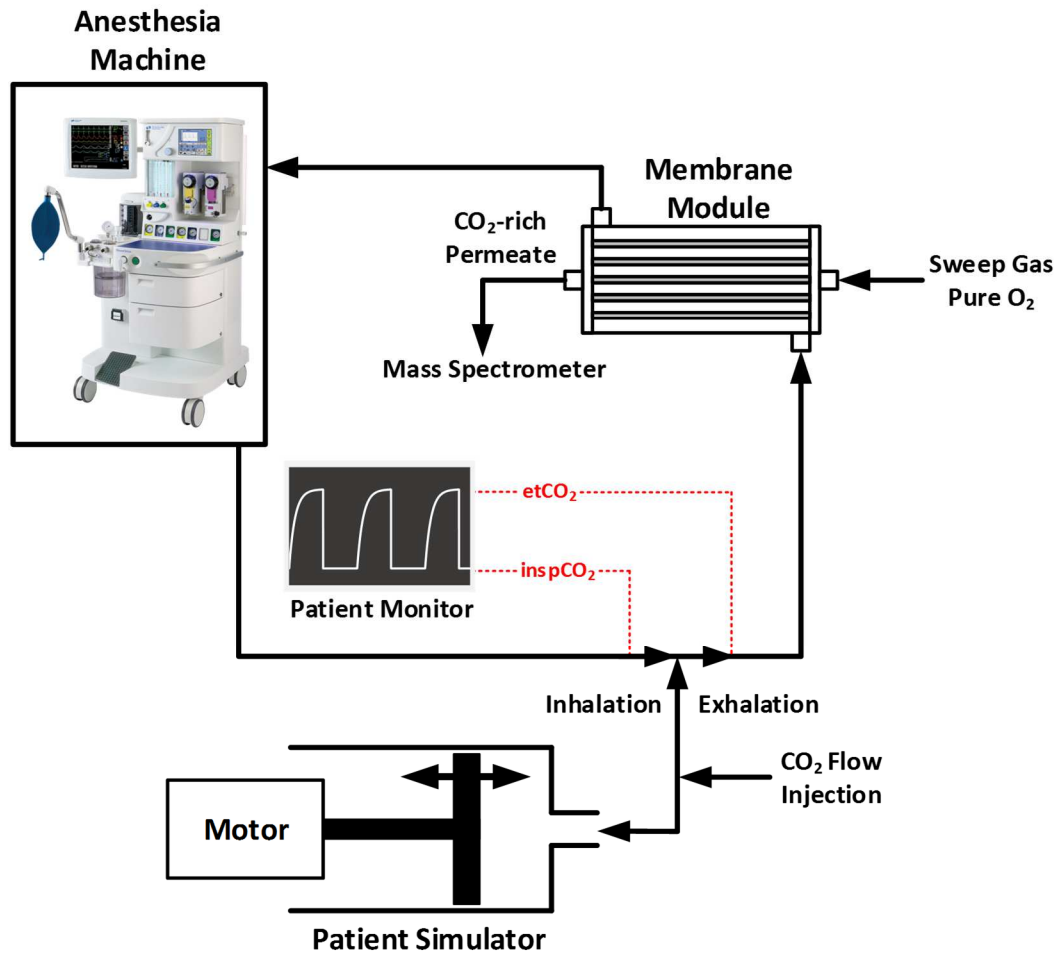
Figure 6.2. Flow diagram of experimental setup.

The data in these experiments were largely derived from the outputs displayed on the anesthesia machine and the patient monitor. The CO_2 waveform typically seen on the patient monitor is included in Figure 6.2. A labelled photo of an anesthesia machine monitor, with ventilator parameters indicated, is shown in Figure 6.3.
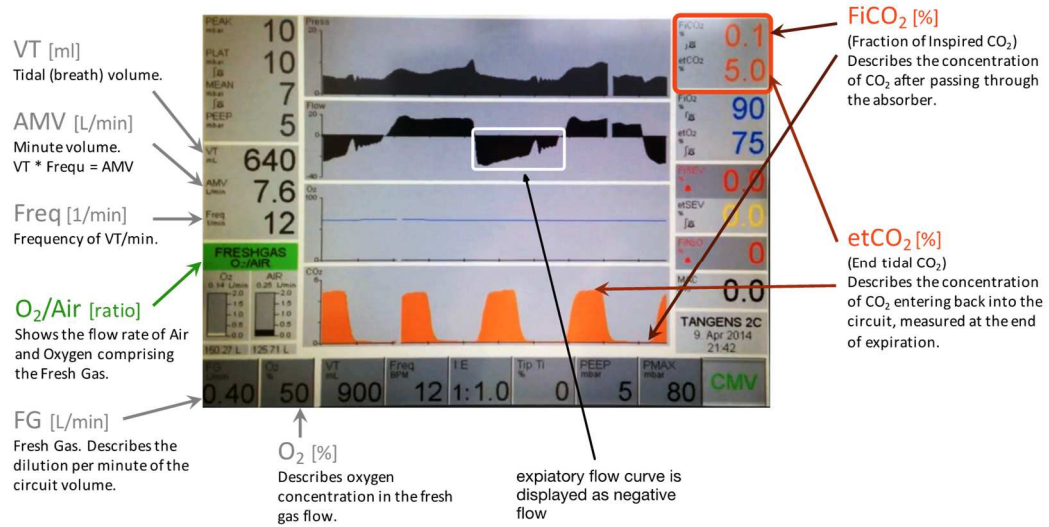
Figure 6.3. Labelled photo of an anesthesia machine monitor [50].

6.3.2 Patient Cases

The tidal volume, breathing frequency, expired CO_2 concentration, and sweep flow rate were defined for each simulated patient case. The tidal volume and frequency were defined on the anesthesia machine. The airway compliance and resistance were set on the lung simulator, which was operated in passive mode. Airway mechanical properties were kept the same for all the cases in this study. The expired CO_2 concentration was achieved by manipulating the CO_2 flow rate entering the expired tube. The list of patient cases used in this study is summarized in Table 6.1.

Table 6.1. Summary of patient cases

NSHA percentile	Minute volume (mL min^{-1})	Frequency (min^{-1})	Tidal volume (mL)	Expired CO_2 (vol. %)	Sweep flow rate (L min^{-1})
25th	4500	10	450	4.8	20
25th	4500	6	750	4.8	20
25th	4800	12	400	4.8	20
25th	4800	8	600	4.8	20
25th	4900	14	350	4.8	20
25th	5000	20	250	4.8	20
50th	5600	14	400	4.8	20
50th	5700	6	950	4.8	20
50th	5840	8	730	5.8	10, 20, 30
50th	6000	12	500	4.8	20
50th	6000	10	600	4.8	20
50th	6000	8	750	4.8	20
75th	7000	14	500	4.8	20
75th	7000	10	700	4.8	20
75th	7200	12	600	4.8	20
75th	7200	8	900	4.8	20
95th	9000	12	750	4.8	20
95th	9000	10	900	4.8	20
95th	9100	14	650	4.8	20
95th	9300	10	930	4.8	10, 20, 30
95th	9360	12	780	5.8	10, 20, 30

The 9300 and 9360 minute volume cases were selected because they represent the largest of the 95th percentile category of minute volume of patients based on the data collected from the Nova Scotia Health Authority from 2011-2013 (patient data collection method is described in ref. [50]). The 5840 minute volume case represents the median case. These select cases were run with three sweep flow rates, as indicated in the summary table (Table 6.1.).

6.4 Model Description

6.4.1 Membrane Model

The membrane system design model was described in detail in Chapter 3. The model was formulated by dividing the membrane module into discrete, perfectly-mixed segments and solving the unsteady material balance equations for all segments. This methodology assumes constant and equivalent properties for each cell. The mass transfer across the membrane and resulting outlet state are computed using the specified inlet conditions. The exiting conditions are then used as the inlet conditions for the successive segments. Each sub-section represents a control volume over a segment of membrane area of feed and sweep. The model equations were derived by performing a total and species mass balance over the permeate and retentate sides of the sub-section. The model equations are summarized in Table 6.2 with respect to component i.

Table 6.2. Summary of segment model equations

Transmembrane flow rate

$$N_i = K_i A_M (y_{i,R} P_R - y_{i,P} P_P)$$

Retentate and permeate flow rates

$$F_R = F_F - \sum N_i$$

$$F_P = F_S + \sum N_i$$

Retentate and permeate concentrations

$$\frac{dy_{i,R}}{dt} = \frac{y_{i,F} F_F - y_{i,R} F_R - N_i}{n_R}$$

$$\frac{\partial y_{i,P}}{\partial t} = \frac{y_{i,S} F_S - y_{i,P} F_P + N_i}{n_P}$$

In the segmental model, N_i is the molar flow rate of component i across the membrane of the segment (mol s^{-1}), K_i is the membrane permeance (mol m^{-2} s^{-1} bar^{-1}), A_M is the segment membrane area (m^2), $y_{i,R}$ and $y_{i,P}$ are the molar fractions of component i on the retentate and permeate side of the membrane, respectively, P_R and P_P are the bulk pressures (bar) of the retentate and permeate side, and F_F, F_S, F_R and F_P are the molar flow rates of the feed,

sweep, retentate and permeate (mol s^{-1}). A schematic representation of the segmental model approach is shown in Figure 6.4.
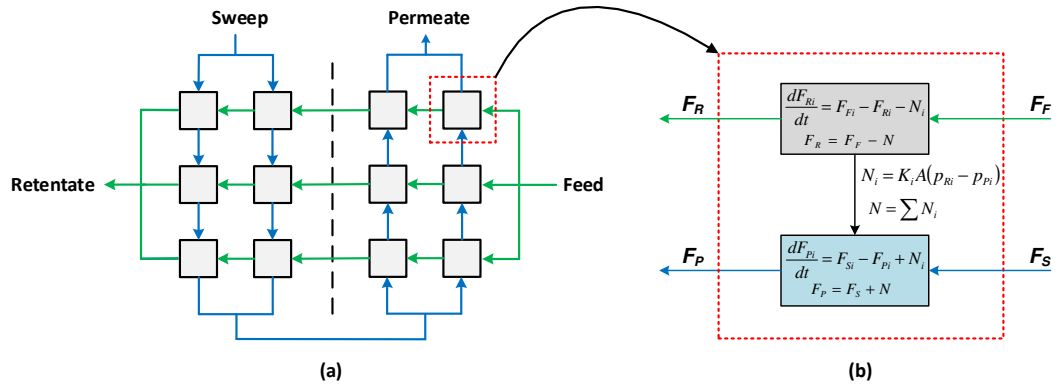
Figure 6.4. Schematic representation of (a) model structure for a double-pass membrane, and (b) control volume over each feed and sweep segment with coupling equations.

The number of discrete segments was determined by setting the membrane permeability and tuning the segments to match experimental steady-state separation performance data. The final discretization scheme for the membrane module used in this study was determined to require 10 segments representing the tube side and 6 segments representing the shell side.

The membrane discretization was represented using a SIMULINK block diagram [36]. The equations derived from the total and component material balances coupled by the local membrane permeation rate were solved for each discrete subsection using the Simulink integrator function and Simulink's continuous explicit variable step *ode45* solver.

A summary of the parameters used in the model is provided in Table 6.3.

Table 6.3. Parameters used in membrane model

Parameter	Value
Active membrane area (m^2)	2.10
Number of passes (-)	2
Packing density (-)	0.45
Fiber inner diameter (μm)	200
Fiber outer diameter (μm)	380
Number of fibers (-)	29500
Active membrane length (mm)	120
Core diameter (mm)	20
O-ring diameter (mm)	70
Bundle diameter (mm)	100
CO_2 permeance (mol m^{-2} h^{-1} bar^{-1})	45.0
O_2 permeance (mol m^{-2} h^{-1} bar^{-1})	18.0

6.4.2 System Model

The dynamic input conditions for the membrane model were generated using an existing ventilator model. The ventilator model was used to generate the time-dependent flow, volume, and pressure curves. These curves and peak values were compared to the corresponding outputs displayed on the anesthesia machine. The model values were adjusted to match the anesthesia machine displays. The expired flow rate generated by the ventilator model was then used as the input flow rate for the membrane model. An example of the ventilator output curves integrated with the membrane model is shown in Figure 6.5.
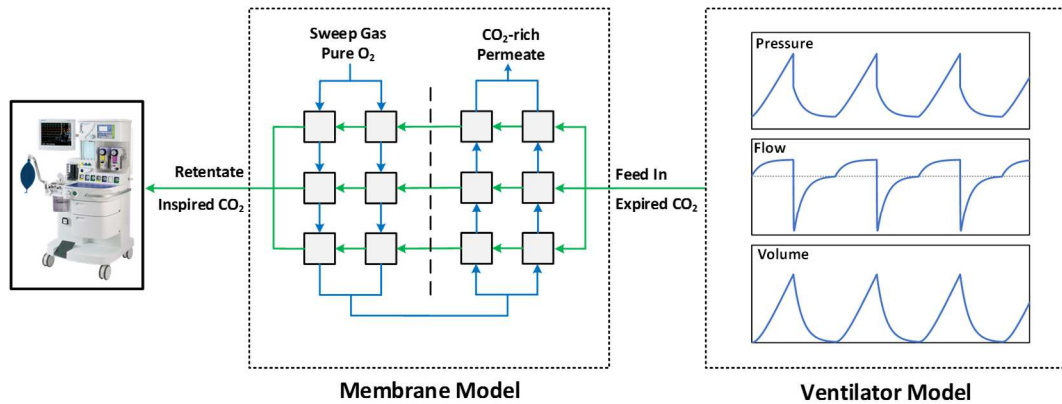
Figure 6.5. Example of generated ventilator model curves for pressure, flow, and volume integrated with the membrane model.

The average concentration exiting the membrane (referred to as the inspired CO_2) was calculated by integrating the product of the CO_2 mass fraction and the flow rate over a sufficiently long time period.

The concentration input used in the membrane model was the end tidal CO_2 concentration reported on the patient monitor. The average inspired concentration was read from the patient monitor once the system stabilized. However, due to the dynamic nature of the system, there was some fluctuation in the value. Therefore, a representative value was selected to compare to the model output.

The outlet concentration of the sweep stream was measured using the mass spectrometer. The output curve was exported for a long enough time to yield a stable average once the system had stabilized. The average concentration over a period was then compared to the average concentration output of the simulated system. Figure 6.6 shows an example of the data exported from the mass spectrometer for the permeate concentration. The average concentration was calculated by integrating the concentration over time using the trapezoid method in MATLAB.
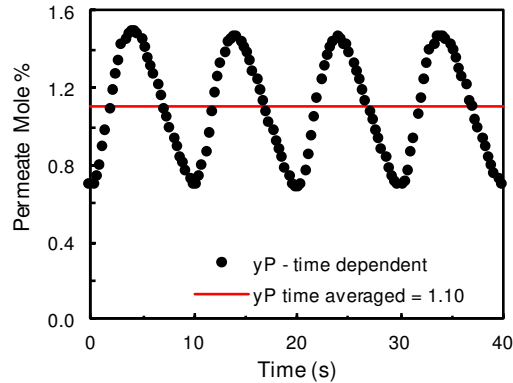
Figure 6.6. Example experimental sweep concentration exported from the mass spectrometer showing the calculated average.

6.5 Results and Discussion

6.5.1 Model Validation

The experimental conditions were reproduced in the simulation to compare the predictions to the experimental results. Since the inspired CO_2 concentration is a stringent performance target that the membrane must achieve to be used in anesthesia circuits, this value is critically important. The inspired CO_2 concentration and the sweep CO_2 concentration exiting the membrane were measured experimentally for all patient cases listed in Table 1. To compare the experimental outputs to the corresponding simulated results, the dynamic concentration averages were used. For the experimental inspired CO_2 concentration, the stabilized value was read on a clinical patient monitor, which reports a CO_2 accuracy reading of ±0.3% by volume. For the experimental sweep concentration, the value was monitored using the mass spectrometer and the dynamic concentration was averaged over a time period. For the simulated values, the flow-averaged concentrations were averaged over a time period.

Figure 6.7 shows a comparison between the predicted and simulated results for the inspired CO_2 concentration and permeate CO_2 concentration. The horizontal error bars on Figure 6.7a are ± 0.3 vol.% CO_2 concentration, corresponding to the accuracy of the patient monitor. The different colours represent the minute volume ranges corresponding to Table 6.1.

105
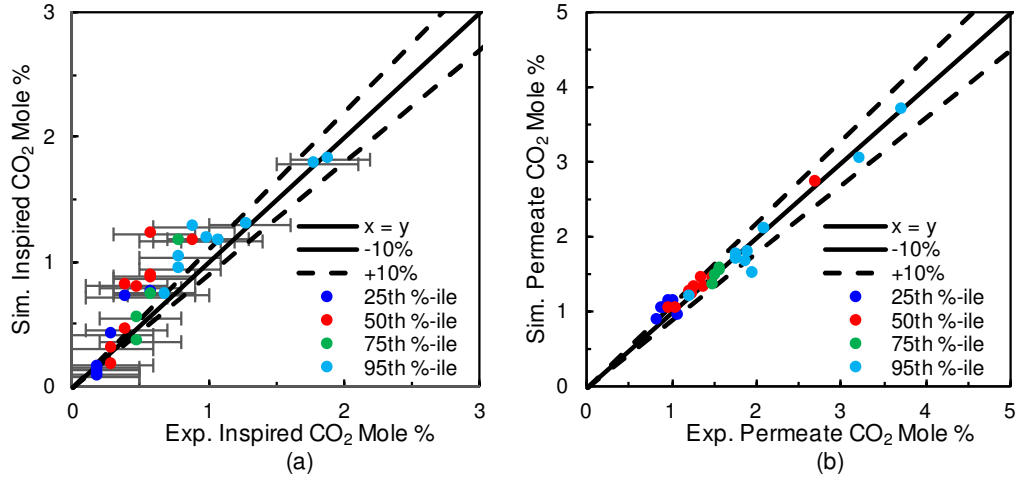
Figure 6.7. Parity plot of experimental data *vs.* simulated predictions for (a) inspired CO_2 concentration (measured on patient monitor with horizontal error bars $\pm$ 0.3 vol.% representing measurement accuracy), and (b) CO_2 permeate concentration (measured on mass spectrometer).

Overall, the simulated data matches the experimental data reasonably well within the accuracy range of the measurement equipment, and considering potential sources of errors and variabilities associated with the experimental configuration. One weakness of the configuration is the inherent variability of the experimental conditions, which were then used in the model. To simulate a patient generating CO_2, a constant flow rate of CO_2 was used until an appropriate end tidal CO_2 reading was obtained on the patient monitor. One challenge with this approach is that the waveform varies slightly for each period. Furthermore, the patient monitor rounds the concentration percentage to the nearest decimal place, so low inspired CO_2 concentrations are likely to have a higher relative error associated with the measurements.

6.5.2 Membrane System Performance

The minute volume is the product of the frequency and tidal volumes, and directly corresponds to the quantity of CO_2 produced by the patient. The patient data was selected to be representative of the range of minute volumes observed in the population. For each defined minute volume, the frequency and tidal volume can be varied. Thus, even though the minute volume is essentially constant, the dynamic behaviour varies which has performance implications.

The minute volume ranges are grouped into the 25th, 50th, 75th, and 95th percentile categories (refer to Table 6.1 for the specific experimental cases). Figure 6.8 shows the inspired CO_2 concentration for different respiratory frequencies for the minutes volume from the four percentile ranges. Figure 6.8a shows the experiment and Figure 6.8b shows the simulation. It is also worth noting that the data displayed in Figure 6.8 includes only the cases with a 20 L min^{-1} sweep flow rate and 4.8% theoretical expired CO_2 (as reported in Table 6.1).
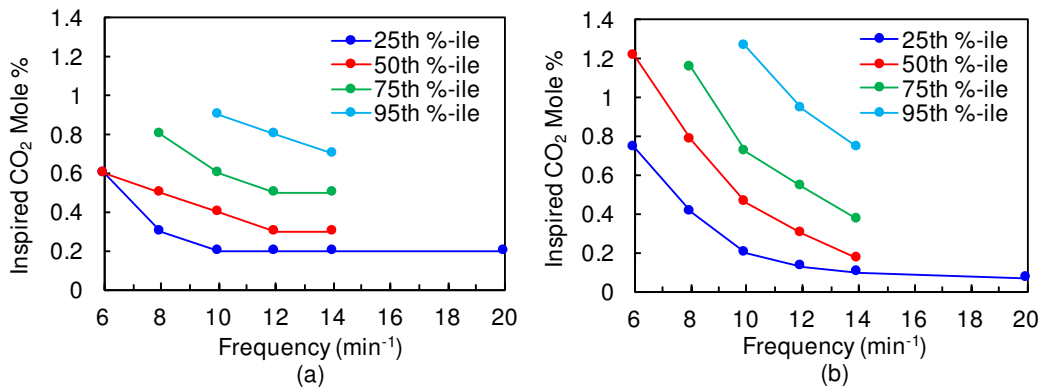
Figure 6.8. Experimental (a) and simulated (b) inspired CO_2 concentration over a range of respiratory frequencies for different patient tidal volumes with constant minute volumes. Each series refers to the percentile range of minute volumes. 25th percentile minute volume is 4500-5000 mL min^{-1} 50th percentile is 5600 to 6000 ml min^{-1}, 75th percentile is 7000 to 7200 mL min^{-1} and 95th percentile is 9000 to 9100 mL min^{-1}. Results shown on the graphs are cases with 20 L min^{-1} sweep flow rate and 4.8% expired CO_2.

Clearly, the experimental and simulated data points are not a perfect match. The simulated inspired CO_2 is noticeably higher than the experimental CO_2 in all cases for frequencies of 6 min^{-1} and 8 min^{-1}.

Increasing the breathing frequency while maintaining the minute volume causes a decrease in the inspired CO_2 concentration exiting the membrane. Since the experimental results are shown and the experimental conditions were used as an input in the model, there is some variability in the inputs that could influence the trends observed on the graphs. For instance, the CO_2 concentration entering the membrane (exp. CO_2) ranges from 4.8 to 5.1 %. Furthermore, although the minute volumes are in a similar range for each category, they are not identical. The 25th percentile theoretical minute volume ranges covers from 4500 to 5000 mL min^{-1}, and there is further uncertainty and variability in the volume delivered

107

by the anesthesia machine. The data points were connected for the sole purpose of providing visual guides and to assist the comparison of the graphs with the same inputs.

The overall trend in the data points is similar in both the experimental and modeled data. For instance, decreasing inspired CO_2 is observed with increasing frequency at a constant minute volume. The exception to this trend is in the 25th percentile group at higher frequencies. The inspired CO_2 reported from the patient monitor is the same for 12, 14, and 20 min^{-1} frequencies. This is perhaps an artefact of the patient monitor rounding to a single decimal position. The corresponding simulated cases show a small inspired CO_2 decrease with increasing frequency from 12 to 20 min^{-1}. However, if the concentration is reported with the same precision as the patient monitor, the inspired CO_2 concentrations of 0.13, 0.09, and 0.07 are all within the range of 0.1. The significant uncertainty associated with both the input and output measurements is certainly a drawback of this experimental approach. Another possible source of experimental error in the CO_2 measurement could come from residual gases trapped in the system and axial back mixing in the sampling tube.

Figure 6.9 shows the simulated and experimental inspired CO_2 and permeate concentration for three patient cases at varying sweep flow rates.
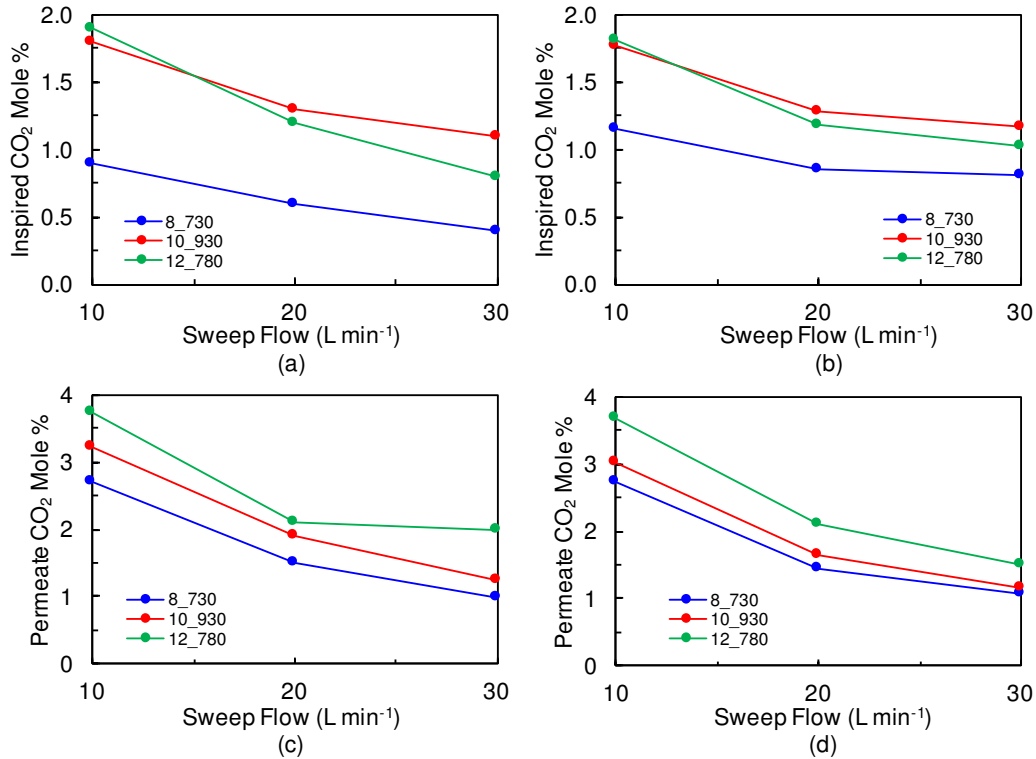
Figure 6.9. Experimental (a and c) and simulated (b and d) effect of sweep flow rate on inspired CO_2 (a and b) and permeate CO_2 (c and d) for three key representative patients: median patient (MV = 5840 mL min^{-1}, f = 8, TV = 730 mL, etCO$_2$ = 5.8%) and two 95th percentile patients (MV = 9300 mL min^{-1}, f = 10, TV = 930 mL, etCO$_2$ = 4.8%, and MV = 9360 mL min^{-1}, f = 12, TV = 780 mL, etCO$_2$ = 5.8%)

Increasing the sweep flow rate decreases the inspired CO_2 concentration for all cases. However, for different cases the effect for varying sweep flow rates is different. The model is able to predict the trends with increasing sweep flow rate reasonably well. Since the target CO_2 concentration to be rebreathed is 0.5%, the model is useful for performing design studies and studying the effect of membrane size and sweep flow rate for different patient cases. The results presented in Figure 6.9 clearly indicate that the membrane module would likely have to be scaled up for the patient cases presented in this figure.

6.5.3 General Discussion

Some of the challenges experienced in these experiments resulted from using medical equipment and monitoring technologies. While medical instruments are appropriate for monitoring in a clinical setting, they are not always ideal for generating model validation data. In addition to the CO_2 measurements, there is also considerable variability and

uncertainty associated with the ventilator parameters provided by the anesthesia machine. The tidal volume and frequency are set, and the pressure, flow and volume wave forms are generated and directed to the lung simulator. During the experiments, the measured tidal volume and frequency reported on the anesthesia monitor experienced some deviation from the set parameters. Modeling is already challenging when an accurate input is available, but doubting the reliability of the input makes model troubleshooting even more challenging.

The membrane model was found to be quite sensitive to the ventilator model. The model waveforms were compared to those on anesthesia machine, and tuned if necessary. However, given the low resolution and accuracy range, the anesthesia monitor is not the best candidate for image analysis. Figure 6.3 shows the ventilation waveforms of interest. Clearly, there is some noise in the data and variability between the periods, so a ventilator model was used in this study. The addition of the ventilator model adds consistency to the model prediction, but it also complicates model validation because it introduces more model uncertainties.

6.6 Conclusions

The main purpose of this study was to validate a mathematical model for a membrane system that is intended to be used for removing CO_2 from anesthesia circuits. Experiments were performed with a simulated anesthesia circuit, which included the membrane module, an anesthesia machine, and a lung simulator. The system was used to collect experimental data for realistic patient scenarios. The membrane model was coupled with a ventilator model to provide predictions of the CO_2 concentrations within the circuit.

The results indicated that the design model was generally able to predict trends in the experimental data. However, some individual data points were not accurately predicted. The study highlights difficulties that can be encountered in validating such dynamic models, due to the uncertainty and variability associated with the experimental approach and assumptions in the modeling methodology. However, it is important to reflect on the broad goals of this exercise in the context of developing a novel device for anesthetic gas separation. It is very important that the membrane itself is able to perform as expected

110

before it is commercialized and used in patients. It is also important to understand the performance of the membrane in extreme cases with different ventilation parameters and the effect of dynamics on performance. While it is challenging to precisely reproduce the experiments by simulations, overall the model is able to predict the performance reasonably well given the large variability in the experiments. Further, knowing the expected accuracy of the model predictions, it is now possible to provide scale-up predictions for membrane modules with an appropriate margin of error.

6.7 Nomenclature

Abbreviations

f	respiration frequency (min^{-1})
$etCO_2$	end tidal CO_2 concentration, equivalent to $expCO_2$
$expCO_2$	expired CO_2 concentration, equivalent to etCO2
$inspCO_2$	inspired CO_2 concentration
MV	minutes volume ($mL\ min^{-1}$)
TV	tidal volume (mL)

Symbols

A_M	membrane area (m^2)
F	molar flow rate ($mol\ s^{-1}$)
n	number of moles
K	membrane permeance ($mol\ m^{-2}\ h^{-1}\ bar^{-1}$)
N	molar flow rate across the membrane ($mol\ s^{-1}$)
P	pressure (bar)
t	time (s)
y	molar fraction

Subscripts

i	species i
F	feed
P	permeate
R	retentate
S	sweep

Chapter 7:   Conclusions

Inhalation anesthesia is normally delivered in partial rebreathing circuits, necessitating the removal of CO_2. This thesis focused on the development and validation of models for performance prediction of a new membrane system for CO_2 removal from anesthesia circuits. The main objective of this thesis project was to develop and experimentally validate a modeling approach to predict and optimize the membrane system performance. A secondary objective was to investigate how the current membrane module performs under realistic patient scenarios, which would guide future scale-up or scale-down studies. To achieve the objective, several studies were conducted.

In Chapter 3, a segmental model was derived and validated for steady-state predictions. The number of segments in the model was tuned to match the experimental data. The results indicated that the model could provide adequate steady-state performance predictions over a wide range of operating conditions.

In Chapter 4, a CFD model implemented in COMSOL Multiphysics was developed to analyze the separation performance and flow behavior in the system. The membrane permeance was tuned to match steady-state experimental data, and the permeance was subsequently used in the segmental model predictions. The CFD model was also used to simulate ideal residence time distribution studies to quantitatively assess mixing patterns in the module and the effect of membrane permeation on the RTD parameters. These tracer simulations revealed that such studies would be sensitive to permeation of the tracer across the membrane.

In Chapter 5, a series of experimental tracer studies were conducted to provide validation data for dynamic predictions by the segmental and CFD models. The results indicated that both models provided reasonable predictions of the residence time distributions for permeating tracers.

In Chapter 6, membrane performance for removing CO_2 from anesthesia circuits for different patient scenarios was investigated. Validation data was collected using an experimental anesthesia circuit configured with an anesthesia machine, lung

112

simulator, and the membrane. The results indicated that the model was generally able to predict experimental trends, but some individual data points were not accurately predicted. While it is challenging to precisely reproduce dynamic experiments by simulations, overall the model predicts the performance reasonably well given the large variability in the experiments.

The models developed in this thesis were shown to be useful tools for designing and optimizing the performance of the studied membrane system. The CFD model was useful for understanding mixing and mass transfer processes in the membrane module, and for studying aspects of the process that are difficult to investigate experimentally. The segmental design model was experimentally validated for the system and has been used to study the performance for different patient scenarios. The design model fulfills the criteria of predicting the performance of the dynamic membrane system using minimal computational resources with acceptable accuracy. Although the modeling techniques developed in this thesis were applied to a very specific membrane system, it is hoped that these approaches can also be extended to other applications.

References

[1]   P. Barash, *Clinical Anesthesia*, 8th Editio. Philadelphia, PA: Lippincott Williams & Wilkins, 2017.

[2]   G. Torri, "Inhalation anesthetics: A review," *Minerva Anestesiol*, vol. 76, no. 3, pp. 215–228, 2010.

[3]   Y. Ishizawa, "General anesthetic gases and the global environment," *Anesth Analg*, vol. 112, pp. 213–217, 2011.

[4]   L. Herbert and P. Magee, "Circle systems and low-flow anaesthesia," *BJA Educ*, vol. 0, no. 0, pp. 1–5, 2017.

[5]   C. Keijzer, R. S. G. M. Perez, and J. J. De Lange, "Compound A and carbon monoxide production from sevoflurane and seven different types of carbon dioxide absorbent in a patient model," *Acta Anaesthesiol Scand*, vol. 51, no. 1, pp. 31–37, 2007.

[6]   M. P. Bouche *et al.*, "Quantitative determination of vapor-phase compound A in sevoflurane anesthesia using gas chromatography-mass spectrometry," *Clin Chem*, vol. 47, no. 2, pp. 281–291, 2001.

[7]   M. Yamakage, K. Takahashi, M. Takahashi, J. Satoh, and A. Namiki, "Performance of four carbon dioxide absorbents in experimental and clinical settings," *Anaesthesia*, vol. 64, pp. 287–292, 2009.

[8]   E. M. Sakai, L. A. Connolly, and J. A. Klauck, "Inhalation anesthesiology and volatile liquid anesthetics: focus on isoflurane, desflurane, and sevoflurane.," *Pharmacotherapy*, vol. 25, pp. 1773–1788, 2005.

[9]   C. R. Stabernack *et al.*, "Sevoflurane degradation by carbon dioxide absorbents may produce more than one nephrotoxic compound in rats," *Can J Anesth*, vol. 50, no. 3, pp. 249–252, 2003.

[10]   G. W. Konat, W. A. Kofke, and S. Miric, "Toxicity of compound A to C6 rat glioma cells," *Metab Brain Dis*, vol. 18, no. 1, pp. 11–15, 2003.

[11]   S. Lagorsse, F. Magalhaes, and A. Mendes, "Xenon recycling in an anaesthetic closed-system using carbon molecular sieve membranes," *J Membr Sci*, vol. 301, pp. 29–38, 2007.

[12]   J. P. H. Fee, J. M. Murray, and S. R. Luney, "Molecular sieves: An alternative method of carbon dioxide removal which does not generate compound A during simulated low-flow sevoflurane anaesthesia," *Anaesthesia*, vol. 50, pp. 841–845, 1995.

[13]   G. H. Thompson, J. M. Murray, and J. P. H. Fee, "Absorption of carbon dioxide

and anaesthetic gases by zeolite 5A," in *Royal Academy of Medicine in Ireland Section of Biomedical Sciences*, 1996, vol. 165, pp. 306–307.

[14] M. Riecke, "Process and device for separating carbon dioxide from a breathing gas mixture by means of a fixed carrier membrane," US Patent No. 8146593 B2, 2012.

[15] S. Laurila, "Arrangement in connection with an anaesthesia/ventilation system for a patient and a gas separation unit for an anaesthesia/ventilation system," US Patent No. 7832398 B2, 2010.

[16] G. Obuskovic and K. K. Sirkar, "Liquid membrane-based CO2 reduction in a breathing apparatus," *J Membr Sci*, vol. 389, pp. 424–434, 2012.

[17] A. Portugal, F. Magalhaes, and A. Mendes, "Carbon dioxide removal from anaesthetic gas circuits using hollow fiber membrane contactors with amino acid salt solutions," *J Membr Sci*, vol. 339, no. 1–2, pp. 275–286, 2009.

[18] F. Wilfart *et al.*, "Design of a membrane system for carbon dioxide removal from gas mixtures under normobaric conditions in anaesthesia circuits (pending submission)," *J Membr Sci*, 2017.

[19] Z. Cui and D. DeMontigny, "Part 7: A review of CO2 capture using hollow fiber membrane contactors," *Carbon Manag*, vol. 4, no. 1, pp. 69–89, 2014.

[20] J.-L. Li and B.-H. Chen, "Review of CO2 absorption using chemical solvents in hollow fiber membrane contactors," *Sep Purif Technol*, vol. 41, no. 2, pp. 109–122, Feb. 2005.

[21] M. S. Shafeeyan, W. M. A. Wan Daud, and A. Shamiri, "A review of mathematical modeling of fixed-bed columns for carbon dioxide adsorption," *Chem Eng Res Des*, vol. 92, no. 5, pp. 961–988, May 2014.

[22] A. Gabelman and S.-T. Hwang, "Hollow fiber membrane contactors," *J Membr Sci*, vol. 159, no. 1–2, pp. 61–106, 1999.

[23] J. G. Wijmans and R. W. Baker, "The solution-diffusion model: a review," *J Membr Sci*, vol. 107, pp. 1–21, 1995.

[24] K. L. Wang and E. L. Cussler, "Baffled membrane modules made with hollow fiber fabric," *J Membr Sci*, vol. 85, pp. 265–278, 1993.

[25] S. R. Wickramasinghe, M. Semmens, and E. L. Cussler, "Mass transfer in various hollow fiber geometries," *J Membr Sci*, vol. 69, no. 3, pp. 235–250, 1992.

[26] F. Wilfart, M. Soehl, N. Kilcup, I. Voigt, and J. Haelssig, "Characterization of dense PMP membranes for the separation of carbon dioxide from anaesthetic

vapours in low pressure applications (pending submission)," *J Membr Sci*, 2017.

[27]   V. Dindore, A. H. G. Cents, D. Brilman, and G. F. Versteeg, "Shell-side dispersion coefficients in a rectangular cross-flow hollow fibre membrane module," *Chem Eng Res Des*, vol. 83, no. 3, pp. 317–325, 2005.

[28]   S. H. Fogler, *Elements of Chemical Reaction Engineering*. Pearson Education, 2005.

[29]   F. Liotta, P. Chatellier, G. Esposito, M. Fabbricino, E. D. Van Hullebusch, and P. N. L. Lens, "Hydrodynamic mathematical modelling of aerobic plug flow and nonideal flow reactors: a critical and historical review," *Crit Rev Environ Sci Technol*, vol. 44, no. 23, pp. 2642–2673, 2014.

[30]   C. Y. Wen and L. T. Fan, *Models for Flow Systems and Chemical Reactors*. New York, NY, NY: Marcel Dekkar, Inc., 1975.

[31]   J. Marriott and E. Sørensen, "A general approach to modelling membrane modules," *Chem Eng Sci*, vol. 58, no. 22, pp. 4975–4990, Nov. 2003.

[32]   T. Katoh, M. Tokumura, H. Yoshikawa, and Y. Kawase, "Dynamic simulation of multicomponent gas separation by hollow-fiber membrane module: Nonideal mixing flows in permeate and residue sides using the tanks-in-series model," *Sep Purif Technol*, vol. 76, no. 3, pp. 362–372, Jan. 2011.

[33]   D. Zaidiza, J. Billaud, B. Belaissaoui, S. Rode, D. Roizard, and E. Favre, "Modeling of CO2 post-combustion capture using membrane contactors, comparison between one- and two-dimensional approaches," *J Membr Sci*, vol. 455, pp. 64–74, 2014.

[34]   M. Binns *et al.*, "Strategies for the simulation of multi-component hollow fibre multi-stage membrane gas separation systems," *J Membr Sci*, vol. 497, pp. 458–471, 2016.

[35]   F. Ahmad, K. K. Lau, S. S. M. Lock, S. Rafiq, A. U. Khan, and M. Lee, "Hollow fiber membrane model for gas separation: Process simulation, experimental validation and module characteristics study," *J Ind Eng Chem*, vol. 21, pp. 1246–1257, Jan. 2015.

[36]   "MATLAB version 2017a." The MathWorks, Inc., Natick, Massachusetts, United States, 2017.

[37]   *The Vacuum Technology Book*. Pfeiffer Vacuum GmbH, 2009.

[38]   S. Foster, "Multiple Concentration Determination." Pfeiffer Vacuum, 2012.

[39]   R. S. Brodkey and H. C. Hershey, *Transport Phenomena: A Unified Approach*,

Internatio. New York, NY: McGraw-Hill, 1998.

[40] "COMSOL Multiphysics® version 5.2." Stockholm, Sweden, 2017.

[41] J. Bear, *Dynamics of fluids in porous media*. New York, NY: American Elsevier Pub. Co., 1972.

[42] H. E. Pacella, H. J. Eash, B. Frankowski, and W. J. Federspiel, "Darcy permeability of hollow fiber bundles used in blood oxygenation devices," *J Membr Sci*, vol. 382, no. 1–2, pp. 238–242, 2011.

[43] M. Labęcki, J. M. Piret, and B. D. Bowen, "Two-dimensional analysis of fluid flow in hollow-fibre modules," *Chem Eng Sci*, vol. 50, no. 21, pp. 3369–3384, 1995.

[44] I. Borsi and O. Lorain, "A space-averaged model for hollow fibre membranes filters," *Comput Chem Eng*, vol. 39, pp. 65–74, 2012.

[45] O. Levenspiel, *Chemical Reaction Engineering*, Third. New York, NY: John Wiley & Sons, 1999.

[46] Z. Ren, Y. Yang, W. Zhang, J. Liu, and H. Wang, "Modeling study on the mass transfer of hollow fiber renewal liquid membrane: Effect of the hollow fiber module scale," *J Membr Sci*, vol. 439, pp. 28–35, 2013.

[47] "Tangens 2C Anaesthesia Unit Technical Specifications." EKU Elektronik GMBH, Leiningen, Germany.

[48] A. Hasan, *Understanding Mechanical Ventilation: A Practical Handbook*, Second. Springer London, 2010.

[49] "Datex Ohmeda S/5 Light Monitor User's Reference Manual." [Online]. Available: https://photos.medwrench.com/equipmentManuals/4468-2373.pdf.

[50] F. Wilfart, "Development and Assessment of a New Solution for Carbon Dioxide Removal from Anaesthesia Rebreathing Circuits," Phd Thesis, Dalhousie, 2016.